Photoexcitation, Photoionization, and X-Ray Scattering of Free Nanoparticles Prepared in a Beam

Inaugural-Dissertation

to obtain the academic degree

Doctor rerum naturalium (Dr. rer. nat.)

submitted to the Department of Biology, Chemistry and Pharmacy

of Freie Universität Berlin

by

Egill Antonsson

from Reykjavík, Iceland

2011

This thesis is based on work done in the time period March 2008 - August 2011 at the Institute for Chemistry and Biochemistry of the Freie Universität Berlin under the supervision of Prof. Dr. E. Rühl.

1^{st} Reviewer: Prof. Dr. E. Rühl

2^{nd} Reviewer: Prof. Dr. H. Baumgärtel

Date of Defence: 21.11.2011

Contents

Chapter 1

Introduction

Nanoparticles have attracted much attention in recent years due to their often unique chemical and physical properties. They are of interest to fundamental and applied research and they find an increasing number of application in technology and industry, such as in catalysis [1] and as additives to cosmetics, drugs delivery, printer toners, varnishes, cement, and food [2–4]. Dust particles in interstellar space and in the atmospheric environment often have a nanoscale size [5,6]. For instance, formation of H_2, the most abundant molecular species in interstellar space, is believed to take place on the surface of interstellar dust [7]. Furthermore, nanoscopic particles play an important role in the atmosphere, such as in cloud nucleation [8–10], where the size of the particles is an important parameter [11]. Due to the increased release of man made nanoparticles into the environment, interactions between nanoparticles and living organisms have been a topic of recent studies with respect to possible adverse health effects [12–19].

The properties of nanoparticles are the subject of this thesis, where SiO_2 is used as a model system for studies on single nanoparticles which are prepared in a continuous particle beam in high vacuum. This approach allows studying

the intrinsic properties of the nanoparticles which are free from interactions with a surrounding medium or a substrate, which is the case when studying deposited particles or dispersions. With the nanoparticle beam approach, changes to the sample over time due to radiation damage or charging by ionizing radiation can be neglected since fresh sample is continuously fed to the interaction area [20, 21].

This thesis deals with three novel aspects of the interaction of free nanoparticles with electromagnetic radiation:

In the first part, photoemission from free SiO_2 is studied after excitation by soft X-rays. Earlier work on photoemission from free SiO_2 nanoparticles focused on limited parts of the electron emission spectrum [22, 23]. In this thesis, a considerably wider electron emission spectrum for emission of one or two electrons after absorption of one photon is studied.

In the second part, the geometric structure (size distribution, shape) and optical properties of free SiO_2 nanoparticles is studied by small angle soft X-ray scattering. This work builds on earlier work, where elastic scattering of visible light has been successfully used to the study free micron sized particles [24–27]. For nanoparticles, previous work has focused on wide angle scattering [28, 29]. It is highlighted in the present work, that the small angle scattering is a promising way to study nanoparticles, since characteristic patterns in the angle resolved X-ray scattering patterns can be resolved, even if finite particle size distributions are studied, providing distinct information on the size distributions and optical constants of free nanoparticles. It is examined in this work, if these optical constants differ from those of the macroscopic condensed phase.

In the third part, electron emission from free SiO_2 nanoparticles after excitation by few-cycle laser pulses of well-defined, variable waveform is studied (pulse length: $\approx$ 5 fs, central wavelength: 720 nm). This pulse length corre-

sponds to about two oscillations of the electric field. For pulses of this length, the amplitude of the pulse envelope changes almost as fast as the electric field oscillates, which allows systematic control of the electron emission from the nanoparticles [30, 31].

Chapter 2

Theoretical Background

Bulk material has properties which are different from isolated atoms of its constituent elements. Between the limiting cases of a bulk materials, which contain an infinite or semi-infinite number of constituents, and isolated atoms or molecules lies particulate matter with finite dimensions, such as clusters and nanoparticles [32]. The distinction between these states of matter is not always clear, since a large clusters can often be considered as a a small nanoparticle and vice versa. A definition that has been offered earlier is that clusters are objects where the exact number of atoms is of importance, as seen for instance in magic numbers of atoms for clusters of rare gas atoms [33], molecules [34] or metals [35] where the stability of the clusters depends critically on the exact number of atoms. According to this definition, a nanoparticle is an object where the size of the entire object, rather than the exact number of atoms, is defining its properties [36].

Fig. 2.1 schematically shows the dependence of some property of interest on the size of an object going from a single atom on the left hand side to infinite bulk matter on the right hand side. In between these extremes, there is first a region where the property increases and decreases in discrete steps if just a

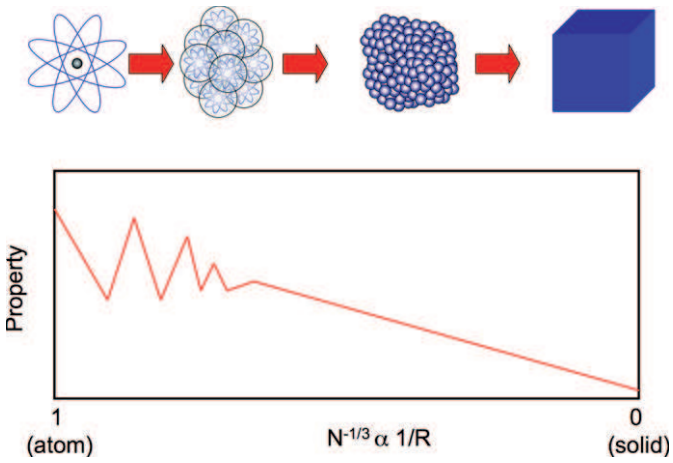

Figure 2.1: Some property of interest as a function of object size when going from a single atom to a bulk sample of the material. The current thesis is concerned with the continuous region where the size of the entire object is more important than the exact number of atoms. The Figure is taken from [45].

single atom is added or removed. This is followed by a region of continuous changes where the exact number of atoms is less important than the size of the entire object. This region of continuous changes is the focus of this thesis. The exact property can be any of numerous ones that depend on the size of the object [37, 38], such as the melting point [39], the secondary electron yield [40], electron binding energies [41, 42], optical constants [43], or chemical reactivity [44]. A characteristic property of clusters and nanoparticles is their high surface-to-bulk ratio. The higher the surface-to-bulk ratio is, the greater is the influence of the surface on the overall electronic and optical properties of the variable size object.

A nanoscopic object is usually defined as an object that is smaller than a particular length in at least one dimension. This length is often taken to be 100 nm [46, 47]. However, a definition of 100 nm is arbitrary since it has no deeper physical meaning. In this thesis, nanoparticles will therefore be defined as particles smaller than *a few hundred nanometers*.

2.1 SiO_2 Nanoparticles

Nanoscopic SiO_2 exists in a variety of natural and manmade forms [2]. Silica is a common trivial name for SiO_2. It can differ in size, shape, crystallinity, and porosity. Crystalline SiO_2 exists in numerous polymorphs [48]. Most involve tetrahedral SiO_4 units connected by shared vertices. Si-O-Si angles and Si-O bond lengths vary between the polymorphs. As an example, the most common naturally occurring form of crystalline SiO_2, α-quartz, has an Si-O-Si bond angle of 144° [49] and an Si-O bond length of 0.161 nm [50]. Porous SiO_2 nanoparticles can be classified according to their porosity as microporous (pore size under 2 nm), mesoporous (pore size 2-50 nm) and macroporous (pore size over 50 nm) species [51].

Various methods exist in the literature to synthesize nanoscopic SiO_2 for industrial applications and research. These can be roughly categorized into *top-down* and *bottom-up* methods depending on whether the nanoscopic particles are made out of larger objects (such as for instance through milling and grinding processes) or from smaller objects, such as by chemical syntheses. SiO_2 nanoparticles of with well-defined sizes and shape are often prepared by the Stöber synthesis [52]. It is an example of a *bottom up* method. In the Stöber synthesis, amorphous SiO_2 nanoparticles are made *via* condensation and nucleation of tetraethoxy silane in the presence of ammonia. Different nanoparticle sizes may be recieved by varying the reaction conditions (such as the concentration of ammonia, temperature, and choice of solvent) [53]. In order to study size dependent properties of nanoparticles, it is of importance to have samples with a narrow size distribution. The width of the size distribution is given by the polydispersity which is the relative standard deviation of the diameters in an ensemble of particles. Nanoparticles of low polydispersity are obtained from the seeded growth method [54–57]. In it, small nanoparti-

cles (a few nm diameter) of low polydispersity are made by the Stöber method and subsequently, layers of SiO_2 are grown onto the nanoparticles. The number of growth steps is chosen depending on the desired final nanoparticle size. Fig. 2.2 shows electron micrographs of SiO_2 nanoparticles of different sizes. The three samples are examples of SiO_2 nanoparticles that are obtained from the seeded growth method, using different numbers of steps, which leads in all three cases to almost perfectly spherical nanoparticles with a narrow size distribution and a diameter of (a) 63 nm ± 6%, 90 nm ± 5% (b), and 142 nm ± 4% (c), respectively.

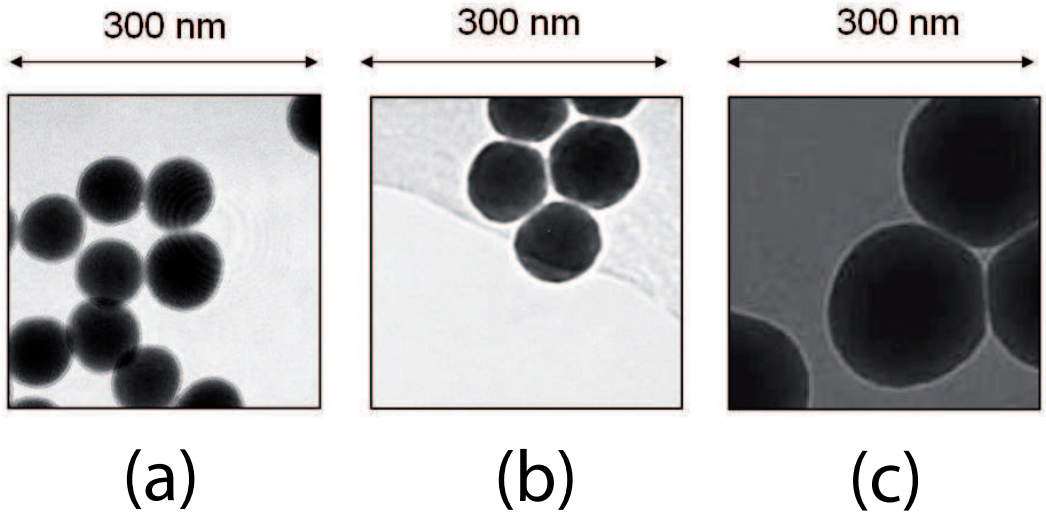

Figure 2.2: Electron micrographs of SiO_2 nanoparticles of three different sizes. The scale is the same in all micrographs. The central diameter and polydispersity of the nanoparticles is, (a) 63 nm ± 6%, (b) 90 nm ± 5%, and (c) 142 nm ± 4%

Nanoparticles in dispersions are unstable and aggregate to form larger particles unless they are stabilized [44]. There are two main schemes for stabilizing nanoparticle dispersions, namely electrostatic and steric stabilization. In electrostatic stabilization the nanoparticles carry electrical charge which attracts the counterions to the surface of the nanoparticles. This prevents their aggregation with other charged particles due to the repulsion between nanoparticles of identical charge. In steric stabilization, spacious ligands, such as hydrocarbons, are attached to the surface of the nanoparticles which prevent them from aggregating with other particles [58].

2.2 Photoelectric Effect

Illuminating a sample by electromagnetic radiation of sufficiently high photon energy will cause electrons to be emitted from the sample. The emitted electrons are usually called photoelectrons. Hertz and Hallwachs observed this effect and Einstein gave a theoretical treatment of the process [59]. If the energy of the photon $h\nu$ is higher than the binding energy, which is required to remove an electron, the excess energy can be transferred into kinetic energy of the photoelectron according to the following equation:

$$h\nu = E_{Binding} + E_{Kin} \tag{2.1}$$

where E_{Kin} is the kinetic energy of the emitted electron and the binding energy $E_{Binding}$ is given by, if changes in internal energy of the cation induced by the photoionization is neglected:

$$E_{Binding} = E_{Final} - E_{Initial} \tag{2.2}$$

Here E_{Final} and $E_{Initial}$ is the energy of the initial and final states, respectively. If the photon energy is known, measuring the electron kinetic energy thus reveals information on the binding energy. This is the foundation of photoelectron spectroscopy. Often a distinction is made between ultraviolet photoelectron spectoscopy (UPS) and X-ray photoelectron spectroscopy (XPS) depending on the photon energy of the exciting radiation. In ultraviolet photoelectron spectroscopy generally valence electrons are excited whereas in X-ray spectroscopy more tightly bound inner shell electrons are excited [45].

Studying photoabsorption by excitation of inner shell electrons has some notable advantages over valence electrons for molecules and solids. The inner shell electrons, in contrast to the valence electrons, largely have an atomic character which makes the method site- and element-specific, since absorption thresholds of inner shells of different elements are most often well separated from each other in energy. Due to its element- and site-specificity, core level spectroscopy is extensively used to study a variety of materials in different states of aggregation [45, 59–62].

Fig. 2.3 shows different cases of photoexcitation of a schematic atom consisting of an occupied inner shell, an occupied valence shell, and an unoccupied higher lying shell. Fig. 2.3 (b) corresponds to absorption by an electron in the inner shell which is emitted from the atom. Similarly, in Fig. 2.3 (a) the photon is absorbed by a valence electron which is emitted. In both cases, the arrows extend beyond the dashed line that represents the vacuum level, the excess energy is thus transferred into kinetic energy of the electron.

Measuring the absorption of soft X-rays close to inner shell absorption edges provides information on the local chemical environment of the probed atoms by resonantly exciting inner shell electron into unoccupied states near to vacuum level. In Near Edge X-ray Absorption Fine Structure spectroscopy (NEXAFS)

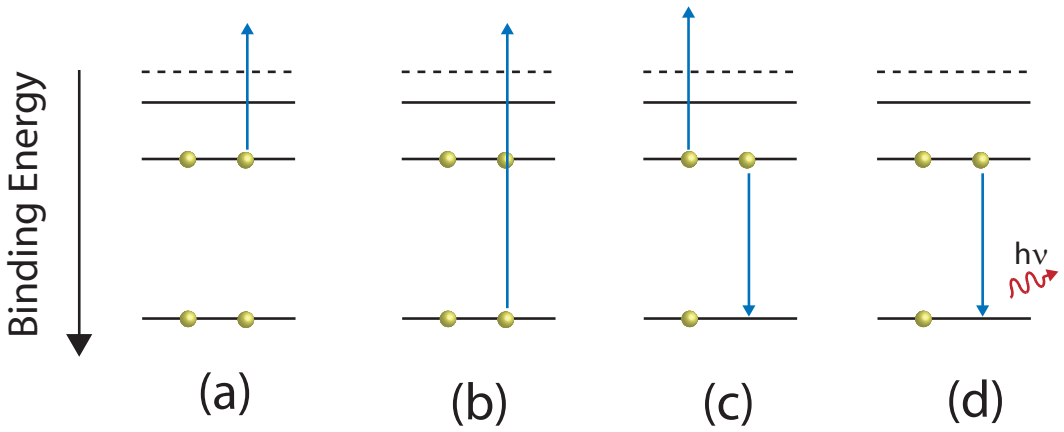

Figure 2.3: Different cases of photoexcitation and core hole decay are shown: (a) is the case of XPS, involving photoionization of an inner shell electron, (b) is the photoionization of a valence electron. (c) and (d) shows decay mechanisms of an inner shell hole, namely Auger decay and X-ray fluorescence, respectively.

the region of -10 eV to +40 eV around an inner shell absorption edge is typically studied. In Fig. 2.3 this corresponds to exciting an electron into the unoccupied level.

2.2.1 Core Hole Decay

An atom with an inner shell vacancy is highly unstable and the vacancies are filled by another electron [63]. A core hole decay can happen *via* fluorescence, in which the core hole is filled by an electron and the excess energy is emitted by fluorescence or *via* a non-radiative process where the hole is filled by an outer shell electron and another one is emitted, which is known as the Auger effect. The kinetic energy of Auger electrons depends on the energies of the involved levels and not on the photon energy of the absorbed photons. The ratio of radiative to non-radiative core hole decay depends on the element under study and the shell of the excited electron [63]. For heavy elements the

radiative decay channel is the dominant one, whereas the non-radiative decay dominates for light elements. Fig. 2.3 (c) and (d) show these two deexcitation routes. In Fig. 2.3 (c) shows an inner shell vacancy being filled by an electron from the valence shell and transfer of the excess energy to another electron of this electronic shell, which leaves the sample. In contrast to this, Fig. 2.3 (d) shows the deexcitation *via* fluorescence, where the excess energy is emitted in the form of a photon that is indicated by a curly arrow.

2.2.2 Electron Transport in Solids

The difference between the penetration depth of X-rays into materials and the escape depth of the photoelectrons makes photoelectron spectroscopy a surface sensitive method. X-rays can penetrate into solids and so that the absorption of an X-ray photon can take place at or near the surface of the solid or deep within the bulk, depending on the wavelength of the X-rays and the absorption cross section of the sample. If the absorption takes place inside the bulk of the solid, the resulting photoelectron must leave the solid before it can be detected. In nanoparticles, the fraction of atoms which are situated at or near the surface is higher than in bulk solids. Therefore, photoelectron spectroscopy is a specifically suitable method to study nanoparticles. The depth from which electrons can escape is called the escape depth and depends on the kinetic energy of the electrons [64–67].

Fig. 2.4 shows a Monte-Carlo simulation of the trajectory of an electron of 100 eV kinetic energy when impinging on a SiO_2 surface as well as the trajectories of secondary (SE in Fig. 2.4) and tertiary electrons created (TE in Fig. 2.4) [68, 69]. The Figure shows that the primary electron moves a short distance before losing energy and creating secondary electrons which have a significantly longer inelastic mean free path due to their low kinetic energy. In the example

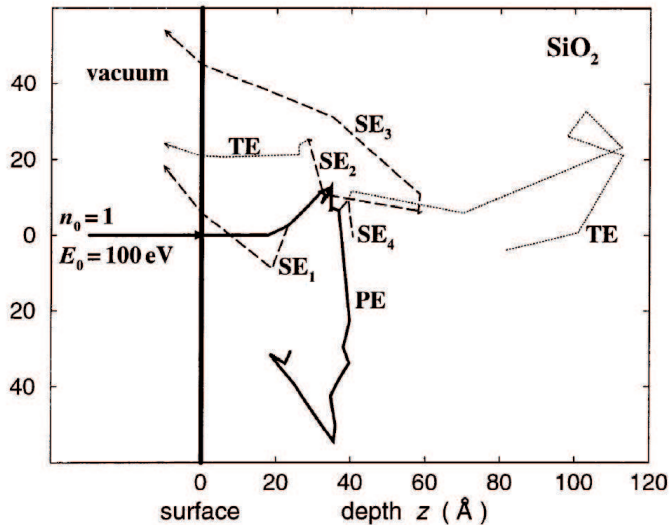

Figure 2.4: Simulation of the trajectory of an electron with 100 eV kinetic energy when impinging on a SiO_2 surface. Through inelastic scattering, the primary electron causes secondary electrons that may or may not leave the surface. The Figure is taken from [70].

that is shown, the primary electron causes the emission of three electrons from the SiO_2 surface.

2.3 Strong Field Ionization

The interaction of matter with intense electric fields, such as from ultrashort laser pulses varies with the strength of the laser field [71–73]. Different ionization mechanisms in strong field ionization are illustrated in Fig. 2.5, where the intensity of the electric field increases from left to right. In Fig. 2.5 (a), the photon energy is lower than the ionization energy so that single photon ionization cannot take place. However, if more than one photon of this photon energy is absorbed, ionization can take place if the sum of the photon energies exceeds the ionization threshold. In Fig. 2.5 (a), the ionization is reached by

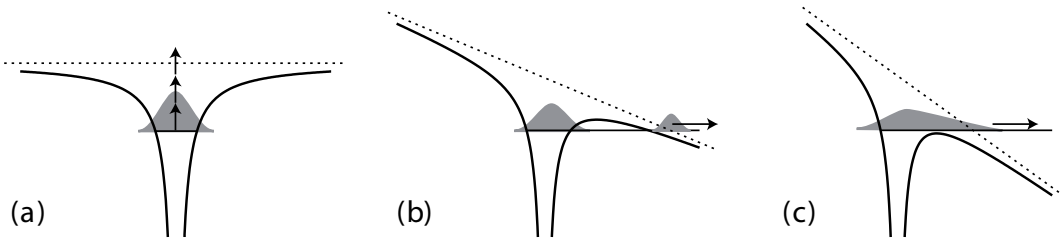

Figure 2.5: Different ionization mechanisms in strong laser fields. (a) is multi-photon ionization, (b) is tunnel ionization and (c) is over-the-barrier ionization. the Figure is taken from [72].

absorption of three photons. In Fig. 2.5 (b) the Coulomb well is distorted due to the strong laser field which leads to a barrier that the electron can tunnel through into the vacuum. Fig. 2.5 (c) shows over-the-barrier ionization where the barrier is suppressed below the ground state, leaving the electron unbound [72, 74].

Which one of these ionization mechanism dominates depends on the strength of the field and the ionization energy of the atom. The Keldysh parameter γ is used to identify which process will dominate.

$$\gamma = \sqrt{\frac{IP}{2U_p}} \tag{2.3}$$

where IP is the ionization potential of the atom and U_p is the ponderomotive potential given by $U_p = \frac{e^2}{4m\omega^2}E^2$ which is the mean quiver energy of the free electron in the oscillating laser field. In the case $\gamma >> 1$, multiphoton ionization dominates, whereas tunnel ionization dominates for $\gamma << 1$. As the intensity is increased, the change from the multiphoton ionization regime to the tunnel ionization regime is not abrupt, and in the range of $\gamma \approx 1$ both processes can take place [72].

The intensity dependence of the ionization yield is different for multiphoton

ionization and tunnel ionization. The electron yield from multi-photon ionization involving n photons is proportional to the intensity of the laser pulse to the power of the number of photons needed for the ionization [75].

$$Yield \propto I^n \tag{2.4}$$

In contrast to this, the tunnel ionization rate is given by the Ammosov-Delone-Krainov rate that is also a highly nonlinear function of the laser electric field [76].

$$Yield(t) = AE_{IP}(\frac{4\sqrt{2E_{IP}^3}}{\mid E(t) \mid})^{2n*-|m|-1}e^{(} - \frac{4\sqrt{2E_{IP}^2}}{3 \mid E(t) \mid}) \tag{2.5}$$

Where $E(t)$ is the instantaneous electric field, E_{IP} is the ionization energy of the atom. n^* and m are the effective principle quantum number and the projection of the angular momentum on the laser polarization direction, and A is a constant. The maximum of the ionization rate coincides with the maximum of $E(t)$.

2.3.1 Electron Rescattering

After being emitted into the continuum, the electron will continue to be influenced by the laser field and can be accelerated away from the ion. Depending on the birth time of the electron, which is the time within the laser pulse when the tunneling takes place, it may be driven back to the ion once the linearly polarized field changes its direction and returns back to the ion. In the classical model introduced by Corkum and Kulander the ionization, propagation of the electron in the vacuum, and the interaction of the returning electron with the ionic residue are treated in three separate steps [76]. Consequently, this model is called the three step model.

The interaction of the returning electron with the remaining ion gives rise to numerous phenomena of strong field physics. If the returning electron recombines with the ion to form a neutral, it can emit its energy (the energy acquired during the propagation in the vacuum in addition to the ionization potential) as a photon. This is the process responsible for high harmonics generation [77–79]. A second process through which the returning electron can interact with the remaining ionic core is scattering, either inelastically or elastically. In the inelastic scattering case the incoming electron leads to the emission of a second electron or higher ionization events *via* collitional ionization. This is known as non-sequential double or multiple ionization depending on the charge state of the final ion [80].

The elastic case can lead to further acceleration of the electron and gives rise to high order above-threshold ionization [81, 82]. This process is of special interest in the present work. Fig. 2.6 shows these different cases schematically. In Fig. 2.6 (a) direct electron emission is shown where the electron never returns to the ionic core, and (b) an electron returning to the ionic core, where it (i) recombines with the ionic core under emission of a photon, (ii) is elastically scattering from the ionic core, and (iii) inelastically scattering from the ionic core causing collisional ionization, which leaves the ion doubly or multiply charged.

In the three step model, the equation of motion of the electron in the oscillating field $E_0 sin(\omega t)$ after tunnel ionization is given by [83]

$$\ddot{x} = \frac{e}{m} E_0 \sin(\omega t) \tag{2.6}$$

where m and e are the electron's mass and charge respectively. The electron starts its propagation at the time t_0 at the origin $x = 0$ with no kinetic energy.

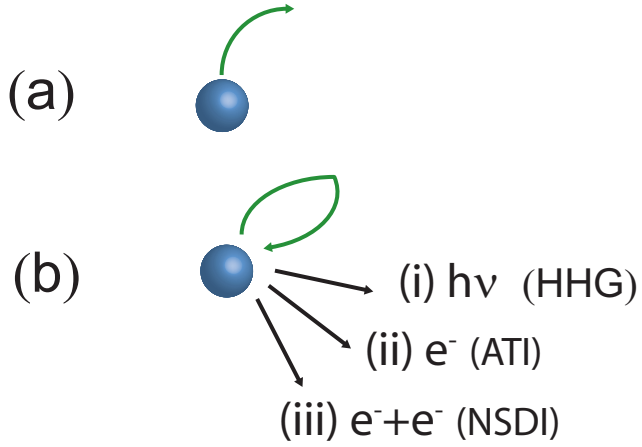

Figure 2.6: Schematic representation of processes following tunnel ionization in the three step model: (a) direct emission, where the electron never returns to the origin and (b) processes that can occur when the electron returns to the origin. The blue sphere represents an atom and the green arrows represent the electron propagation in the vacuum after tunnel ionization. See text for details.

The birth time puts restrictions on whether the electron can return to the ionic core and the kinetic energy that is acquired. The electron returning to the ion at the time t_1 thus corresponds to $x(t_1) = 0$. To find out at what times the electron will return to the origin, Eq. 2.6 is integrated to give the following expression for the first return time, t_1, [83]

$$sin(\omega t_1) - sin(\omega t_0) = \omega(t_1 - t_0)cos(\omega t_0) \tag{2.7}$$

depending on the birth time, the electron can return to the origin once, many times, or never.

The electron's velocity components at the time t after it is elastically scattered by an angle θ_0 with respect to the direction of motion before the scattering

event is given by

$$m\dot{x}(t) = -\frac{eE}{\omega}(cos(\omega t) - cos(\omega t_1) + cos(\theta_0)(cos(\omega t_1) - cos(\omega t_0))) \quad (2.8)$$

$$m\dot{y}(t) = -\frac{eE}{\omega}sin(\theta_0)(cos(\omega t_1) - cos(\omega t_0)) \quad (2.9)$$

This leads to the kinetic energy of the electron, if measured by a detector outside the field, to be the time-averaged kinetic energy in the field [83]:

$$E = 2U_P((\cos^2(\omega t_0) + 2((1 - cos(\theta_0))cos(\omega t_1)(\cos(\omega t_1) - cos(\omega t_0)))) \quad (2.10)$$

Equation 2.10 thus reveals that the highest electron kinetic energies of electrons that scatter elastically from the ionic core occur for $cos(\theta_0) = -1$, corresponding to an angle $\theta_0 = 180°$, which implies that they are backscattered.
If the electron returns when the amplitude of the field changes sign and is backscattered ($\theta_0 = 180°$) it can be further accelerated by the field for another half-cycle to gain additional energy. The maximum kinetic energy that the electron can acquire is E_{Kin}=10.007 U_P in the classical model [84].
The birth time of the electron influences the number of times it can return to the origin and its kinetic energy. Fig. 2.7 shows (a) a linearly polarized laser field and (b) trajectories of electrons with different birth times for tunnel ionization. Trajectory (1) corresponds to an electron born at 0° that never returns to the origin. Trajectory (2) is for an electron born at 90° which corresponds to the maximum amplitude of the field and therefore to the highest electron yield (cf. Eq. 2.5). This results in the electron returning to the origin but gaining no drift energy. Trajectory (3) for an electron born at 107° leads to a return of the electron when the sign of the field changes, and if the electron is elastically backscattered it can be further accelerated leading to the highest

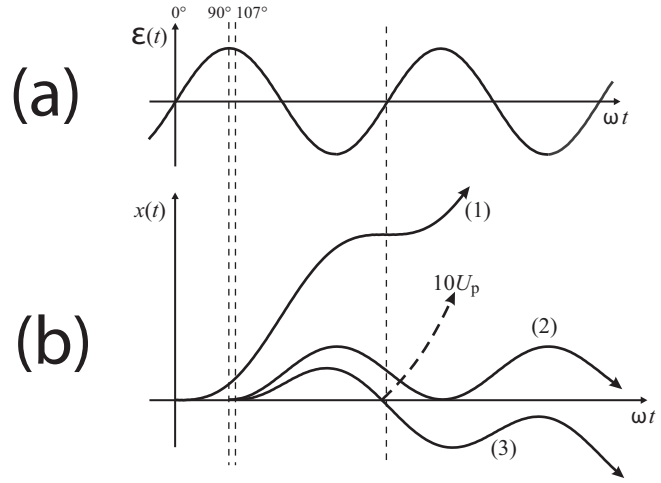

Figure 2.7: Electron trajectories after ionization in the field shown in (a). In (b), trajectory (1) is for of an electron with a birth time of 0° where the electron never return to the origin, whereas (2) and (3) are both at 90° and 107° leading to them returning to the origin. The electron with birth time at 107° (3) returns when the field changes sign and can through elastic scattering at the ion be further accelerated up to 10 U_P. The Figure is taken from [80]

kinetic energies of 10 U_P which is indicated by the dashed arrow in Fig. 2.7. As seen from (2) and (3), the birth times leading to the maximum electron yield and those leading to the highest kinetic energies do not coincide [85].

2.4 Elastic Light Scattering from Spheres

Light propagates through a homogeneous medium, such as vacuum, in a straight line. If it encounters some inhomogeneity or obstacle, it may change its direction of propagation. This is referred to as light scattering and may be elastic or inelastic depending on whether the photon energy of the light changes or not [86]. In this thesis, only elastic light scattering is considered for the case that the incoming radiation is in the soft X-ray regime, the homogeneous medium through which it propagates is vacuum and the inhomogeneity it en-

counters is a free spherical nanoparticle in vacuum.

For the special case of a sphere embedded in a homogeneous medium, Mie gave an analytical solution to Maxwell's equation for the interaction of the sphere with light [87]. Although Mie's original motivation was to study the different colors of colloidal gold, his solution is more general and applies to other sizes of a sphere, other materials than gold, and to electromagnetic radiation in other spectral regimes than that of visible light [88, 89].

The Mie solution applies if the objects are homogeneous spheres in a homogeneous environment. The conditions for the light is that it is a plane wave. If these conditions are fulfilled, then the scattering problem can be solved for any ratio between the sphere's radius and the wavelength of the light and for any refractive index of the material.

For the scattered far-field component, the following applies for the angular distribution for polarizations parallel and perpendicular to the plane defined by the polarization of the incoming radiation and its direction of propagation [90]:

$$E_{Scat,Parallel}(\Theta) = \frac{e^{ikr}}{-ikr} \sum_{n=1}^{\infty} \frac{2n+1}{n(n+1)} (a_n \tau_n + b_n \pi_n) \tag{2.11}$$

and

$$E_{Scat,Perpendicular}(\Theta) = \frac{e^{ikr}}{-ikr} \sum_{n=1}^{\infty} \frac{2n+1}{n(n+1)} (a_n \pi_n + b_n \tau_n) \tag{2.12}$$

where π_n and τ_n describe the angular scattering pattern that are weighted by the complex valued factors a_n and b_n. π_n and τ_n are given by the following recurrence relations:

$$\pi_n = \frac{2n-1}{n-1} cos(\theta) \cdot \pi_{n-1} - \frac{n}{n-1} \pi_{n-2} \tag{2.13}$$

and

$$\tau_n = ncos(\theta)\pi_n - (n-1)\pi_{n-1} \tag{2.14}$$

these can be solved by starting with $\pi_0 = 0$ and $\pi_1 = 1$. Fig. 2.8 shows polar graphs of the first five π_n and τ_n. The radial scales in Fig. 2.8 are not to scale between the different function.

The Mie coefficients a_n and b_n are given as [91]:

$$a_n = \frac{\mu m^2 j_n(mx)[xj_n(x)]' - \mu_1 j_n(x)[mxj_n(mx)]'}{\mu m^2 j_n(mx)[xh_n^{(1)}(x)]' - \mu_1 h_n^{(1)}(x)[mxj_n(mx)]'} \tag{2.15}$$

and

$$b_n = \frac{\mu_1 j_n(mx)[xj_n(x)]' - \mu j_n(x)[mxj_n(mx)]'}{\mu_1 j_n(mx)[xh_n^{(1)}(x)]' - \mu h_n^{(1)}(x)[mxj_n(mx)]'} \tag{2.16}$$

Here, the functions j_n and h_n^1 are spherical Bessel functions of the first and third kind of order n with the argument x or mx. The primes denote derivates with the respect to the corresponding argument. x is the Mie size parameter given by $x = \frac{2\pi r}{\lambda}$, where r is the radius of the sphere and λ is the wavelength of the radiation. m is the ratio of the complex refractive indices of the sphere and that of its surroundings. Thus, if the surroundings are vacuum, then m is the material's refractive index.

The sums in Eqs. 2.11 and 2.12 for the angular distribution go to infinity, which is not feasible for practical applications. The following limit is used to consider the number of relevant terms to be considered [89]:

$$n_{max} = x + 4x^{1/3} + 2 \tag{2.17}$$

where x is the Mie size parameter. For the Mie simulations presented in this work, n_{max} is thus of the order of 100. As the Mie size parameter increases, calculating the scattering pattern gets increasingly cumbersome due to the

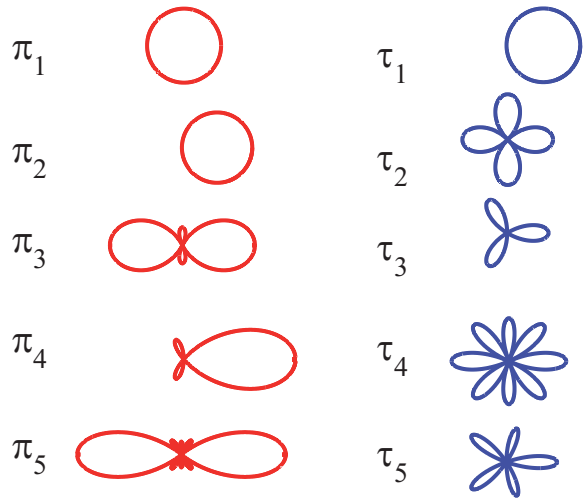

Figure 2.8: The first five angle functions in a polar representation. The different functions are not shown to scale.

increasing number of terms in the sums in Eqs. 2.11 and 2.12.

Fig. 2.9 shows simulations of the angular distributions of the scattered light for different sizes of gold spheres in an aqueous surrounding and is taken from Mie's publication [87]. The wavelength is 500 nm for the incoming radiation. Fig. 2.9 (a) shows the perpendicular (outer curve) and parallel (inner curve) polarization scattering for the limit of an infinitely small sphere, (b) shows the angle resolved scattering pattern for a d=160 nm gold sphere (outer curve is perpendicular and inner curve is parallel polarization), and finally (c) shows the angle resolved scattering pattern using a d=180 nm gold sphere (again, the outer curve is perpendicular and the inner curve is parallel polarization). As the size of the gold spheres increases, the scattering becomes increasingly forward oriented. Furthermore, in Fig. 2.9 (b) and (c) a minimum is formed and its position changes as the size of the sphere is increased (it is located at $\approx 110°$ in Fig. 2.9 (b) and $\approx 120°$ in Fig. 2.9 (c)). In Fig. 2.9, 180° is the direction of propagation of the incoming light. As the Mie size parameter x

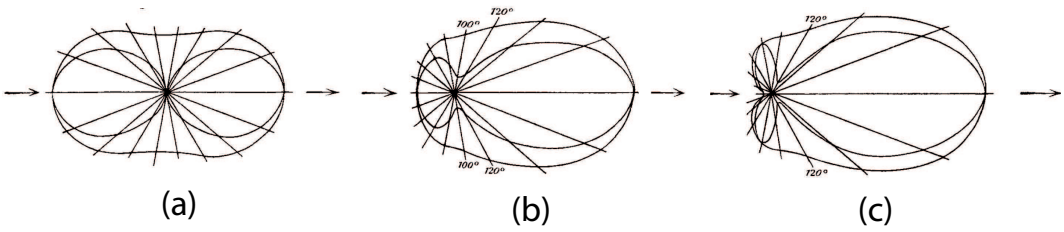

Figure 2.9: Scattering of $\lambda = 550\ nm$ from gold spheres of different size. (a) is the limit of an infinitely small gold sphere, (b) is a d=160 nm gold sphere and (c) is a d=180 nm gold sphere. The Figure is taken from [87].

increases, the scattering becomes increasly forward oriented and a structure of minima and maxima is observed. By measuring the position of these minima and maxima, information may be derived on the size distribution and optical constants of the spherical particle.

Chapter 3

Experimental Setup

The aim of this work is to study nanoparticles in a nanoparticle beam in high vacuum. This approach has the advantage that the nanoparticles can be studied without any interaction with a surrounding medium, which will inevitably be the case if they are deposited on a surface or contained in a dispersion. The second advantage of this approach is that changes to the sample over time, for instance charging when studying photoionization of nanoparticles, can be ruled out, since the interaction time of the nanoparticles with the radiation field is short [92]. After this short time period the nanoparticles leave the interaction region which is continuously fed by pristine sample.

This Chapter will describe how an aerosol of nanoparticles is made out of a dispersion and how the aerosol is subsequently brought into high vacuum. After being transferred into a nanoparticle beam in vacuum, the nanoparticles are studied by soft X-rays as well as ultrashort laser pulses in the visible spectral regime. The radiation sources used in this work will be described as well as the instruments used to analyze electrons emitted and photons scattered from the nanoparticles in the nanoparticle beam.

3.1 Nanoparticle Spraying

The transfer of nanoparticle into an aerosol is achieved by spraying a dispersion containing the nanoparticles at ambient pressure using an atomizer. Fig. 3.1 shows the principle of the atomizer. Compressed air (or another gas or gas mixture) is expanded through an orifice to form a high-velocity gas jet. A dispersion containing nanoparticles is sucked up from a reservoir to be turned into a spray of droplets by the gas jet. The output of the atomizer contains droplets which contain nanoparticles. The gas stream containing the droplets is are passed around a 90° turn. Large droplets are unable to follow the gas stream and are efficiently removed from the gas flow and flow back down into the reservoir. Smaller droplet can be carried away by the gas and leave the atomizer [93]. The atomizer used in this work is the model 3076 from TSI [94]. Subsequent evaporation of the liquid yields a dry aerosol of nanoparticles. SiO_2 nanoparticles in an ethanolic dispersion have a tendency to aggregate when they are stored over longer time periods [95]. For this reason, care is taken to treat the dispersions in an ultrasonic bath prior to use to break up possible aggregates. When spraying a dispersion in this manner into the atmosphere, aggregates may also form if more than one nanoparticle is contained in one droplet. This is prevented by diluting the concentration of the dispersions to a point where, on average, one in 100 droplet (assuming no interactions between the nanoparticles) contains a nanoparticle. For SiO_2 nanoparticles with a diameter of 100 nm this corresponds to a mass concentration of 0.8 g/L. Typically the output of the atomizer for SiO_2 nanoparticles is in the order of $5 \cdot 10^6$ particles/cm^3.

Although the SiO_2 are charge stabilized in the dispersion, it would not be expected that the nanoparticles in the nanoparticle beam carry any excess charge, since the counter ions will be contained in the droplet. However, some

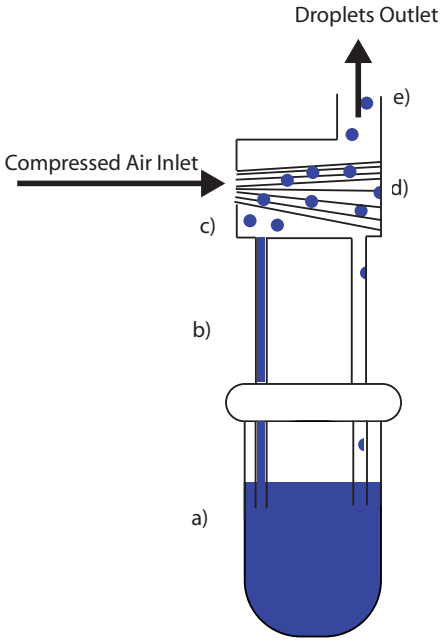

Figure 3.1: Schematic illustration of the atomizer to create an aerosol from a nanoparticle dispersion. Nanoparticles in a dispersion are placed in a reservoir (a), from where they are sucked up to a gas jet (b) where the dispersion is forming droplets (c). Larger droplets collide with a wall (d) and flow back into the reservoir while smaller droplet can leave the atomizer *via* an aperture (e).

excess charge is delivered to the droplets *via* the spraying process. For instance, it has been reported that free NaCl nanoparticles (250-600 nm) prepared by the methods described here carry on average two to three charges [96]. The charge on the particles is not believed to influence their properties greatly, since the charge density is low.

Drying of the droplets sprayed from aqueous dispersions is accomplished by transferring them through polyethylene tubing into a diffusion dryer, which consists of two concentric cylinders. An outer cylinder is filled with hydroscopic silica gel and an inner wire screen cylinder allows transport of the aerosol stream through the dryer without direct contact with the silica gel to prevent particles loss. Water can diffuse through the wire screen inner cylinder into

the silica gel which is periodically dried by heating it overnight at 120°C [97].

3.2 Aerodynamic Focusing

A confinded beam of nanoparticles is created by focusing the stream of particles in a carrier gas by an aerodynamic lens [98–101]. An aerodynamic lens is a cylinder containing a set of apertures through which the aerosol is transported to form a fine beam of nanoparticles during its transport into high vacuum. When an aerosol is sent through the apertures, the gas will contract and expand as it travels through the apertures. Since the solid particles contained in the gas flow have a higher moments of inertia than the carrier gas, they are not able to follow the streamlines of the gas and, if the size of the apertures have been chosen properly, will follow the gas during the contraction in the aperture but they will not follow the subsequent expansion. Instead, they are put on a trajectory that is parallel to the axis of the aerodynamic lens system. Fig. 3.2 shows the principle of aerodynamic focusing when a particle which is embedded in a carrier gas that is initially at a distance R_{pi} from the center of the lens. The gas can expand after traveling through the aperture, but the particle is transferred to a new distance R_po which is closer to the middle of the lens.

There are numerous parameters that can be adjusted to achieve an optimal aerodynamic focusing for nanoparticles of a particular size and density [101]. In this work, the aerodynamic focusing is optimized by varying the diameter of the critical aperture at the entrance of the aerodynamic lens system, which limits the gas flow through the aerodynamic lens and the initial pressure. The diameter of the critical aperture is chosen to be 180 μm for 100 nm SiO_2 nanoparticles. The aerodynamic lens used in the present work is de-

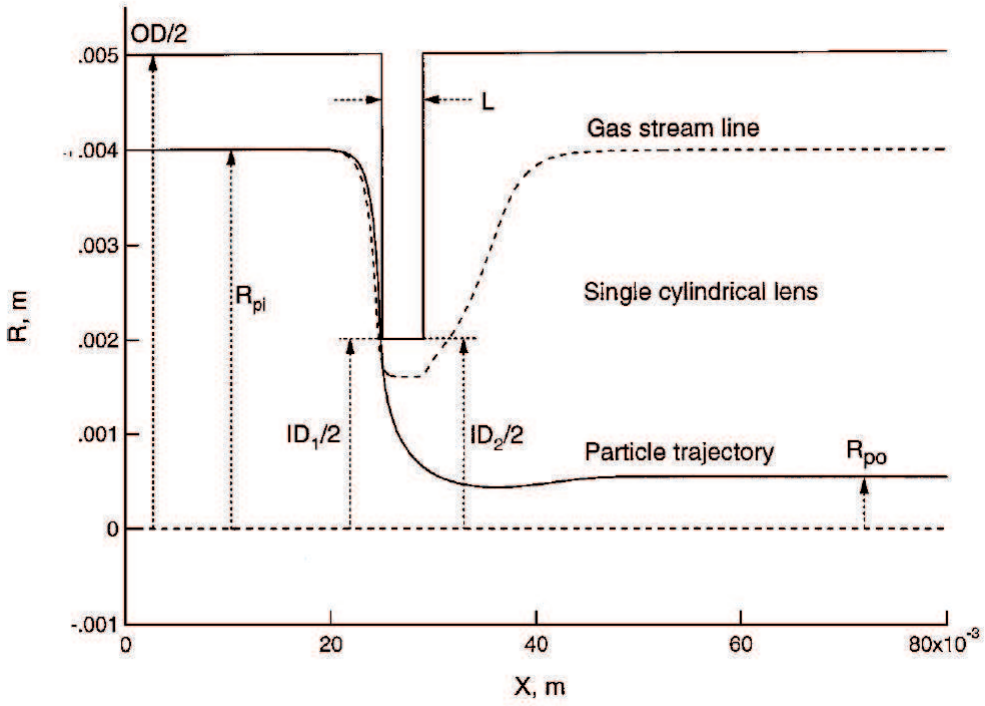

Figure 3.2: Operation principle of an aerodynamic lens. A particle is contained in a gas flow at an initial radial distance R_{pi} and enters an aperture. The gas and the particle move towards the middle when encountering the obstacle. While the gas can expand again as shown by the dotted line, the particle has moved to a radial distance R_{po} which is closer to the center of the aerodynamic lens. The Figure is taken from [102].

signed based on the work of Zhang et al [102, 103]. It has been described and characterized in detail elsewhere [104]. The lens has a length of 30 cm and consists of a critical aperture, 5 subsequent apertures of decreasing diameter and an accelerating nozzle. The diameters of the orifices is listed in Table 3.1.

Fig. 3.3 shows results from a measurement of the width of the nanoparticle beam formed by the aerodynamic lens in the interaction region. The nanoparticles are ionized by synchrotron radiation and the total electron yield is recorded while changing the height of the experimental chamber in a range of 3 mm.

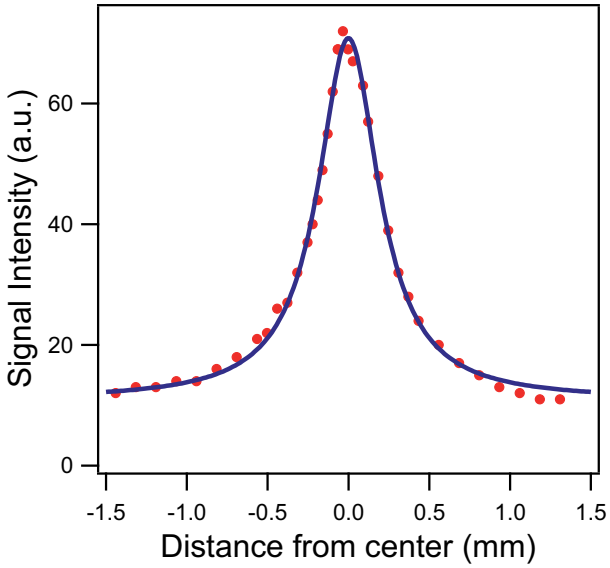

Figure 3.3: Width of the nanoparticle beam in the interaction region with the ionizing radiation. SiO_2 nanoparticles (90 nm ± 6%) are used as a sample. They are ionized with synchrotron radiation (hν=137.9 eV) while recording the total electron yield. The blue line is a fit using a Lorentz function which gives a value of 0.47 mm for the full width at half maximum.

Table 3.1: Diameters of the orifices in the aerodynamic lens setup

Orifice	*Diameter(mm)*
Critical aperture	*Variable*
First aperture	5.3
Second aperture	5.0
Third aperture	4.7
Fourth aperture	4.44
Fifth aperture	4.24
Accelerating nozzle	3.94

The SiO_2 nanoparticles in Fig. 3.3 have a diameter of 90 ± 5% nm, the critical aperture has a diameter of 180 μm and a photon of 137.9 eV is used. The shape of the nanoparticle beam could best be described by a Lorentzian function which is in agreement with previous results reported by Bresch for NaCl

nanoparticles [104]. The fitted function has a width 0.47 mm (FWHM).
Testing of aerodynamic lenses to help finding optimal aperture sizes, carrier gas, and pumping conditions for a particular application can be done by using the aerodynamic lens calculator developed by Wang and McMurry [105, 106].

3.3 Vacuum Apparatus

After leaving the accelerating nozzle of the aerodynamic lens, the fine particle beam travels downstream through a differential pumping stage that connects the outlet of the aerodynamic lens with the high vacuum ($\approx 10^{-}7$ mbar) of the interaction region. The differential pumping stage consists of three sections with decreasing pressure as shown in Fig. 3.4. The pressure in the first section of the stage is carefully monitored as it is found that the critical aperture of the aerodynamic lens has a tendency to get clogged by particles. A drop in pressure is a sign of lower gas flux through the critical aperture indicating that it needs to be cleaned. After the nanoparticle beam leaves the differential pumping stage it enters a spherical vacuum chamber. Different setups for detecting electrons or photons can be attached to the this chamber allowing to study of free nanoparticles using a variety of different experiments.

3.4 Faraday Cup Electrometer

Opposite to the aerodynamic lens a Faraday Cup electrometer is installed to monitor the flux of nanoparticles through the interaction area. Its operational principle is to collect the nanoparticles on its surface and, since some of them carry excess charges, measuring an electrical current [107]. If the particles are given a well defined, known, charge distribution, for instance through neutral-

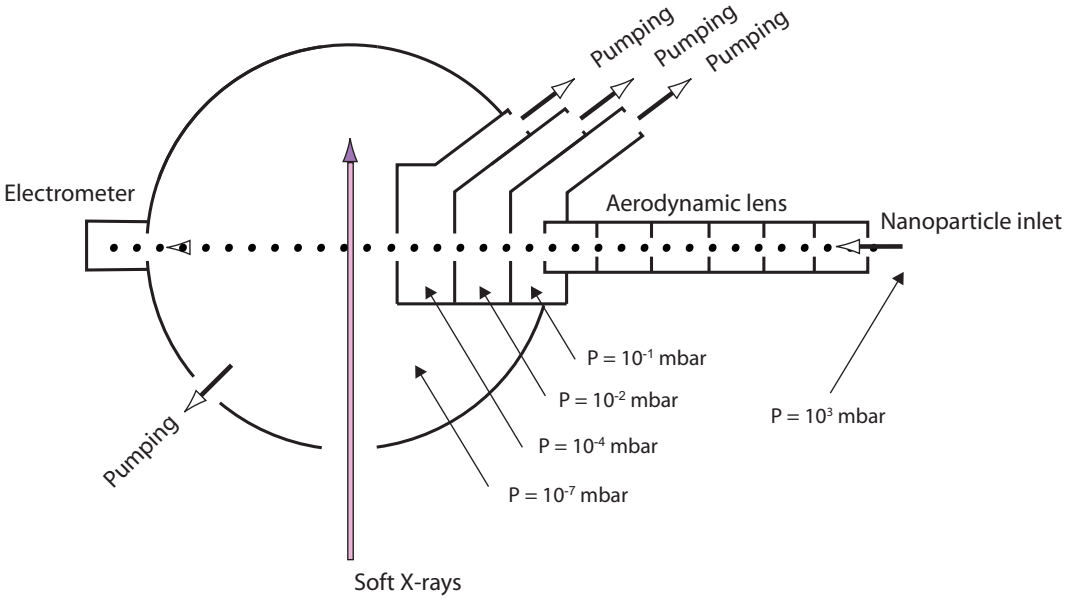

Figure 3.4: Schematic diagram of the experimental setup used in this work to study free nanoparticles. An aerosol of nanoparticles enters from the right into an aerodynamic lens which focuses the particle beam to a diameter of ≈ 500 μm diameter (FWHM). After traveling through a differential pumping stage, the nanoparticle beam is crossed either by a beam of soft X-rays or a beam of few-cycle laser pulses in high vacuum. The vacuum chamber is modular and allows to connect different detection schemes for studied on electrons, ions or photons.

ization by a radionuclide [108,109] or a corona discharge [110], an electrometer may in principle be used to determine the absolute number of nanoparticles reaching the Faraday cup [101]. The electrometer has two purposes: Firstly, it can be used as a monitor for the nanoparticle flux. Any changes in particle flux is monitores, so that e.g. clogging of the critical aperture is noticed. Secondly, it proves to be a useful tool to establish the spatial overlap between the nanoparticle beam and the soft X-rays. At the beginning of an experiment, the overlap between the nanoparticle beam and the soft X-rays has to be established. This sometimes proves to be cumbersome work. By monitoring the

signal on the electrometer due to the nanoparticles and the spot of zero order light from synchrotron radiation on a window at the back of the chamber, a retractable needle is used to iteratively establish an overlap between the soft X-rays and the nanoparticle beam.

3.5 Radiation Sources

Electromagnetic radiation is used in all parts of this work to study properties of free nanoparticles. Use is made of two kinds of radiation sources whose output differs substantially with respect to their time structure and photon energy. These two radiation sources are synchrotron radiation and ultrashort pulse lasers.

3.5.1 Synchrotron Radiation

Synchrotron radiation is emitted when charged particles are accelerated. In a synchrotron radiation facility most often electrons are accelerated to relativistic velocities and injected into an electron storage ring through which they are made to circulate by magnets. At designated positions in the storage ring radiation is generated either at the bending magnets or at injection devices, where the radiation is guided through beamlines from the storage ring to experimental stations. In the beamlines the radiation is directed by optical elements, monochromatized and focused onto the experimental region within an experimental station. Letting the electrons circulate in a ring makes it possible to connect several beamlines to a single electron storage ring so that experiments at many stations can be performed simultaneously. Various modes of operation of synchrotron radiation facilities have been described extensively elsewhere [111–113].

Synchrotron radiation has found a wide-spread use in many branches of science because of its high brilliance and wide tunability for monochromatic radiation. For instance, the synchrotron radiation BESSY II, where most of the work described in this thesis is carried out, offers users radiation ranging from the far-infrared to hard X-rays.

The electrons in an storage ring are not uniformly distributed in the storage ring. They are rather contained in discrete buckets, known as electron bunches. The synchrotron radiation facility BESSY II in Berlin has different modes of operation that differ in the number of electron bunches stored in the ring and in the length of the electron bunches. The two modes of operation that are of interest in this work are the multi bunch and single bunch modes of operation. In the single bunch mode one electron bunch circulates in the storage ring. The round-trip time of the electron bunch in the ring is 800.5 ns (repetition rate: 1.25 MHz) which defines the time between two consecutive flashes of radiation. For the measurements presented in Chapter 4 this clear time structure of the radiation is used to perform time-of-flight measurements of emitted electrons using the arrival time of a radiation flash as the zero-point of the time scale. The length of such a flash of soft X-rays is approximately 30 ps.

In the multi bunch mode numerous electron bunches are stored in the ring simultaneously (up to 340) which increases the photon flux that is available for experiments. The measurements in Chapter 5 are performed during multi bunch mode since a high photon flux is important for those experiments, whereread time resolution is of no importance.

The measurements discussed in Chapter 4 are carried out at the beamline UE56/2-PGM-1 at BESSY II in Berlin, Germany [114] with the exception of the near edge X-ray absorption fine structure spectra that are carried out at

the PLEIADES beamline at the SOLEIL synchrotron radiation facility in Gif-sur-Yvette, France. The measurements discussed in chapter 5 are carried out at the UE52-SGM beamline at BESSY II in Berlin, Germany [115].

3.5.2 Short Pulse Lasers

The measurements using ultrashort laser pulses are discussed in Chapter 6. They are performed at the AS5 beamline at the Max-Planck Institute for Quantum Optics in Garching, Germany. The laser setup is shown schematically in Fig. 3.5 and a detailed description can be found in Ref. [116]. Transform-limited laser pulses of $\approx$ 25 fs pulse length [117, 118] that are the output of an amplified Ti:sapphire laser system (Femtopower Compact Pro, Femtolasers) are spectrally broadened through self-phase modulation in a 1 m long hollow-core fiber filled with neon [119, 120]. The spectrally broadened pulses are compressed to a pulse duration of $\approx$ 5 fs by a chirped mirror compressor. The length of the compressed pulses can be tuned by varying the pressure in the hollow-core fiber. A feedback loop is used to stabilize the phase of the laser pulses [121, 122]. Changing the phase of the laser pulses is achieved by inserting a pair of fused silica wedges into the beam path. Transform-limited Gaussian laser pulses with a length of 5 fs have a spectral width of $\approx$ 150 nm (FWHM) [123].

3.6 Recording Elastically Scattered Soft X-Rays

The setup to measure elastic scattering of soft X-rays from free nanoparticles is shown schematically in Fig. 3.6. An X-ray sensitive CCD camera (Andor DX440-BN [124]) is positioned in vacuum 134 mm away from the scattering center. A movable mechanical beam dump is positioned in front of the CCD

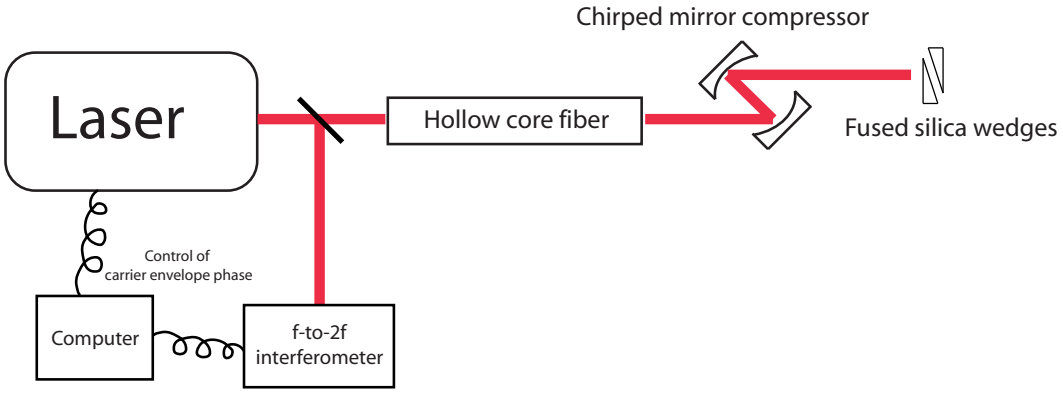

Figure 3.5: Schematic diagram of setup to generate few-cycle laser pulses with a well defined and controllable waveform. See text for details.

chip to prevent damage by the primary beam of soft X-rays. The beam dump is then retracted to allow scattered soft X-rays to be detected. The chip of the camera is internally cooled to -70°C to reduce noise and a liquid nitrogen cooled copper plate is positioned next to the chip, acting as a cold trap to protect the sensitive chip from any condensable substances. Conversion of the pixel scale of the camera into an angle scale is achieved by minimizing the flux of soft X-rays and retracting the beam dump completely. The resulting image that can be recorded is assumed to correspond to the position of the primary beam. Using this position as the starting point of the angle scale, the distance between the nanoparticle beam and the chip and the size of one pixel (13.5 x 13.5 μm^2) is used to calculate the angle scale. Figure 3.7 shows a typical scattering pattern in the small angle regime, as recorded by the X-ray sensitive CCD camera. The red curve is recorded while nanoparticles are introduced into the interaction area and the blue one without nanoparticles. The beam shutter blocks the angle range below 1.2°. Since the soft X-ray scattering is mainly forward oriented (cf. Chapter 5), this implies that the most intense part of the scattered X-rays is also blocked. After accounting

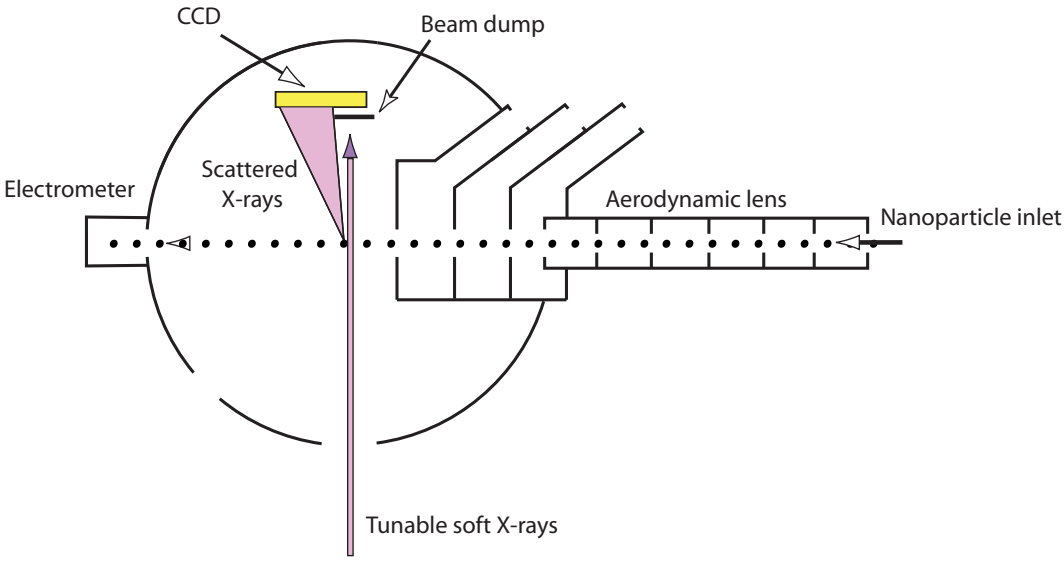

Figure 3.6: Setup for measuring elastic scattering of soft X-rays from free nanoparticles. Soft X-rays that are elastically scattered from the nanoparticles in the nanoparticle beam are recorded by an X-ray sensitive CCD camera. A movable beam dump blocks the primary beam of soft X-rays to prevent damage to the camera.

for different photon fluxes, the difference between these two measurements is used for further analysis. In the course of the experiment, a compromise has to be found between keeping the beam shutter as much open as possible to be able to record measure as small scattering angles as possible and keeping the number of recorded counts per unit time low. This is required to keep the duty cycle of the data acquisition high, where data acquisition time should be long relative to the readout time of the CCD-chip. Furthermore, a smearing out of scattering features is observed if the acquisition time is not much longer than the readout time. For each of the measurements discussed in Chapter 5, one measurement with nanoparticles and one without nanoparticles is made. This also required to normalize the scattering patterns to the incident photon flux. The difference between these measurements is used for further analysis.

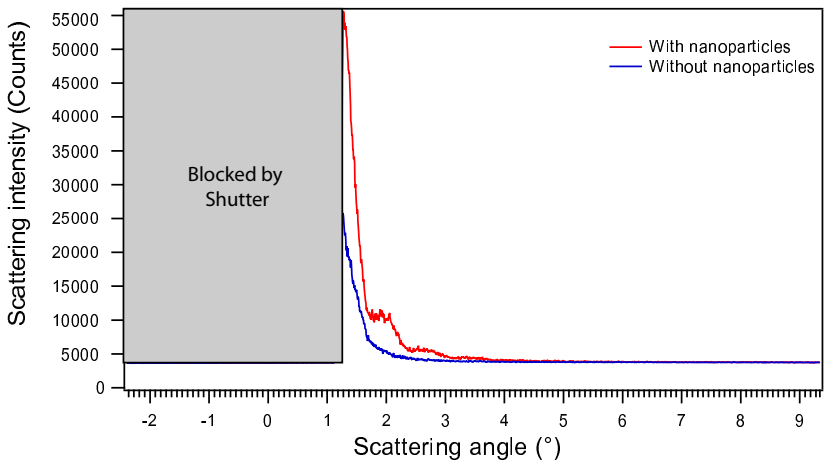

Figure 3.7: Typical image taken by the CCD camera with and without SiO_2 nanoparticles (hν=550 eV, d=183 nm). The difference between the two curves is due to elastic scattering from the nanoparticles. The angle regime below 1.2° is blocked by a mechanical beam shutter to prevent damage to the CCD chip from direct exposure to the primary soft X-ray beam.

The angular resolution of the system is determined by a number of factors:

- The size of the pixels of the CCD camera (13.5 μm x 13.5 μm) leads to a resolution of 0.006° when the camera is located 134 mm from the scattering region.

- The bandwidth of the synchrotron radiation may in principle cause smearing out of the scattering patterns [125]. In this experiment, the smearing out due to the bandwidth is negligible ($E_{h\nu}/\Delta E_{h\nu} > 1000$).

- The width of the nanoparticle beam in the scattering region is about 500 μm in full width at half maximum. If the measured signal is a sum of X-rays scattered from nanoparticles in different regions of the nanoparticle beam, this will lead to smeared out scattering patterns. This contribution is estimated to be 0.004-0.034 ° in the angle region 1.2-9.3°.

- The width of the focus of synchrotron radiation. If the full width at half maximum of the focus is assumed to be 40 μm, this leads to an estimated resolution of 0.017°.

If these contributions are all assumed to be uncorrelated, the root-sum-square of these quantities gives the overall angular system resolution:

$$d_{Angle} = \sqrt{(0.006°)^2 + (0.004°)^2 + (0.017°)^2} = 0.018° \tag{3.1}$$

This value refers to an angle of 1.2 °. For larger angles, the resolution will be lower. For example, at the highest scattering angle of 9.3 ° that can be detected by the CCD camera, which is due to the size of the CCD chip, the angular resolution is reduced to 0.038°. It will be shown that the size distribution of the nanoparticles has a significantly larger influence on smearing out of the scattering signal than the above mentioned factors. Since all measurements are done on a large number of particles, contributions from different sizes will add up and smear out the minima and maxima of the scattering patterns. Most significantly, narrow size distributions, i.e. a low polydispersity of the samples, will lead to more pronounced scattering features.

3.7 Time-of-Flight Electron Spectrometer

In the experiments discussed in Chapter 4, the beam of free SiO_2 nanoparticles is crossed by a beam of monochromatic tunable soft X-rays and extreme ultraviolet radiation, respectively. In Fig. 3.8, the experimental setup is schematically shown. The emitted electrons are collected using a home-built magnetic bottle type electron spectrometer, which is based on the design of Cheshnovsky et al. [126]. In the single bunch mode, the round-trip time for the

electron bunch in the storage ring is 800.5 ns, which defines the time between two subsequent pulses of soft X-rays. This is used to measure the flight times of electrons in order to analyze their kinetic energies. The used flight tube has a length of 600 mm. Therefore, the time interval between two photon pulses is too short for the slowest electrons to reach the detector before the next photon pulse arrives. In order to be able to collect these slow electrons, a small (-1.2 V) voltage is applied to the magnet mounted in the ionization region, so that slow electrons are accelerated. Alternatively, a positive voltage can also be applied to the magnet to slow down the electrons in order to increase the resolution of the spectrometer. The calibration of the photon energy scale is done using the Ar $2p \rightarrow 4s$ resonance at 244.390 eV and the Kr $3d \rightarrow 5p$ at 91.200 eV [127].

If no measures are taken to guide the electrons towards the detector, only those electrons that are emitted into the direction of the detector can be detected. The magnetic bottle type spectrometer is designed to provide high detection efficiency for electrons. The principle of operation of a magnetic bottle type spectrometer is an arrangement with a permanent magnet that is mounted close to the ionization region and a solenoid wrapped around a flight tube that leads to the detector which consists of a stack of microchannel plates. This setup ensures an efficient collection of electrons towards the detector [128]. The inhomogeneous magnetic field of the permanent magnet and the solenoid act a magnetic mirror [111]. The principle of operation is shown in Fig. 3.9 where photoelectrons released from the sample near the magnet, so that they are brought on a helical trajectory when moving from a strong field B_i to a weaker uniform field B_f. Typically, a current of 2 A is passed through the solenoid.

The time-of-flight to kinetic-energy conversion is done by ionizing the 2p levels

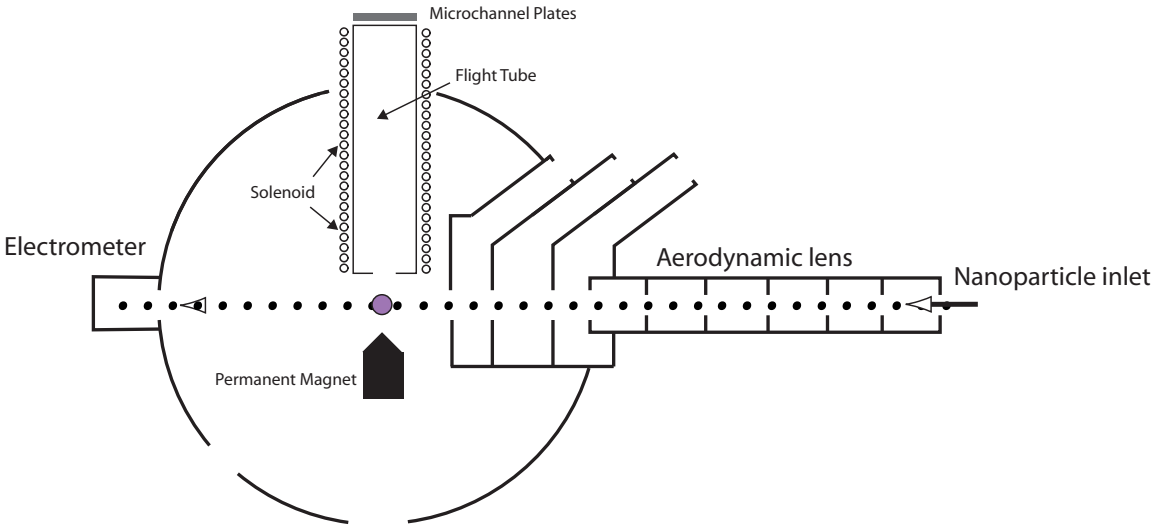

Figure 3.8: A schematic diagram of the experimental setup for time-of-flight measurements of electrons emitted from nanoparticles after excitation by soft X-rays. Unlike Fig. 3.6, the soft X-rays enter the vacuum chamber perpendicular to the plane of the diagram.

of argon and comparing the flight times to the kinetic energies deduced from the known binding energies of 250.6 eV and 248.4 eV for the $2p_{1/2}$ and $2p_{3/2}$ levels, respectively [129]. Typical count rates in the experiment are 10000-20000 counts per second. The repetition rate of the synchrotron radiation is 1.25 MHz, which means that events are detected for every 1 or 2 pulses out of a hundred. The conversion of electron flight times into kinetic energies is performed by using the following formula:

$$E_{Kin} = \frac{m_e}{2q}(\frac{d}{t - t_0})^2 + U_0 \tag{3.2}$$

where m_e is the mass of the electron, q the elementary charge, d the distance between the interaction region and the detector, t_0 is a time offset and U_0 is an accelerator potential.

It can be seen from equation 3.2 that the energy resolution depends on the

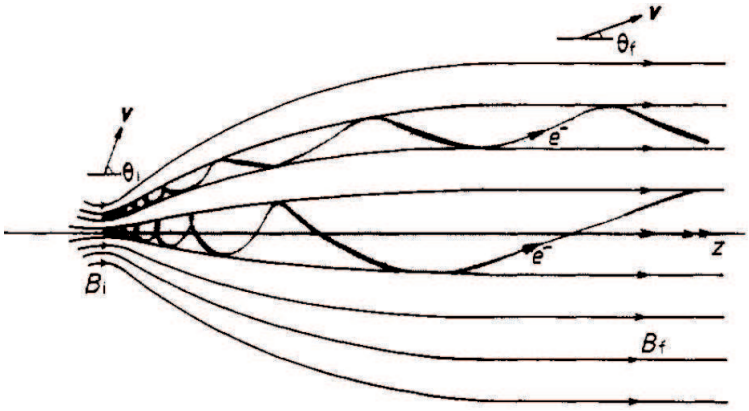

Figure 3.9: Electrons released in the ionization region are brought to helical trajectories when moving from the strong field B_i to the weaker uniform field B_f. The Figure is taken from ref. [128]

kinetic energy of the electrons, since some particular temporal width of the electron signal Δt will lead to different widths in kinetic energy ΔE_{kin}. For short flight times (higher kinetic energies), the resolution is lower than for long flight times (lower kinetic energies). By retarding the electrons, which shifts them to longer flight times (the U_0 in equation 3.2), the resolution of the spectrometer may be enhanced. This, however, prevents electrons emitted with kinetic energy lower than U_0 from reaching the detector at all.

The time-to-kinetic-energy conversion is done in a way that the relative areas under different features in the photoelectron spectrum remains constant [130, 131]. In Fig. 3.10 (a) the time-of-flight spectrum of electrons emitted from d=50 nm SiO_2 nanoparticles after excitation by soft X-rays (hν=137.9 eV) is shown. The flight time spectrum in Fig. 3.10 (a) corresponds to Fig. 4.2 in Chapter 4 before the electron flight times are converted into kinetic energies. As a result of the nonlinear relation between flight times and kinetic energies, the electrons with kinetic energies 90-100 eV arrive within $\approx$ 5 ns whereas those with kinetic energies between 0-10 eV arrive within $\approx$ 400 ns.

Dividing the flight-time spectrum by the first derivative of the flight-time-to-kinetic-energy curve (3.10 (b)) yields the correct signal intensities in the kinetic energy spectrum [132].

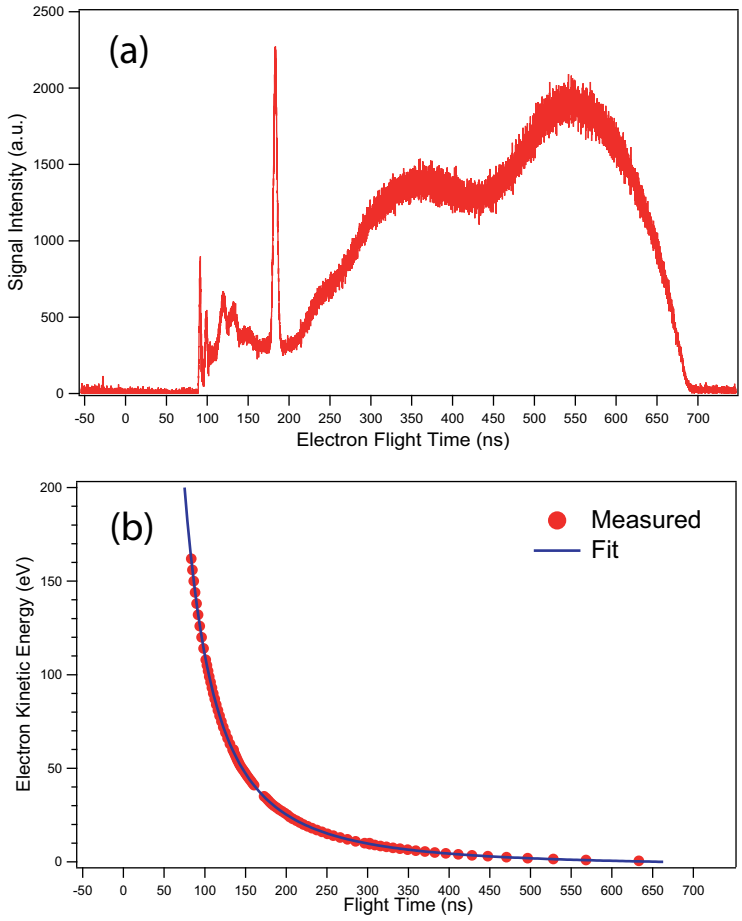

Figure 3.10: (a) is an electron spectrum recorded at 137.9 eV on a flight-time scale. The nanoparticle size is 50 nm. The spectrum corresponds to Fig. 4.2 in Chapter 4 before convertion of the electron flight time to kinetic energies. (b) shows the relation between flight times and the kinetic energy of the electrons. The blue curve is a fit to the data point using equation 3.2.The Ar 2p3/2 photoelectron line is used for the conversion between electron kinetic energies and flight time. The soft X-ray pulse arrives at time=0 and negative values for flight times imply that the radiation pulse has not yet arrived.

Electrons arriving at the end of the flight tube impact on an electron multi-

plier that consists are a pair of microchannel plates that amplify the electron signal. Electrons impacting on the microchannel plates release secondary electrons that can travel through the microchannels while undergoing numerous collision with the channel walls and releasing more secondary electrons. The microchannels have a diameter of 10 μm and are tilted by 8° relative to the surface normal. Typically, a potential of +400 V is applied to the frontside of the microchannel plate stack and +1900 V to the backside to accelerate the electron cloud.

The arrival time of the electrons relative to the arrival time of the flash of soft X-rays is recorded with a time to digital analyzer that can detect up to 14 events in a single cycle with a typical double pulse resolution of 30 ns. The ability to measure more than one event per cycle opens up the possibility to study multi electron coincidences when more than one electron is emitted after the absorption of one photon.

3.8 Velocity Map Imaging

In Chapter 6 the analysis of the electron emission is done not by recording times-of-flight but by recording the impact positions of electrons on a position sensitive detector using the velocity map imaging technique [133]. As with the magnetic bottle type electron spectrometer, velocity map imaging is a high detection efficiency method which allows collecting electrons emitted in a solid angle of 4π. In Fig. 3.11 the experimental setup used in Chapter 6 is shown schematically. The exciting laser beam enters perpendicular to the plane of the paper. The ionization region is situated between two plates termed the extractor plate and repeller plate. A potential is applied to the plates that accelerates the emitted electrons in the direction of the detector. Typically,

+15 kV is applied to the repeller plate and 12 +kV to the extractor plate. After

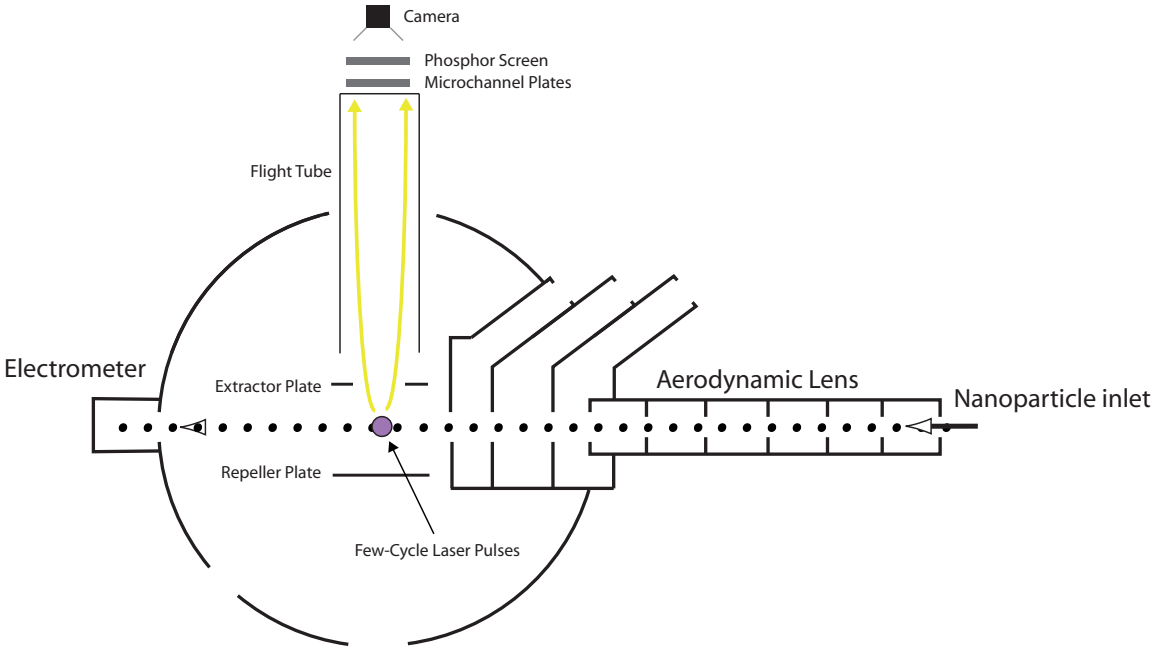

Figure 3.11: Schematic diagram of the experimental setup for velocity map imaging. Few-cycle laser pulses enter the vacuum chamber perpendicular to the page in this diagram. Electrons emitted in the ionization region are accelerated by the repeller/extractor plates towards a microchannel plate stack. The amplified electron signal lands on a phosphor screen where the luminescence is recorded by a CCD camera that is read out by a computer. The yellow curved arrows show two electrons of equal kinetic energy that are emitted in opposite directions.

ionization of a target at time t_0 the emitted electrons move out on expanding spheres with a radius $r(t)$ that depends on the kinetic energy of the electrons:

$$r(t) = \sqrt{\frac{2E_{kin}}{m}}t \tag{3.3}$$

where m is the electron mass. In an imaging spectrometer the expanding spheres are projected onto a two-dimensional position sensitive detector (CCD camera). The impact position of the electrons on the detector is then deter-

mined by their kinetic energy and the emission angle.

If the symmetry axis exits in the detector plane, such as the polarization axis of the laser radiation in this work, one can reconstruct the original three-dimensional distribution from the two-dimensional projection onto the detector. Even if the source of the fragments is not a point source, for example if they are created along a portion of the laser focus, fragments with identical velocity will be projected onto the same point on the detector irrespective of where they are created assuming that a proper voltage ratio is applied to the electrodes of the electrostatic lens. In the experiments described in Chapter 6 the length of the source volume of the emitted electrons corresponds to the width of the nanoparticle beam (cf. Fig. 3.3). This is illustrated in Fig. 3.12 for simulations of trajectories of ions created along a 3 mm line. All charged particles, i.e. ions or electrons, with the same initial velocity will be imaged onto the same point of the detector.

The electron signal is amplified by a stack of two micro-channel plates and the resulting luminescence is projected on a phosphour screen, where the visible radiation is recorded by a CCD camera (PCO, Sensicam) that is situated outside of the vacuum chamber and is read out by a computer.

The two-dimensional projections of the electron cloud onto the detector thus recorded with the camera are transformed into a three-dimensional velocity distribution by using an iterative method. There are different methods for the reconstruction of the original three-dimensional distribution that differ in level of computational cost and how they deal with noise [134–136]. In this work, the method of Vrakking is used [136].

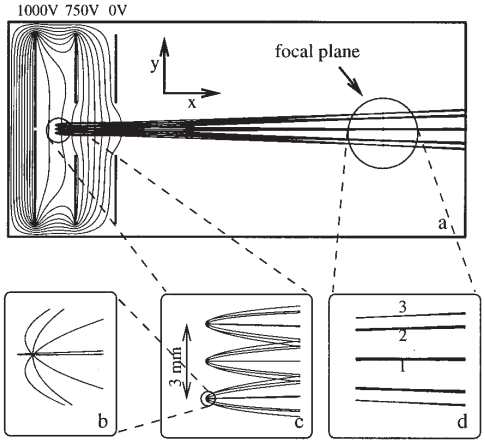

Figure 3.12: Simulated ion trajectories for $V_E/V_R = 0.75$ where V_E and V_R are the potentials applied to the extractor and repeller plates, respectively. The ions are generated along a 3 mm long line. In panel (c), ions are generated at three different points with 1 eV kinetic energy with 45°angle distance. In panel (d), the trajectories of ions with the same emission angle but different starting positions converge in a focussing plane. This Figure is taken from [133]

Chapter 4

Photoemission from Free SiO_2 Nanoparticles

In this chapter the electron emission from free SiO_2 nanoparticles after excitation by extreme ultraviolet radiation and soft X-rays will be used to characterize their electronic structure. Furthermore, electron-electron coincidence spectroscopy reveals emission channels that involve the emission of more than one electron after the absorption of one photon. Photoemission has been used successfully as a site, size and electronic state sensitive method to study clusters and solids [45,67]. In this Chapter, this method will be extended to study free nanoparticles in a nanoparticle beam.

4.1 The Absorption Spectrum of SiO_2

The total electron yield from SiO2 nanoparticles is recorded near the Si 2p and O 1s absorption edges. This approach is used as an approximate measure for the absorption by the nanoparticles [137]. Near-edge X-ray absorption fine structure spectroscopy is a sensitive way to probe the unoccupied orbitals in

matter [36, 138, 139].

In Figure 4.1(a) the near-edge X-ray absorption fine structure spectrum of SiO_2 nanoparticles near the Si 2p absorption edge is shown. The ionization threshold relative to the vacuum level as determined by photoelectron spectroscopy is indicated by a flag (cf. Fig. 4.4). The spectrum shows peaks at 105.75 eV and 106.35 eV that Sutherland et al. [140] assign to $2p_{3/2} \rightarrow a_1^*$ and $2p_{1/2} \rightarrow a_1^*$ transitions, respectively. The peak at 108.4 eV is assigned to the $2p \rightarrow t_1^*$ transition. The error bars in Fig. 4.1 correspond to the statistical error.

The nanoparticles studied in Fig. 4.1 have a diameter of d=90 nm. The measurements are repeated for nanoparticle samples of different size, and the position of the near-edge features at 105.75 eV, 106.35 and 108.4 eV is found to be not influenced by the size of the nanoparticles. This experiment is performed with a spectral bandwidth of 9 meV. The energy positions of the first two near-edge peaks are in excellent agreement with previous findings by Bresch [104] for free SiO_2 nanoparticles, whereas the peak at 108.4 eV is at 0.25 eV higher photon energy than found by Bresch.

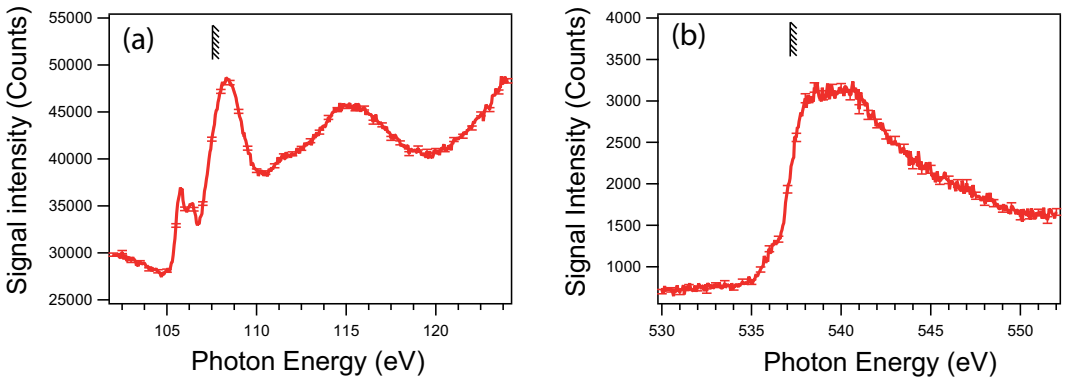

Figure 4.1: Near edge X-ray absorption fine structure spectrum of SiO_2 nanoparticles near the Si 2p (a) and O 1s (b) absorption edges. The ionization thresholds of the Si 2p and O 1s core level electrons as determined with photoelectron spectroscopy are indicated with flags.

Figure 4.1 (b) shows the absorption spectrum near the O 1s absorption edge. Similar to Fig. 4.1 (a), the ionization threshold is determined by electron spectroscopy and is also indicated by a flag. The O 1s near-edge spectrum is less structured than the Si 2p near edge absorption spectrum. The main feature is a broad maximum near 538-541 eV. The assignment of different transitions within this broad feature can be found in ref. [141], but no new information on this aspect comes from the present study. The electron yields represent useful reference data to the results that will be presented in Chapter 5, where the refractive index of SiO_2 nanoparticles in the soft X-ray regime is discussed.

4.2 Emission Spectrum of SiO_2

Unlike total electron yield spectra, that resemble the absorption cross section (cf. Figure. 4.1) and provide information on the unoccupied electronic states of SiO_2 nanoparticles, photoemission provides information on the occupied states. Fig. 4.2 shows the electron emission from SiO_2 nanoparticles (d=50 nm) after excitation by soft X-rays (hν=137.9 eV). This is shown on a logarithmic (a) and a linear (b) intensity scale. The main part of the electron emission is located in a broad feature at low kinetic energies that is attributed to secondary electron emission, which is a result of inelastic scattering of photoelectrons in the bulk of the nanoparticles. Other features are observed corresponding to the emission of Si 2p inner shell electrons, valence electrons and Si LVV Auger electrons. The experiments are performed in two steps: (i) a gas beam containing nanoparticles and (ii) a gas beam without nanoparticles, where only the carrier gas is introduced into the ionization region. After normalization to the photon flux, the difference of both measurements is assumed to be exclusively

due to photoemission from nanoparticles.

Four features have been colored for clarity. The secondary electrons are marked in red color, direct photoemission from Si 2p is in green, Si LVV Auger electrons are marked in blue, and finally valence photoemission is marked in yellow color. The kinetic energy of the direct Si 2p photoelectron is given by the difference between the binding energy relative to the vacuum level and the photon energy. For a photon energy of 137.9 eV, the kinetic energy of the Si 2p electrons is found to be 29.9 eV, and so the Si 2p binding energy is determined to be 108.0±0.2 eV. No spin-orbit splitting can be observed. It has been found in other studies on both free SiO_2 nanoparticles and bulk SiO_2 that the spin-orbit splitting of Si 2p in SiO_2 is not observable [22, 23, 142] and this can be attributed to the disorder of the material [143, 144]. The disorder of the material means that the measured signal is a superposition of signal from Si atoms in slightly different environments that smears out the spin-orbit doublet. The core hole left by the excitation of the Si 2p electron will most likely decay *via* an Auger decay, since the radiative decay, the competing process, has a low probability of the order of 10^{-4} [63]. The emission of the Si 2p electron followed by the emission of an Auger electron corresponds to double ionization after the absorption of one photon. Furthermore, valence electron emission of SiO_2 appears in the kinetic energy range of roughly 110-130 eV, marked in yellow color in Fig. 4.2. The fourth color coded feature in Fig. 4.2 is the emission of secondary electrons. They are arbitrarily colored for kinetic energies lower than 20 eV.

For the electrons with the lowest kinetic energy in Fig. 4.2, the overall resolution is 0.2 eV. At $E_{Kin} \approx 130\ eV$, the kinetic energy of electrons emitted from the top of the valence band, the overall resolution is 6 eV, which is mainly limited by the spectrometer resolution.

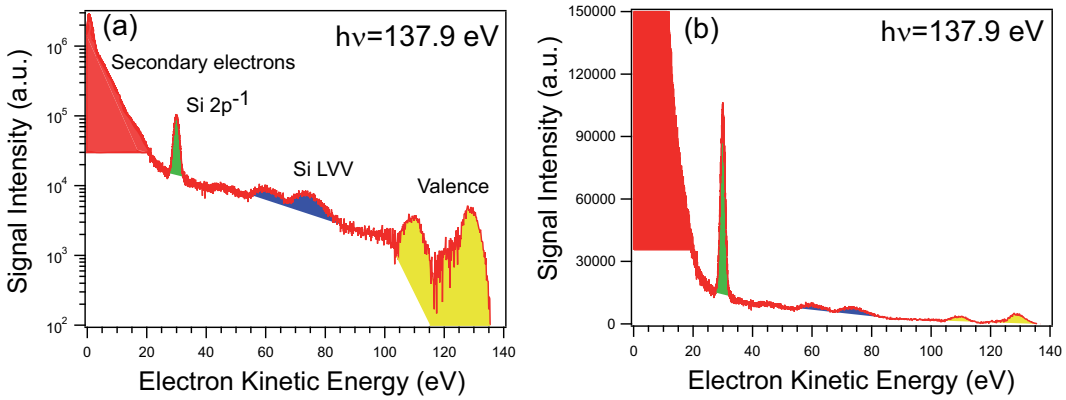

Figure 4.2: Photoelectron spectrum of SiO_2 nanoparticles after excitation by 137.9 eV soft X-rays. For clarity, four regions have been colored. See text for further details.

In order to describe the electron emission from solids, a three step model is proposed by Berglund and Spicer [145, 146]. It considers the photoemission in three steps:

- The absorption process which can take place at different locations within the bulk interior of the particles. The flux of radiation deeper down in the solid is lower than in locations closer corresponding to Beer's law. A measure for the distance the radiation can travel into the solid is the attenuation length, which is the distance after which the photon flux has decreased to $1/e$.

- The second step is the transport of the electrons through the material to reach the surface. In this step the electrons can lose energy due to inelastic scattering events at other atoms. Inelastic scattering can be quantified by the inelastic mean free path, which is the average distance an electron with a given energy travels between successive inelastic collisions [64]. In addition to inelastic scattering, elastic scattering will take place as well [147], but the large collection angle of the spectrometer

leads to any angular information being lost.

- Escape of the electrons from the solids into the surroundings where they can be detected.

The photoemission from solids in the extreme ultraviolet and soft X-ray regimes is to a large degree characterized by the fact that the penetration depth of the radiation is vastly greater than the inelastic mean free path of the electrons. Fig. 4.3 shows values of the attenuation length for soft X-rays and the inelastic mean free path for SiO_2, as reported in refs. [148,149]. For instance, at the photon energy at which Fig. 4.2 is recorded, which corresponds to ≈ 30 eV kinetic energy of the Si 2p photoelectron, the attenuation length of the soft X-rays is about 100 times longer than the inelastic mean free path of Si 2p electrons. For an electron set free in the bulk, the probability that this electron will undergo inelastic scattering on its way to the surface is thus very high. This also means that the case where a photon is absorbed but no photoemission takes place is of non-negligible probability. This is the case where absorption takes place in the bulk of the nanoparticle and the electrons that are set free do not manage to reach the surface before thermalizing in the bulk [150]. The large difference in the penetration depth of the soft X-rays and the inelastic mean free path of the electrons makes photoelectron spectroscopy a surface sensitive approach, as only electrons originating from locations close to the surface will be able to leave the sample.

Figure 4.4 shows the emission in the Si 2p and O 1s regions at a photon energy of 137.9 eV and 567.2 eV, respectively. In Fig. 4.4 (a) the Si 2p binding energy is determined to be 108.0 ± 0.2 eV, which is in accordance with work on thin SiO_2 films [151] as well as 8.2 nm [23] and 300 nm SiO_2 nanoparticles [22] in the gas phase. The blue line is a fit assuming a Gaussian line shape superimposed on a background of inelastically scattered electrons. The binding

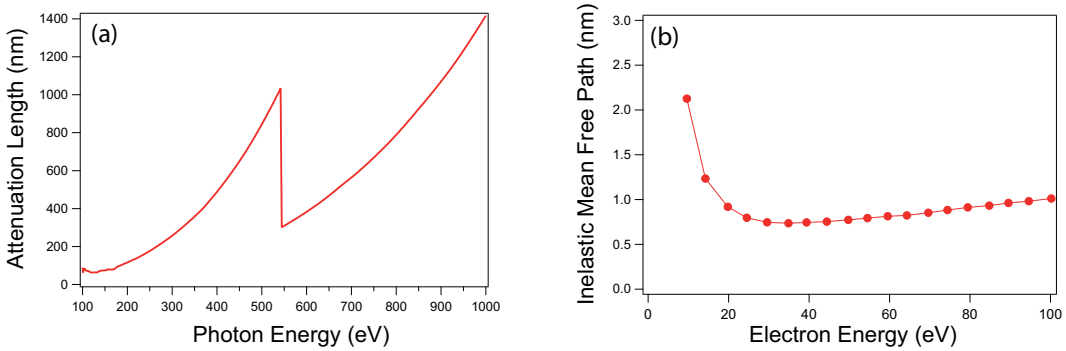

Figure 4.3: Comparison of the attenuation length of soft X-rays in SiO_2 (a) [148] with the inelastic mean free path of electron in SiO_2 (b) [149]. The electron spectrum in Fig. 4.2 is recorded at 137.9 eV. At that photon energy the attenuation length is around 100 nm whereas the inelastic mean free path of the Si 2p electron is about 1 nm.

energy is taken to be the maximum of the curve. Figure 4.4 (b) shows the electron emission in the O 1s regime. The blue line is a fit assuming a Gaussian line shape that is superimposed on a linear background, which is due to inelastically scattered electrons. The binding energy of O 1s is taken to be the maximum of this Gaussian curve and is found to be 537.1 $\pm$ 0.2 eV. Mysak et al. [22] have reported the O 1s ionization threshold of SiO_2 nanoparticles in a particle beam to be 535.7 eV, which is 1.4 eV lower than the value found here. In the study of Mysak et al., two emission peaks are observed corresponding to binding energies of 537.6 eV and 535.7 eV of which the first is assigned to gaseous water and the second to emission from the nanoparticles. There is, however, reason to call this assignment into question, since the O 1s binding energy of gaseous water has been found by other workers to be 539.67-539.88 eV relative to the vacuum level [152–154]. Instead, the ionization threshold found here can be compared to values found for bulk amorphous SiO_2 where the O 1s binding energy has been reported to be 429.2 eV higher than the Si 2p binding energy. This corresponds to a binding energy relative to the vacuum

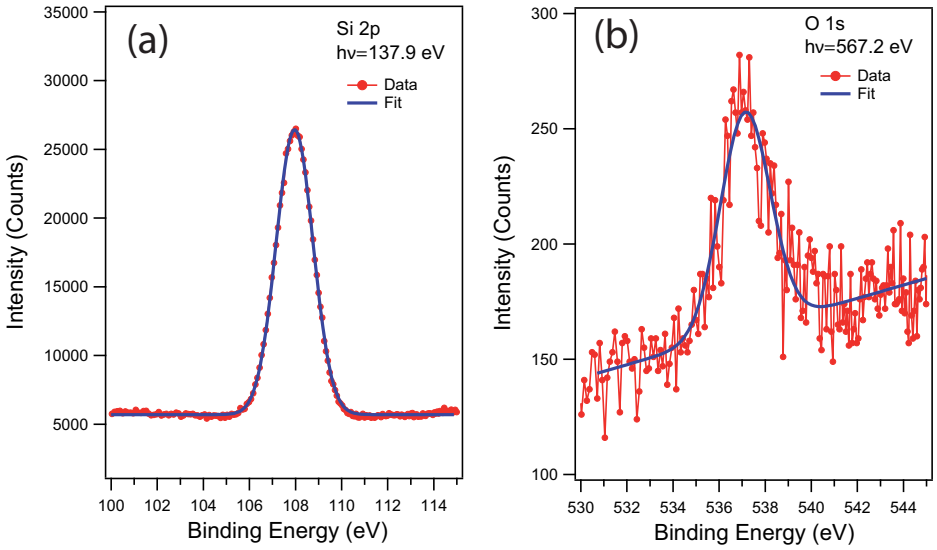

Figure 4.4: (a) the Si 2p regime recorded at a photon energy of 137.9 eV. The Si 2p binding energy is found to be 108.0 ± 0.2 eV; (b) the O 1s regime recorded at a photon energy of 567.2 eV. The O 1s binding energy is found to be 537.1 ± 0.2 eV.

level of 537.2 eV [155]. Since the nanoparticles are sprayed from an ethanolic solution, a signal from the photoelectrons resulting from ionization of the O 1s level of ethanol would also be detectable in this kinetic energy range. The ionization threshold of gaseous ethanol has been reported to be 538.6 eV [156] and no clear sign of ethanol is found in the photoemission spectrum.

Figure 4.5 shows the valence photoemission at a photon energy of 73.1 eV. The resolution due to the spectrometer and the light source for the lowest binding energy electrons (the highest kinetic energies) is estimated to be 1.5 ± 0.1 eV. The estimate is done by measuring the linewidth of Ar $2p_{1/2}$ and comparing it with known natural line widths [157]. Ramaker et al. [158] assign the feature centered at 11.5 eV binding energy which is marked by an 'A' in Fig. 4.5 to orbitals of predominantly nonbonding O 2p character, the feature centered at 16 eV binding energy which is marked by a 'B' to bonding orbitals with O 2p

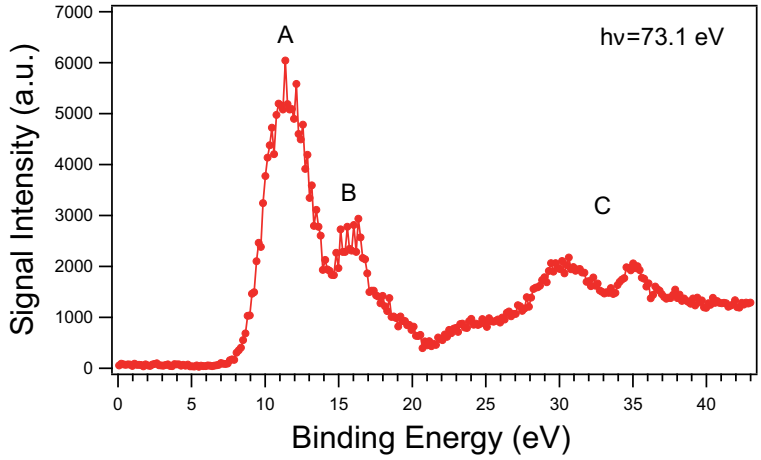

Figure 4.5: Valence photoemission spectrum of SiO_2 nanoparticles (d=50 nm) recorded at 73.1 eV.

added to Si 3s and Si 3p and the feature marked by a 'C' to predominantly O 2s bonding with admixtures of Si 3s and Si 3p. The positions of the tops of the different bands correspond well to the values found by Di Stefano and Eastman [159] with the exception that the two features marked with a 'C' corresponding to O 2s electrons bonding with Si 3p and Si 3s (the $4a_1$ and $3t_2$ orbitals in the T_d notation in ref. [158]) are 5 eV apart in binding energy, whereas they are not resolved in ref. [159]. In Fig. 4.5 it is found for SiO_2 nanoparticles that electrons with the lowest binding energies are located in a tail that extends to 7 eV binding energy. Extrapolating the edge of feature 'A' to zero intensity gives an ionization threshold of 8.5 $\pm$ 0.2 eV. The ionization threshold of the top of the valence band of bulk amorphous SiO_2 relative to the vacuum level has been given as 10.2 eV [160] - 10.6 eV [161]. However, a tail of lower binding energy has also been reported [138] which is attributed to defects involving dangling sp^3 bonds on Si and non-bridging oxygen atoms. This could also be the case for the SiO_2 nanoparticles studied here. It is known that the Si-O-Si network is not perfect in SiO_2 nanoparticles produced by the

Stöber method [56,162]. In the SiO_2 nanoparticles, the Si-O-Si network terminates at either ethoxy or hydroxy groups which results in non-bridging oxygen atoms. This will be discussed in greater detail in chapter 5.

4.3 Secondary Electron Emission

In Figure 4.6 the secondary electron peak from Fig. 4.2 is shown in the kinetic energy range 0-20 eV. The secondary electron emission shows a maximum at $E_{Kin} = 0.6\ eV$ and a rapid drop in intensity towards higher kinetic energies. At 8.9 eV, the intensity of the secondary electrons has dropped to one tenth of the intensity at the maximum at 0.6 eV. Henke et al. have proposed fitting the kinetic energy distribution $\beta(E_{kin})$ of secondary electrons from insulators emitted after excitation by soft X-rays to a function with the following shape [65]:

$$\beta(E_{Kin}) = k\frac{E_{Kin}}{(E_{Kin} + E_A)^3} \tag{4.1}$$

Where k is a constant and E_A is the electron affinity of the material defined as the energy difference between the bottom of the conduction band and the vacuum level [163]. In Figure 4.6, the measured secondary electron peak is indicated by a red line and the model of Henke et al. as the dashed blue line. Fitting Eq. 4.1 to the experimental data, yields an electron affinity of 1.1 ± 0.1 eV. This value is in reasonable agreement with values found by other workers for bulk SiO_2 (0.9 eV [164] - 1.3 eV [163]). Of the photoemission from SiO_2 in Fig. 4.2, 92% of the total intensity is contained in the kinetic energy range 0-20 eV which is attributed to secondary electron emission. This shows an important advantage of the nanoparticle beam technique. If the secondary electron emission of deposited nanoparticles is measured, the charge build-up on the nanoparticle surface would prevent the slow secondary electrons from

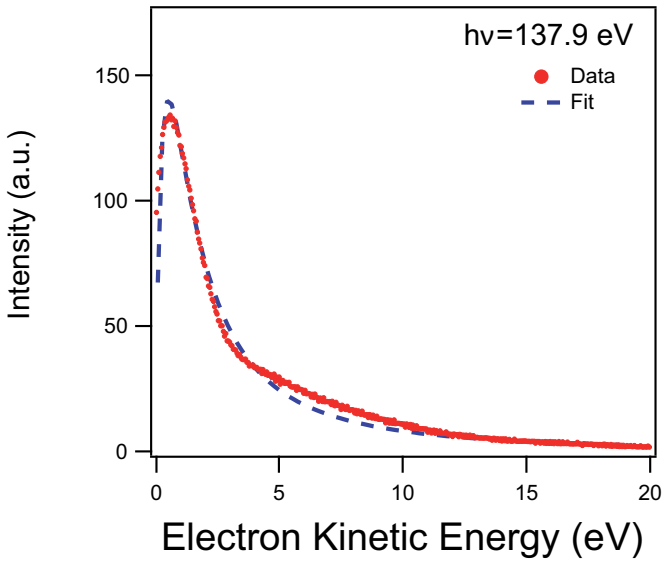

Figure 4.6: The low kinetic energy part of the electron emission spectrum from SiO_2 nanoparticles (d=50 nm) at a photon energy of 137.9 eV. The peak of low energy electrons is attributed to secondary electrons. The blue dashed line is a fit to equation (4.1).

leaving the nanoparticle [150]. With the nanoparticle beam technique, this is prevented by continuously supplying fresh sample to the ionization region.

4.4 Particle Size Dependence

For SiO_2 nanoparticles that have a size that is of the order of magnitude of the escape depth of the nanoparticles, one might expect that if one, for example, excites the Si 2p electrons that the ratio of unscattered photoelectrons to secondary electrons would vary with the particle size. Indeed, a comparison of the photoelectron spectrum of the 8.2 nm SiO_2 nanoparticles shown in Figure 3 in ref. [23] with that of 50 nm nanoparticles (cf. Figure 4.2) reveals that the Si 2p signal relative to the secondary electron emission is stronger for the smaller nanoparticles. In the present work, the photoemission from nanoparticles of

different size are compared (50 nm, 60 nm, 90 nm, 150 nm, and 210 nm) and no size dependence is found. This is understandable, because the nanoparticles are in all cases much larger than the photoelectron escape depth.

Another method to probe size dependence in the interaction between nanoparticles and soft X-rays would be to measure the angular distribution of electron emission relative to the propagation direction of the X-rays. Wilson et al. [165] have reported size-dependent angular asymmetry in the emission of photoelectrons from NaCl nanoparticles after excitation with vacuum-ultraviolet radiation at a photon energy of 9.4-12 eV. Extending this idea to soft X-rays would make it possible to not only probe the electron emission behavior as a function of nanoparticle size but also by varying the penetration depth of the X-rays (by varying the photon energy) and the escape depth of the photoelectrons (see figure 4.3). It is anticipated that higher photon energies would in this case lead to a more symmetric photoemission since the penetration depth of the radiation increases. Likewise, higher kinetic energies of the photoelectrons increase their inelastic mean free path which is also anticipated to lead to a more symmetric photoemission (cf. Fig. 4.3).

4.5 Electron-Electron Coincidence Spectroscopy

Electron-electron coincidence spectroscopy, where two electrons originating from the same photoabsorption process are detected, has been used successfully to study atomic gases [166, 167], molecules [131, 168, 169], small clusters [170–172], and solids [173–176]. Here, the method will be extended to the study of photoionization of free nanoparticles.

In order to study multi-electron emission from nanoparticles, cases where one or more electrons are detected after exactly one electron bunch passing the

beamline leading to exactly one light flash are sorted, according to the number of electrons detected. In Figure 4.7 (a) the electrons detected over approximately one hour have been sorted according to the number of electrons detected after one flash of soft X-rays interacting with the nanoparticle beam. Up to 5 electrons can be detected after the interaction of one flash of soft X-rays with the nanoparticle beam. Detection of exactly one electron is the most probable event and detection of more than one electron gets increasingly less probable with the increasing number of electrons detected. In Fig. 4.7 (b)-(f) the kinetic energies of the electrons for each case in Fig. 4.7 (a) is shown, corresponding to the kinetic energies of electrons detected when exactly one (b) (74% of the detected electrons), exactly two (c) (22%), exactly three (d) (3.8%), exactly four (e) (0.4%), and exactly five (f) (0.03%) electrons are detected. In all these cases, the contribution from slow secondary electrons is dominant.

When two unrelated events are detected during the same acquisition time window one speaks of false coincidences. The true coincidences are events where absorption of one photon leads to the emission of two or more electrons. False coincidences, on the other hand, are two unrelated events that by chance happen during the same acquisition time period, and where each event originates from the emission of a single electron. Examples of such events may be found from the ionization of one carrier gas molecule and of a nanoparticle, ionization of two different nanoparticles by the same X-ray pulse and the case where one nanoparticle absorbs X-rays photons at two different sites of the nanoparticle. The probability of two unrelated events taking place has a quadratic dependence on the magnitude of the primary event, whereas a single process has a linear relationship. In this way, one distinguishes false coincidences from true ones. This can be accomplished by doubling the photon flux, which will result in the quadrupling of false coincidences whereas the true coincidences are only

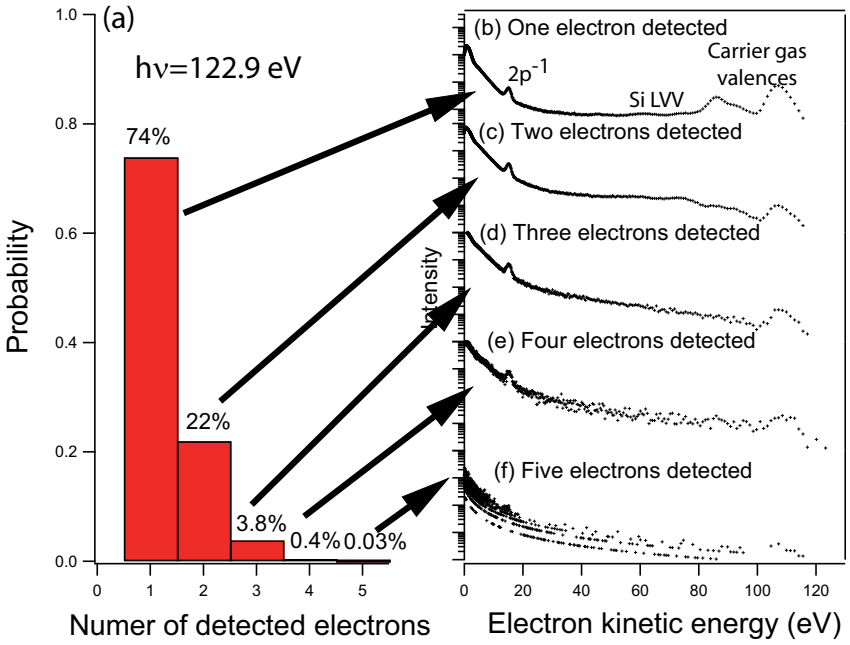

Figure 4.7: All detection events sorted according to the number of electrons detected. Note that due to the dead time after detection of one pulse, not all electrons that get emitted will actually get detected.

doubled. Since the current in the storage ring decreases between injections, the photon flux dependence of the ratio of single emission events to double emission events can easily be monitored during the experiments.

False coincidences are not *per se* a problem in coincidence spectroscopy. In Fig. 4.7(c)-(f) representing two, three, four, and five electron detection events, there is a signal at ≈ 100-115 eV of photoelectrons from the carrier gas. By chance these are emitted during the same X-ray flash as one, two, or three electrons emitted from nanoparticles. Coincidences that are known to be false, such as those where the sum energy of the electrons is above the double ionization threshold, are acceptable since they are simply discarded for the analysis of the results.

Bresch [104] (p. 94) estimated the amount of photons that would hit a d=150

nm nanoparticle in a nanoparticle beam to be six if the photon flux is $5 \cdot 10^{13}$ photons per 100 mA of ring current. Assuming a typical ring current in single bunch mode of 10 mA, this yields $5 \cdot 10^{12}$ photons per second. In the experiments discussed here, the exit slit of the beamline is used to reduce the photon flux so this value will be somewhat of an overestimate relative to the maximum photon flux of the beamline. If, for simplicity, it is assumed that the nanoparticles are cubes of side length 50 nm, the transmission through the nanoparticle will be 60% assuming a penetration depth of 100 nm (Figure 4.3). Thus, one tenth of the flux as compared to the estimate of Bresch, one tenth of the area, and an absorption of 40% leads to the estimate that one particle will on average absorb $6 \cdot 0.1 \cdot 0.1 \cdot 0.4 = 0.024$ photons. This estimate is reasonable, since it is in accordance with the estimate that, on average, about one nanoparticle is in the ionization region at any given time while the count rate is typically 10000-20000 at a repetition rate of 1.25 MHz, which means that 1-2 out of a hundred pulses will ionize a nanoparticle.

Figure 4.8 shows the case where exactly two electrons are detected for d=50 nm SiO_2 at a photon energy of 122.9 eV. The kinetic energies of the two electrons involved in each event are deduced from their flight times and plotted against each other. Fig. 4.8 thus corresponds to spectrum (c) in Fig. 4.7 but with kinetic energy of each of the electrons in a pair plotted against each other. Each point represents a unique combination of kinetic energies of the two electrons. Such a plot is called a coincidence map. From the coincidence map, different channels that contribute to two-electron-emission can be distinguished. However, not all two electron emission events can be detected by such experiments. Due to the dead time of the detector, two electrons that have similar flight times will not be detected as a pair but merely as one electron. The dead time of the detector in the experiments discussed here is 50-100 ns.

Without the dead time, detection of pairs of equal kinetic energies would be possible. They would show up as a diagonal line in a coincidence map.

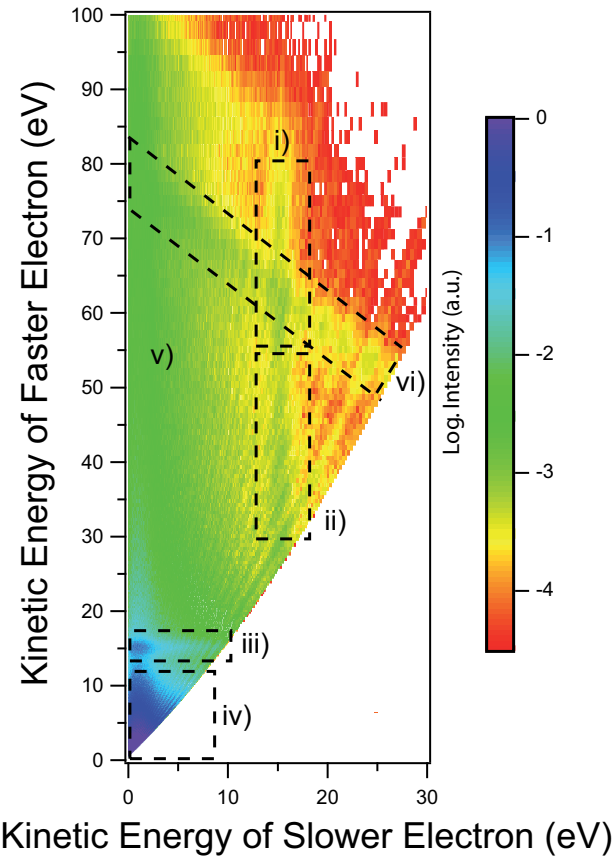

Figure 4.8: Coincidence map recorded at $h\nu = 122.9\ eV$ showing the energy distribution of electron pairs for those cases where exactly two electrons are detected. The dashed boxes correspond to different electron emission channels that can be distinguished. See text for assignment of the different channels. The signal is shown on a logarithmic scale for clarity.

The following two electron emission channels, which are marked by dashed boxes in figure 4.8 are identified.

- (i) At a photon energy of 122.9 eV the Si 2p electrons will have a kinetic energy of about 15 eV if they are emitted without losing energy

on their way to the surface. Likewise, the Si LVV lines lie in the kinetic energy range 55-80 eV [158]. Channel (i) is thus the result of the Si 2p photoelectron and the Auger electron associated with the subsequent decay both leaving the nanoparticle without energy loss. In this case, the photoelectron is the slower one at this photon energy and the Auger electron is the faster one. If the kinetic energy of the faster electron is below 55 eV, it is assigned to a scattered Auger electron.

- (ii) This channel, where the slower electron has a kinetic energy of 15 eV and the faster electrons have a kinetic energy lower than the unscattered Si LVV in (i) is assigned to the emission channel when Si 2p are emitted without losing energy on their way to the surface of the nanoparticle whereas the Auger electron does undergo inelastic scattering. In Fig 4.9 channels (i) and (ii) can be seen more clearly.

- (iii) The emission of one electron with $E_{kin} = 15eV$ and one slow electron ($E_{kin} < 10eV$). This is attributed to the emission of Si 2p in addition to exactly one secondary electron which must have been created by the Auger electron as it traveled through the nanoparticle. The channel where the Auger electron causes two secondary electrons will not turn up in this coincidence map since it leads to the emission of three electron in total.

- (iv) The emission of two secondary electrons. This two-electron-emission channel can have many reasons. It can be caused by absorption by an electron in the valence band which will have $\approx$ 90-110 eV kinetic energy and can therefore cause the emission of two secondary electrons. It can be the result of an Auger electron causing two secondary electrons, or it can be caused by an Si 2p and the subsequent Auger electron each

causing one secondary electron. It is not possible to distinguish these mechanisms.

- (v) A continuum that can have many causes [177]. It could come from absorption by electrons in the valence bands [178] that lose energy during the transport through the nanoparticles and causes one or several secondary electrons on the way. Alternatively, it can be caused by Si 2p absorption where the Si LVV electrons have slowed down and yield one secondary electron while the Si 2p electrons are thermalized in the bulk. A third possibility is Si 2p absorption where both the Si LVV and Si 2p electrons are slowed down. These different possible mechanisms cannot be distinguished.

- (vi) The diagonal line is due to double ionization of the carrier gas (N_2) and not due to the nanoparticles.

Electron-electron coincidence spectroscopy where an inner-shell photoelectron is measured in coincidence with an Auger electron has been used to separate spectral features that in a normal Auger spectrum are not distinguishable. An example of this is a study in which Auger lines from Cu from different processes could be clearly distinguished from each other when measuring the Auger lines in coincidence with the L_2 or L_3 photoelectrons, respectively [179]. In Figure 4.9 a coincidence map is shown where a potential of +30 eV is applied to the magnet. The photon energy is 137.9 eV. At this photon energy, the kinetic energy of unscattered Si 2p electrons is 29.9 eV and thus they are better distinguishable from the strong secondary electron peak. Applying a positive voltage to the magnet prevents the slowest electrons from entering the flight tube and increases the resolution for faster electrons. Moreover, at constant dead time of the detector, it changes the range of kinetic energies that can be

reached. In Fig. 4.9, for instance, pairs of electrons with kinetic energies of 35 eV and 30 eV are detected, whereas in Figure 4.8 pairs of electrons with those kinetic energies are not in the range that can be detected. The notable feature observed in Figure 4.9 is the coincidences between the unscattered Si 2p with unscattered and scattered Si LVV Auger electrons. Fig. 4.9 (b) shows a cut through 4.9 (a) where the energy of the slower electron corresponds to the energy of the unscattered Si 2p electrons (shown as the dashed box in Fig. 4.9(a)). The kinetic energy distribution of the faster electron can be compared to Auger electron spectra from bulk SiO_2 reported by Ramaker et al. [158] The features at 60-80 eV are the Si LVV bands of SiO_2. It consists of two broad features centered at 62 eV and 75 eV, respectively. The position of the two bands from the SiO_2 nanoparticles is not significantly different from what was observed in bulk SiO_2. The case where the Si 2p and the Si LVV electrons leave the nanoparticles unscattered is a very selective probe for the nanoparticle surface [67, 180, 181]. This is because two electrons must leave the particle without inelastic scattering. An effective mean free path, λ_{Eff} for both electrons reaching the surface of the nanoparticles without scattering and leaving it can be calculated if one assumes that the propagation of the photoelectron and the Auger electron are independent of each other [182,183]:

$$\frac{1}{\lambda_{Eff}} = \frac{1}{\lambda_{Auger}} + \frac{1}{\lambda_{Photoelectron}} \tag{4.2}$$

Where λ_{Auger} and $\lambda_{Photoelectron}$ is the inelastic mean free path of the Auger electron and photoelectron, respectively. Assuming the inelastic mean free paths in Fig. 4.3, $\lambda_{Auger} \approx \lambda_{Photoelectron} \approx 0.8\ nm$, the effective mean free path for both electrons to leave the nanoparticle is 0.4 nm. This length is shorter than 3 Si-O bonds [184]. This means that the surface sensitivity of the experiment

can be extended even further by detecting the Si 2p and the subsequent Auger electron in coincidence.

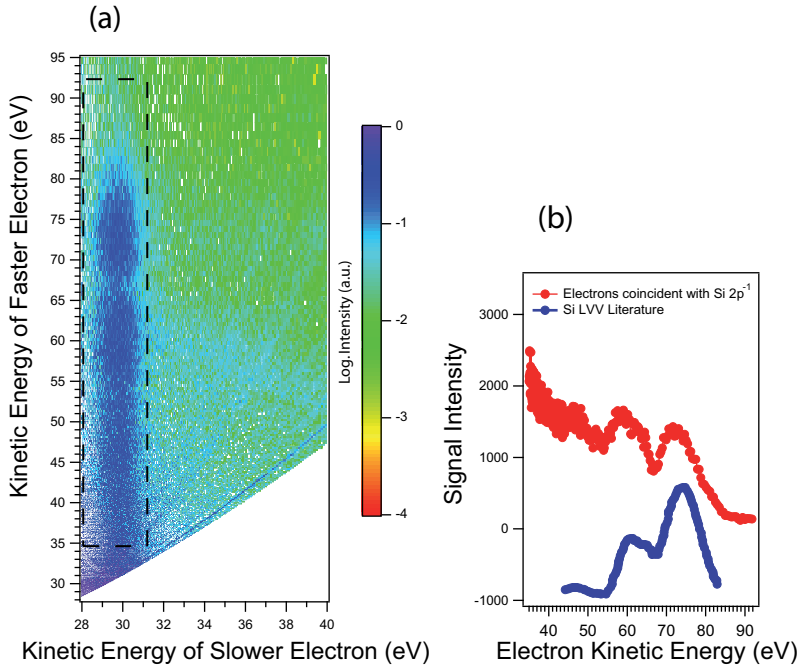

Figure 4.9: (a): Coincidence map recorded at $h\nu = 137.9eV$ showing the energy distribution of electron pairs for those cases where exactly two electrons are detected. (b): Cut through the map (indicated with the dashed box) for the case that the slower electron has $\approx$ 30 eV kinetic energy which corresponds to the unscattered Si 2p electrons. This is compared to the Si LVV Auger spectrum of SiO_2 reported by Ramaker et al. [158]. For the spectrum in Ref. [158], the inelastic portion of the signal has been substracted.

In Fig. 4.10, photoemission from SiO_2 nanoparticles with a diameter of 50 nm is shown after excitation at a photon energy of 73.1 eV. The photon energy is chosen to be below the Si 2p absorption edge, resulting in absorption only by the electrons in the valence band of SiO_2. In Figure 4.10, a false color coincidence map of those events where exactly two electrons are detected is shown. As in Figures 4.8 and 4.9, the most intense two-electron emission channel is the emission of two slow electrons ($E_{kin} < 10$ eV) which is attributed to the

emission of secondary electrons. A smaller contribution of faster pairs of elec-

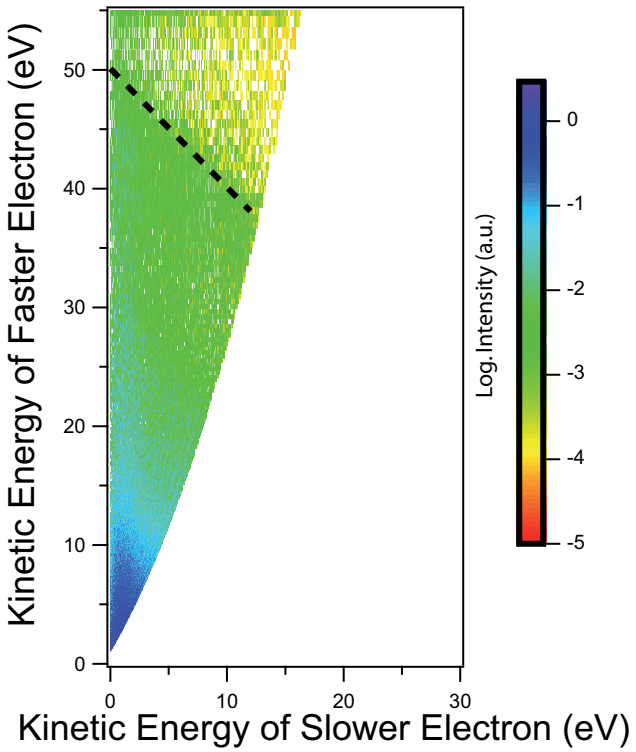

Figure 4.10: An electron coincidence map for the case that exactly two electrons are detected after the excitation of SiO_2 nanoparticles with 73.1 eV synchrotron radiation. This photon energy is below the Si 2p absorption edge and only valence electrons can be excited. The diagonal dashed line shows electron pairs emitted with a sum kinetic energy corresponding to a binding energy of 23 eV which is twice the binding energy of the maximum of the valence band (cf. Fig. 4.5).

trons stretches up to a diagonal line of constant sum energy of the emitted electron pair. Above this line there is an abrupt decrease to the signal. The electron pairs on this line are two electrons being emitted from the top of the valence band of SiO_2. The sum energy of the emission from the top of the valence band is close to being twice the ionization threshold for single ionization of an electron at the top of the valence band. No two-electron emission pairs

can be detected above this line because of conservation of energy. This double ionization threshold of two times the single ionization threshold is typical for solids whereas it is higher for atoms and molecules. The reason for this is the electron correlation energy [168]. The sum energy corresponding to two times the binding energy of the maximum emission from the nonbonding O_{2p} character (E_{sum} 11.5 eV + 11.5 eV = 23 eV) has been indicated with a dashed line in Fig. 4.10.

In principle, two mechanisms are conceivable for two-electron emission from the valence band. The first one is the case where a single electron absorbs the photon and then collides with other atoms which it ionizes, creating an electron pair. The second mechanism is direct double photoionization [175, 176, 185]. These two mechanisms cannot be distinguished by the electron-electron coincidence experiments. However, it is noted that the dynamics of emission for the two different processes will be different. The electron scattering mechanism will involve a time-lag due to the time needed by the electron to travel to the atom where the second ionization takes place. This time-lag is of the order of 10 fs [185]. That is well below the time resolution of the present experiment (60 ps). However, recent advances in attosecond physics [186–188] have shown that this time resolution can be reached.

The total count rate for two-electron emission is around 7000 counts per second. Of these, electrons in two electrons events with a sum energy of 37-52 eV, i.e. those attributed to direct double ionization from the valence band, are detected at a rate of 45 counts per second. The ratio of two-electron event detected to one-electron events is 1:5. This ratio can be compared to typical one-electron:two-electron rates in helium. In the photon energy range corresponding to 30-400 eV above the double ionization threshold of helium, the cross section is roughly two orders of magnitude lower than the cross section

for single ionization [59]. This much higher ratio in the nanoparticle is mainly caused by the high probability of the emission of two secondary electrons, since they contribute to the majority of two-electron emission events.

4.6 Conclusions and Outlook

The photoemission from SiO_2 nanoparticles after excitation with extreme ultraviolet radiation and soft X-rays has been reported and discussed. The photoelectron spectra show emission of valence electrons, Si 2p and O 1s inner shell electrons, and Auger electrons, as well as slow secondary electrons. By recording electron-electron coincidence event, channels involving the emission of exactly two electrons after absorption of exactly one photon are observed. The strongest two-electron-emission channel is the emission of two secondary electrons. Other two-electron-emission channels that could be unambiguously distinguished are: (i) an inner shell electron (Si 2p) and an Auger electron, (ii) an Si 2p electron and an Auger electron that has undergone inelastic scattering, (iii) an Si 2p and a secondary electron, (iv) the emission of two secondary electrons, and (iv) the emission of two valence electrons. The electron-electron coincidence method offers a site selective method of studying the electronic structure of nanoparticles, since unscattered photoelectrons originate from sites close to the surface while electrons that have undergone inelastic scattering will come preferentially from the bulk.

If the dead time of the detector could be reduced, a quantitative picture of the secondary electron yield could be obtained [166]. For instance if multi electron emission event are measured in coincidence with a core shell electron, the secondary electron emission would give a quantitative picture of the secondary electrons caused by the Auger electron.

Applying the method discussed here to nanoparticles of different materials would be straightforward. For example, it has been reported that the charging behavior of gold coated SiO_2 nanoparticles is significantly different from that of non-coated SiO_2 nanoparticles when exposed to soft X-rays [189]. The kinetic energy resolution in the experiment discussed here could yield more insight into the nature of these differences in charging behavior.

Chapter 5

Elastic X-ray Scattering from Free SiO_2 Nanoparticles

Elastic scattering of electromagnetic radiation from particulate matter depends on both the properties of the radiation (wavelength and polarization) and those of the object from which they are scattered (shape, size, chemical composition). For the special case of a plane wave scattered from a spherical object an analytical solution to Maxwell's equations exists that was introduced by Mie [87] who was motivated by the different colors of colloidal gold solutions. In this Chapter, elastic scattering of soft X-rays from spherical SiO_2 nanoparticles is used as a probe of their size distribution and optical properties.

Considering that the size is of crucial importance for the optical properties of nanoparticles, the determination of the size distribution is a problem of fundamental importance. Various methods are used for this purpose on nanoparticles in different environments. Examples include dynamic light scattering [190] for suspensions, transmission electron microscopy for deposited particles [191, 192], as well as differential mobility analysis for aerosols [193]. In this Chapter, elastic scattering of soft X-rays will be used to determine the

size distribution of free SiO_2 nanoparticles in a nanoparticle beam. Elastic X-ray scattering has been used extensively to study the size and growth of nanoparticles in suspensions [194–199]. In the gas phase, different regions of the electromagnetic spectrum have been used, including hard X-rays [200–204] as well as ultraviolet [205] and vacuum-ultraviolet radiation [29, 206–210]. Of special interest in the present work is a study on elastic scattering of soft X-rays from free SiO_2 nanoparticles [28]. In that study, the scattered X-rays were detected in a wide range of scattering angles (4-100°) with an angular resolution of 1.15°. In the present work, however, the focus is put on the small angle scattering range, because in that range the fine structure of minima and maxima are resolvable for soft X-ray scattering from nanoparticles with a narrow size distribution. Notably, in the soft X-ray region, materials may be studied in an element specific manner allowing chemical differentiation [211, 212].

A key parameter in the elastic scattering from particulate matter is the ratio of the wavelength of the radiation and the size of the object. This is described by the Mie size parameter x:

$$x = \frac{2\pi r}{\lambda} \tag{5.1}$$

Here, λ is the wavelength of the radiation and r is the radius of the spherical object. In the present work the wavelength of the radiation is much smaller than the size of the object to be studied. Therefore, the angular distribution of the scattering is strongly influenced forward scattering, as is typical for high Mie size parameters.

In Fig. 5.1 this is illustrated for the case of scattering from d=5, d=50, and d=500 nm SiO_2 nanoparticles at 78.9 eV. The simulations are performed with the Mieplot program [213]. This corresponds to Mie size parameters of 1, 10, and 100, respectively. The refractive index used for the simulations is

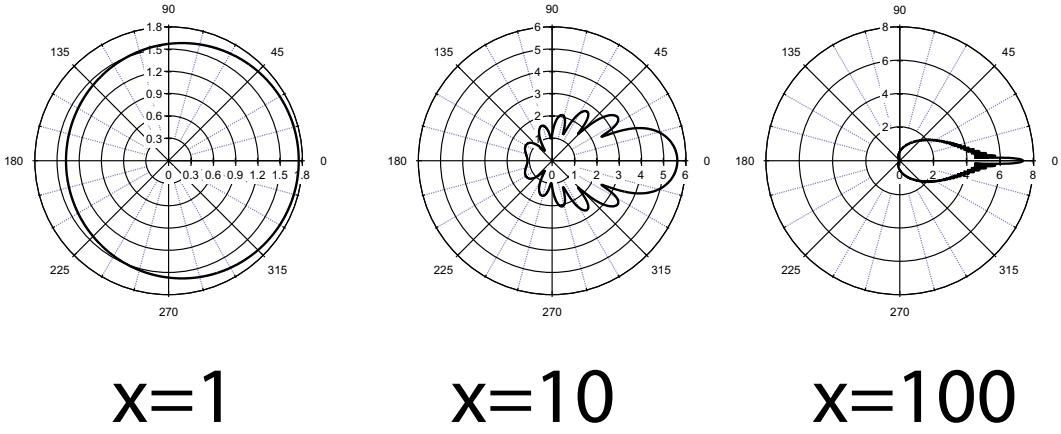

Figure 5.1: Polar diagram of simulations of the angle resolved light scattering from spheres for three Mie size parameters $x = (2\pi r)/\lambda$. This corresponds to d=5 nm, d=50, and d=500 nm particles at 78.9 eV. The strongly forward oriented and structured Mie scattering appears when the diameter of the sphere is larger than the wavelength of the radiation. In this polar plot, the direction of propagation of the light is 0° and the radial axis is logarithmic. See text for details of the simulation.

$n = 0.9675 + 0.01616i$ which corresponds to SiO_2 nanoparticles with a density of 2.2 g/cm^3 at 78.9 eV. As the Mie size parameter increases, forward scattering becomes dominant and shows a distinct structure of maxima and minima. In the work presented here the Mie parameter is in the range 30-270. It is noted that this range is similar to the Mie size parameter regime when studying particles that are some tens of micrometers in size using visible light [24, 25].

5.1 Angle Resolved Soft X-Ray Scattering from Free Nanoparticles

Figure 5.2 shows experimental angle resolved small angle elastic X-ray scattering spectra of free nanoparticles of different sizes on a logarithmic scale. The scattering patterns are recorded at a photon energy of 450 eV. This photon

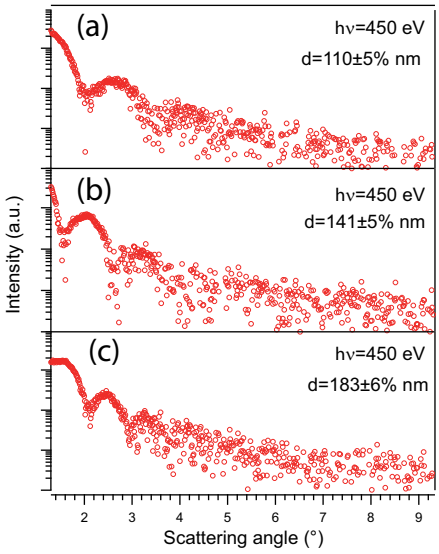

Figure 5.2: Angle resolved scattering spectrum recorded at a photon energy of 450 eV for SiO_2 nanoparticles of three different sizes. The intense forward scattering as well as the characteristic minima and maxima are clearly visible. The intensity of scattered X-rays is shown on a logarithmic scale.

energy corresponds to a wavelength of 2.76 nm. The sizes of the three nanoparticle samples are (a) 110 nm ± 5%, (b) 141 nm ± 5% and (c) 183 nm ± 6%, respectively. Thus, the Mie size parameter ranges between 125 and 208 and is in all cases >> 1. In all three scattering spectra, the intensity of the scattered X-rays decreases by two to three orders of magnitude over the range 1.5-5° as is typical for Mie scattering. A strong forward orientation of soft X-ray scattered from free SiO_2 nanoparticles has been reported before in the angle region 4-100° [28] and of vacuum ultraviolet radiation scattered from SiO_2 in the angle region 18-120° [29]. However, in those earlier studies, the characteristic minima and maxima are not well resolved. This is due to the fine structure smearing out in the wide angle range when scattering from nanoparticles of a finite size distribution is studied. In the present work, the maxima and minima can be

resolved in the small angle scattering range. Since the photon energy is kept constant in 5.2 (a)-(c), the shifting of the position of the minima are likely due to the different sizes of the SiO_2 nanoparticles. The plateau in the scattering intensity from d=183 nm ± 6% nanoparticles below 1.6° is due to saturation of the CCD camera (see Fig. 5.3 (c)). The characteristic minima and maxima will be used to determine the size distribution of SiO_2 nanoparticles and their refractive index in the Si 2p and O 1s regimes. Compared to earlier work, the use of an X-ray sensitive CCD camera in the present work has the advantage of a higher dynamic range and a higher angular resolution. Fig. 5.3 shows an overview over the angle resolved small angle soft X-ray scattering from d=183 nm ± 6% SiO_2 nanoparticles. The photon energy is varied between 100-600 eV in 5 eV steps and the scattered soft X-rays are recorded for each photon energy. Over this wide photon energy range, minima and maxima in the angle resolved scattering can be seen. These shift towards smaller angles as the photon energy is increased. This is due to the change in Mie size parameter and wavelength dependent changes in the refractive index. The location of the Si 2p and O 1s inner shell absorption edges have been marked by arrows. An arrow at ≈ 285 eV marks a sudden drop in the scattering intensity that is due to reduced photon flux. This is caused by a drop in the photon flux as a results of carbon contaminations on the reflection optics in the beam line.

The positions of the characteristic minima and maxima in the angle resolved elastic scattering is determined by (i) the Mie size parameter and (ii) the material's refractive index. If the Mie size parameter is known, the refractive index can be derived and vice versa. In the following, the size distribution of the SiO_2 nanoparticles will first be determined. Then, this size distribution will be used to derive the refractive index in the Si 2p and O 1s near edge regimes. Henke et al. calculated atomic scattering factors for a range of elements in a

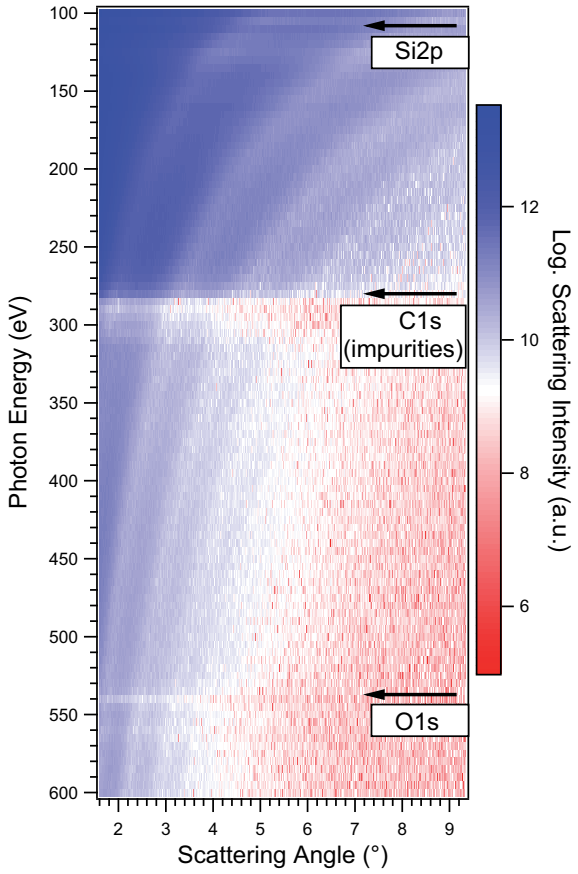

Figure 5.3: False color map of angle resolved elastic X-ray scattering from SiO_2 nanoparticles with a diameter of 183 nm ± 6%. The shift of the minima towards smaller angles as the photon energy is increased is a consequence of the increasing Mie size parameter and of the change in the refractive index of the material. The Si 2p, O 1s, and C 1s inner shell absorption edges have been marked by arrows. See text for details.

wide photon energy range from absorption measurements using the Kramers-Kronig relations [148]. The refractive index of materials in the soft X-ray regime may be accurately calculated in regions where there are no inner-shell absorption edges by using the data from Henke et al. [214]. The refractive index may deviate from the values reported by Henke et al. in the near edge regimes [148]. This is because the refractive index near inner shell absorption

edges is dependent on the chemical environment of the excited atom and cannot be treated as a weighted average of the constituent elements. The method to calculate the refractive index from the atomic scattering factors, as reported by Henke et al., depends critically on the density of the material. Henke et al. give for the complex refractive index [148]:

$$n = 1 - \delta - i\beta = 1 - \frac{r_0}{2\pi}\lambda^2 \sum_q n_q f_q(0) \tag{5.2}$$

where r_0 is the classical electron radius, λ is the wavelength of the X-rays, f_q are the complex atomic scattering factor for atom q and n_q is the number of atoms of type q per unit volume. From Eq. 5.2 one sees that the refractive index is proportional to the density of the material. The density of the SiO_2 nanoparticle samples has to be known in order to convert the tabulated atomic scattering factors into the refractive index. Various workers have reported the density of SiO_2 nanoparticles prepared by the Stöber synthesis [57, 162, 215–218]. Their density is lower than that of α-quartz which has been reported to be 2.65 g/cm^3 [219, 220] and amorphous bulk SiO_2 which is 2.2 g/cm^3 [218]. The density of SiO_2 nanoparticles prepared by the Stöber approach has been reported to be 1.98-2.03 g/cm^3 [162]. The lower density of SiO_2 nanoparticles prepared by the Stöber method as compared to amorphous bulk SiO_2 is due to the porosity of the nanoparticles [162]. The porosity of the SiO_2 nanoparticles results from the synthesis, which makes use of the hydrolysis and condensation of tetraethoxysilane in the presence of ammonia:

$$Si(OCH_2CH_3) + 4H_2O \rightarrow Si(OH)_4 + 4C_2H_5OH \tag{5.3}$$

$$SiOH_4 \rightarrow SiO_2 \downarrow + 2H_2O \tag{5.4}$$

In the synthesis, however, not all ethoxy groups leave the tetraethoxysilane which causes termination of the Si-O-Si chains. In Fig. 5.4 the relative abundance of Si atoms with two, three, or four O-Si bonds is shown, as measured by van Blaaderen and Kentgens [162]. About 66% of the Si atoms have four siloxane bonds, 30% have three and about 4% have only two. This incom-

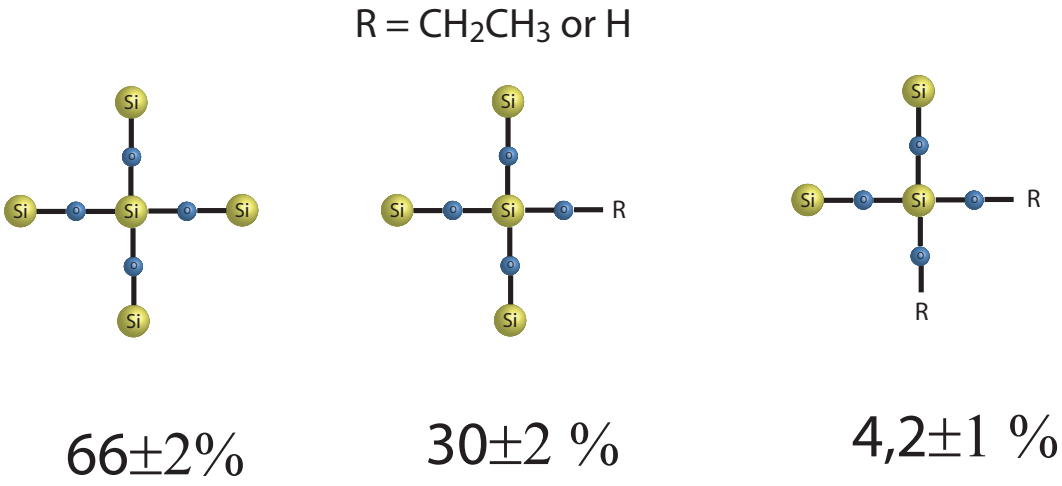

Figure 5.4: Si atoms that are not bound to four O-Si groups cause the Si-O-Si network to terminate. This explains the porosity of SiO_2 nanoparticles. The fraction of Si atoms with four, three, and two O-Si groups is also indicated [162].

pleteness in the Si-O-Si network causes the porosity of the SiO_2 nanoparticles, which reduces their density significantly as compared to SiO_2 with a complete Si-O-Si network. Another consequence of the incompleteness of the Si-O-Si network is the presence of carbon in the nanoparticles. Van Blaaderen and Kentgens determined the carbon content of SiO_2 nanoparticles prepared by the Stöber synthesis to be of the order of a few percent by weight [162]. However, the low photon flux at photon energies near the C 1s absorption edge due to carbon containing impurities on the beamline optics made attempts to study the elastic scattering in this photon energy regime unsuccessful.

5.1.1 Size Distribution

The experimental angular resolved scattering patterns are used to derive the size distribution and complex refractive index of the SiO_2 nanoparticles by fitting to them the following function:

$$f_{Simulated} = Af_{Mie}(x, n) + B \tag{5.5}$$

Here $f_{Mie}(x, n)$ is the scattering pattern as calculated by the Mie formalism using Bohren and Huffman's code [89] that depends on the Mie size parameter x and the material's complex refractive index n, B is a term that accounts for the background level in the experiment, and A is a prefactor that influences the overall intensity and is needed to bring the relative units of the simulation in agreement with the units of the experiment (scattered light intensity detected by the CCD camera) and A is thus influenced by the quantum yield of the detector, the photon energy dependent number of electrons generated in the detector per photon, and the photon flux. In general, photon energy dependent changes in the refractive index not only influence the position of the minima, but also the total intensity of the scattering. Cases will be shown where changes in the refractive index and changes in the prefactor A can have a similar influence on the shape of the scattering patterns. The term B that corresponds to a background of photons reaching the detector includes fluorescence photons, but their contribution is insignificant since the fluorescence is expected to be isotropic. Unlike the fluorescence, the scattered soft X-rays are preferentially oriented in the forward direction. Furthermore, the fluorescence yield is small (of the order of 10^{-4} [157]). Additionally, the background term B includes scattered soft X-rays that have been reflected from other parts of the experimental setup.

Fig. 5.5 shows simulated scattering patterns for 141 nm monodisperse nanoparticles at a photon energy of 375 eV for three different values of the density of the SiO_2 nanoparticles. The refractive indices corresponding to the three densities are calculated using Eq. 5.2 and are listed in Table 5.1. For better comparison, the simulations are run without considering the particle size distribution, i.e. the nanoparticles are assumed to be monodisperse for these simulations. Fig. 5.5 shows that the different refractive indices at this photon energy do not change the position of the minima significantly. The three values that are used in the simulations are 2.0 g/cm^3, which is the density reported for SiO_2 nanoparticles [162], 2.2 g/cm^3, which is the density of bulk amorphous SiO_2 given in Ref. [218], and 1.8 g/cm^3 which is added for a better comparison. With increasing density, the real part of the refractive index decreases whereas the imaginary part increases. The simulations indicate that SiO_2 of higher density give rise to a stronger scattering of the soft X-rays but that the position of the minima is not significantly shifted.

Although the values of the density used for the simulations in Fig. 5.5 are about 10% apart from each other, it can be seen in Table 5.1 that the change in density results in changes of the refractive index that are relatively small, i. e. 0.00033 for the real part and 0.00003 in the imaginary part. The simulations indicate that this change is too small to have a significant influence on the position of the minima.

These simulations therefore indicate that it is favorable to determine the size distribution of free SiO_2 nanoparticles at photon energies where variations of the refractive index does not greatly influence the position of the minima. As can be seen in Fig. 5.5, this condition is fulfilled at 375 eV, since variations in the refractive index caused by different density of the material will not change the result of the size determination by small angle X-ray scattering.

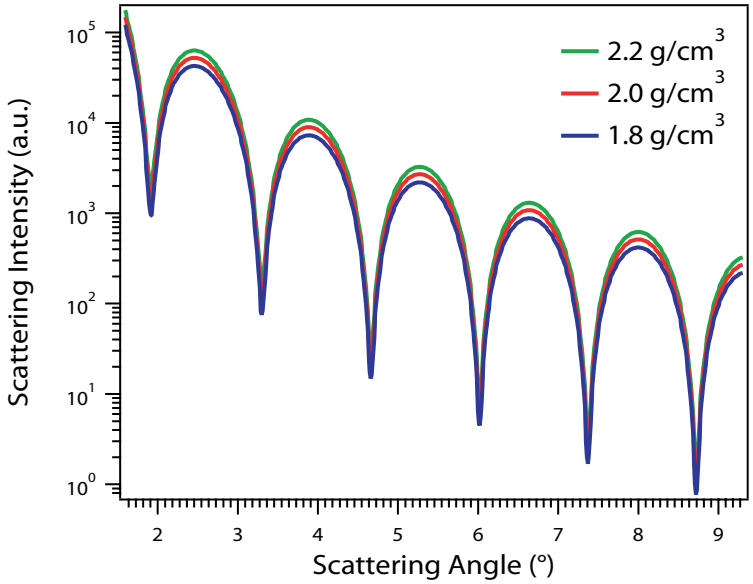

Figure 5.5: Simulations of scattering patterns from monodisperse d=141 nm SiO_2 nanoparticles at 375 eV when assuming different density. The different densities result in slightly different refractive indices that change the intensity of the scattering patterns. Notably, the different refractive index does not significantly change the position of the minima at this photon energy. The refractive indices used are listed in Table 5.1.

Fig. 5.6 shows elastic soft X-ray scattering curves from d=141 nm ± 5% SiO_2 nanoparticles at a photon energy of 375 eV along with simulations using the Mie formalism. The refractive index is calculated from the atomic scattering factors using the density of SiO_2 nanoparticles of 2.0 g/cm^3 [162]. For the simulation, some refractive index must be assumed. Since the refractive index scales with the density, assuming a refractive index requires the assumption of the particle density. The result of this approach of particle size determination is not influenced by this, since realistic values of the refractive index do not influence the position of the minima (Fig. 5.5). Fig. 5.6 illustrates the influence of (i) the diameter of the nanoparticles and (ii) their size distribution, corresponding to their polydispersity, on the elastic soft X-ray scattering pat-

Table 5.1: Complex refractive indices of SiO_2 nanoparticles used for the simulations in Fig. 5.5 that result from assuming different densities of the nanoparticles.

Density	$Re(n)$	$Im(n)$
1.8 g/cm^3	0.99851	0.0002763
2.0 g/cm^3	0.99835	0.0003070
2.2 g/cm^3	0.99818	0.0003376

terns. The polydispersity is defined as the relative standard deviation of the diameter. Fig. 5.6 (a) shows the influence of the ensemble polydispersity on the simulated scattering curves for monodisperse nanoparticles, 2%, 5%, and 8% polydispersity, respectively. The depth of the minima critically depends on the polydispersity of the nanoparticles since the experimental curves are a superposition of signal from nanoparticles of different sizes. Experiments on single particles, where averaging over an ensemble of particles is avoided, could overcome this limitation [208–210], but goes beyond the scope of this work. When the polydispersity is 8%, the depths of the minima are smaller than the depths in the experimental curve, whereas the depths of the minima is too large when the polydispersity is assumed to be 2%. Assuming a polydispersity of (5 ± 1)% gives the best agreement with the experimental results. Using transmission electron microscopy, a polydispersity of 4.3(4)% is obtained. The analysis is inconclusive regarding the shape of the size distribution. Possible size distributions could be normal or log-normal distributions. Fig. 5.6 (b) shows simulations where the polydispersity is kept constant at 5% and the particle diameter is varied. When assuming different diameters, the position of the minima shifts. For a diameter of 136 nm the minima occur at larger angles than in the experimental results. Assuming a size of 146 nm leads to minima occuring at smaller angles than in the experimental curve. Finally, a

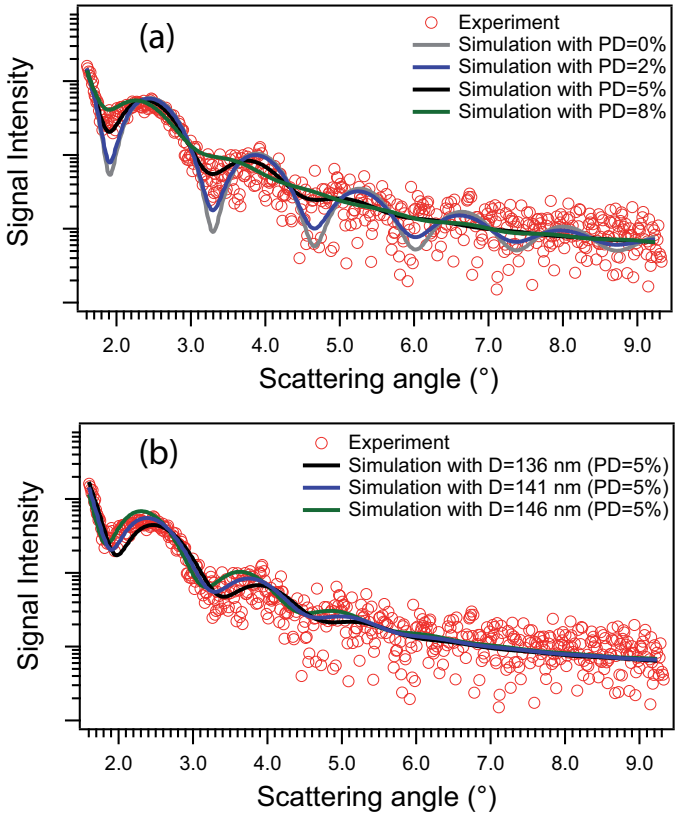

Figure 5.6: Angle resolved scattering curves from SiO_2 nanoparticles (diameter: 141 nm ± 6%) at $h\nu = 375\ eV$. (a) Simulated curves when assuming a polydispersity of 2 %, 5 %, and 8 % are shown. The experimental curve is an average of scattering curves from nanoparticles of sizes that correspond to the size distribution of the sample. (b) Same experimental data as in (a) but with simulations using different particle central diameters of 136 nm, 141 nm, and 146 nm, respectively.

diameter of 141 ± 2 nm is found to give the best agreement with the experimental results.

It has been pointed out before that the fine structure of minima and maxima in the angular distribution of soft X-rays scattered from nanoparticles is more sensitive to changes in nanoparticle size or refractive index at larger scattering

angles [206]. While this is certainly true for monodisperse particles, the analysis of angle resolved scattering curves from nanoparticles with a finite size distribution has severe limitations. This is due to the measured signal being a superposition of signal from nanoparticles of different sizes. In fact, since the scattering pattern is more sensitive to the particle size at larger scattering angles, the pattern will also be more smeared out at large angles than at small angles. Fig. 5.7 (a) shows simulations of the soft X-ray scattering pattern from monodisperse 141 nm and 146 nm SiO_2 nanoparticles, respectively. The refractive index is derived from Eq. 5.2 using a density of 2.0 g/cm^3. The scattering pattern is simulated for the angle region 0-35° which is a larger regime than is covered in the experimental work. The distance between the minima in the scattering pattern from nanoparticles of different sizes are indeed larger in the 15-35° regime as compared to the 0-10° regime. For instance, the tenth minimum is found at 14.16° and 13.67° for d=141 nm and d=146 nm particles, respectively. This corresponds to a shift of 0.49°. However, the position of the first minimum is found at 1.92° and 1.85° for the d=141 nm and d=146 nm, respectively. Thís corresponds to a shift of 0.07°. Thus, the simulations indicate that for a monodisperse sample, the shift of the tenth minimum is seven times larger than the shift of the first minimum. Fig. 5.7 (b) shows the effect of polydispersity on the simulated scattering curves. When using a realistic polydispersity of 5% the minima in the 10-35° region get washed out due to the superposition of scattering signal from different sizes, whereas in the regime below 10°, the minima can still be observed. For the example discussed above where the shift of the tenth minimum and the first minimum were compared, the simulations indicate that the tenth minimum will be very poorly resolved for a sample with 5% polydispersity. This illustrates the advantage of measuring the scattering patterns in the small angle region when working

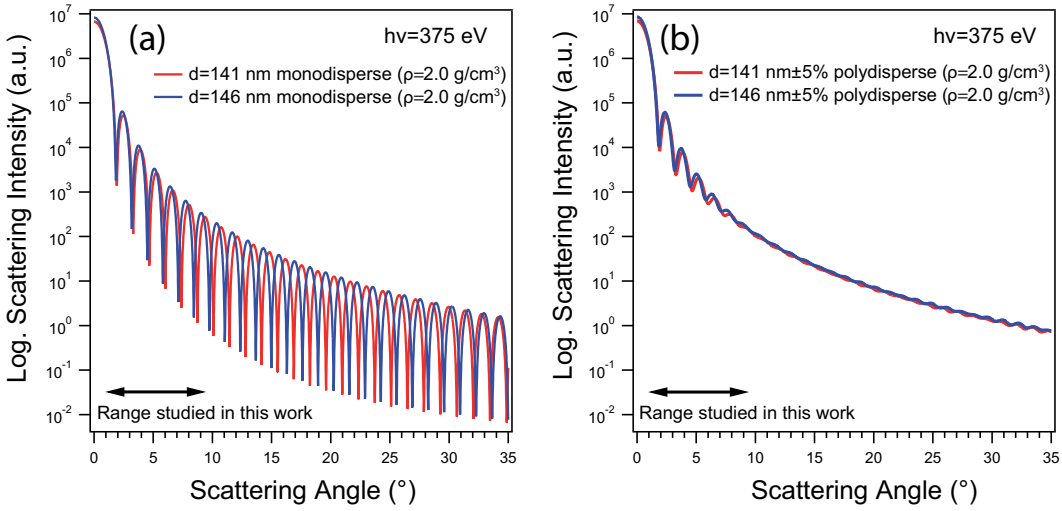

Figure 5.7: (a) Simulated scattering curves for soft X-rays scattered from (i) monodisperse d=141 and (ii) monodisperse d=146 nm SiO_2 nanoparticles. (b) The same simulations when assuming a polydispersity of 5%.

with polydisperse samples. As a result, this makes small angle scattering an interesting approach for determining particle sizes and size distributions.

The analysis of the scattering data is done with a fitting method that is based on the Bohren-Huffman algorithm [89]. For testing the fitting algorithm, the results are compared to simulations done by the Mieplot program [213]. The comparison shows that the implementation of the Bohren-Huffman code used in this work yields identical simulations in all tested cases. Figure 5.8 shows size distributions obtained from three different SiO_2 nanoparticle samples of different sizes. In Fig. 5.8 (a), the angle resolved scattering patterns recorded at 375 eV are shown along with a fitting done using the Mie formalism to determine the central diameter and polydispersity. The simulations are a result of letting the fitting procedure find the best agreement for central diameter and polydispersity while keeping the refractive index fixed (at the values obtained from Eq. 5.2) using a density of 2.0 g/cm^3. Using another value for the

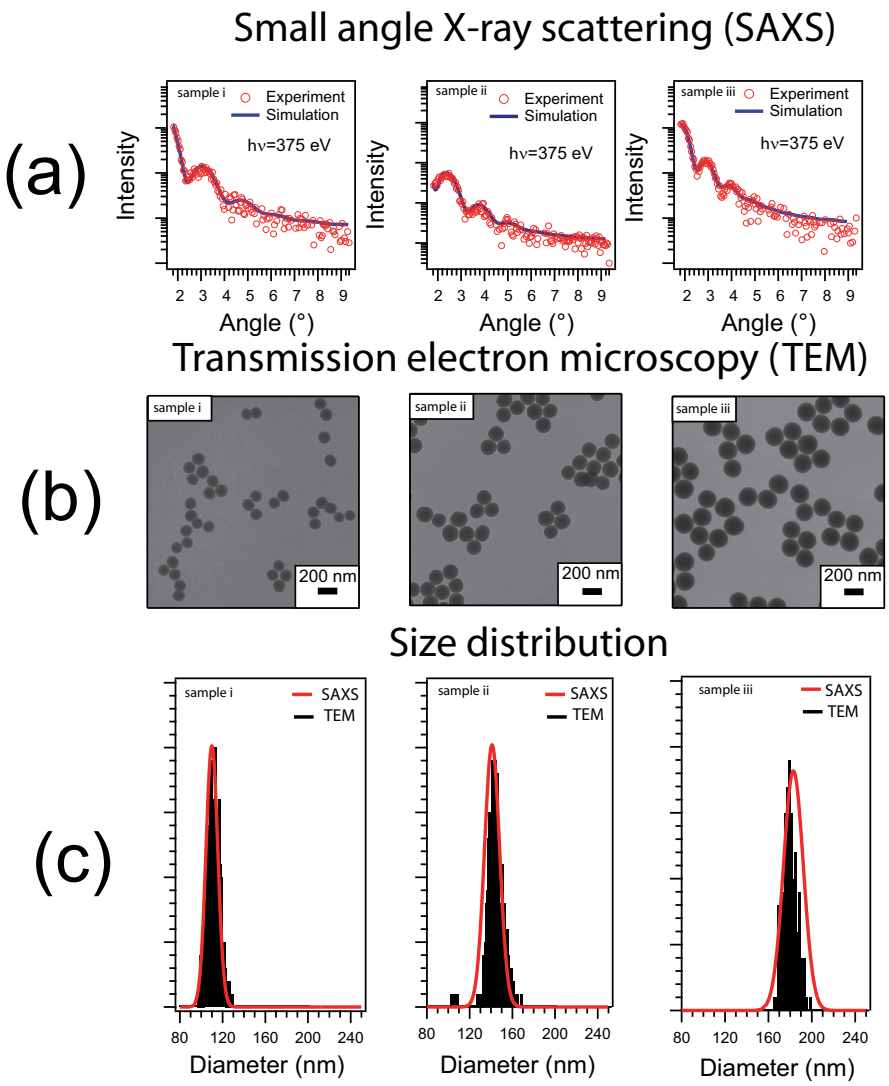

Figure 5.8: Determination of the size distribution of three SiO_2 samples (labeled (i), (ii), and (iii)) of different sizes. (a): Angle resolved scattering patterns from different sizes recorded at 375 eV. From these curves the size distributions (red curves in (c)) can be obtained using the Mie formalism. (b): Transmission electron micrographs of the three SiO_2 samples. (c) A comparison of the size distributions obtained from the two methods: Black bars are size distributions obtained from electron microscopy and the reds line ones obtained with angle resolved soft X-ray scattering. The results for the central diameters and polydispersity are summarized in Table 5.2.

density will not change the results, since the position of the minima is not significantly influenced by changes in the density at this photon energy (cf. Fig. 5.5). The size distributions determined in this way are shown in Fig. 5.8 (c) as red curves for each of the three samples. For a comparison, the three samples are also studied by transmission electron microscopy (Fig. 5.8 (b)). Not all particles that are analyzed are shown in the Fig. 5.8 (b). The distribution of the diameters derived from transmission electron microscopy are shown as black bars in Fig. 5.8 (c). The size distribution of the nanoparticles derived from transmission electron microscopy follow a normal distribution around the central diameter. A normal distribution is therefore also assumed for the fitting procedure, but the outcome is not affected if a log-normal distribution is used. It has been reported that nanoparticles often have a log-normal size distributions [221,222]. The central diameters and polydispersity derived from both methods are summarized in Table 5.2. For sample (i) in Fig. 5.8 the

Table 5.2: Central diameters (d) and polydispersity (PD) of different sizes of SiO_2 nanoparticles as determined from transmission electron microscopy (TEM) and small angle X-ray scattering (SAXS).

Sample	$d(SAXS)$	$d(TEM)$	$PD(SAXS)$	$PD(TEM)$
i	110(2)	110	5(1)%	5.8(6)%
ii	141(2)	142	5(1)%	4.3(4)%
iii	183(2)	178	6(1)%	3.4(3)%

central diameter is identical for both methods. For sample (ii), the diameter obtained from elastic soft X-ray scattering is by 1 nm smaller, and for sample (iii) the diameter obtained from elastic soft X-ray scattering is approximately 5 nm larger. This 5 nm difference corresponds to a relative deviation of $\approx 3\%$. Numerous studies have compared size distributions of SiO_2 nanoparticles that are determined by X-ray elastic scattering in suspensions to size distributions

determined by transmission electron microscopy [191, 223, 224]. Generally, diameters determined by transmission electron spectroscopy tend to be smaller than those determined by elastic X-ray scattering in suspensions. The smaller values for sizes obtained from transmission electron microscopy compared to those from elastic X-ray scattering are due to a slight shrinking of the particles in the high vacuum used for electron microscopy. The present results on free nanoparticles prepared in a nanoparticle beam which is injected into high vacuum indicate that the particles are already largely dried when they reach the scattering region. The nanoparticles in the largest sample studied is by $\approx 3\%$ larger in the scattering region than in the electron microscope. For the two smaller samples this is not the case. Therefore, it can be concluded that larger nanoparticles have not been completely dried.

After spraying the nanoparticle dispersion into ambient pressure, the droplets are dried by a diffusion drier (see Chapter 3). After drying, the nanoparticles enter the aerodynamic lens within a few seconds. In the experimental chamber used in this work, the background pressure during the experiments is typically 10^{-7} mbar and the nanoparticles are subjected to this pressure for a short time, namely the flight time between the differential pumping stage and the interaction region with the X-rays. If a velocity of 200 m/s is assumed for the nanoparticle beam, they will spend about 0.5 ms in the high vacuum before interacting with the soft X-rays. It has been argued that heating of the nanoparticles by the electron beam of the electron microscope is crucial in causing the shrinking [162]. The present results indicate that the sizes of the 110 nm $\pm$ 5% and 141 nm $\pm$ 5% SiO_2 nanoparticles obtained from small angle soft X-ray scattering in high vacuum and with transmission electron microscopy are quite similar to each other. However, the size distribution obtained from soft X-ray scattering for 183 nm $\pm$ 6% nanoparticles is about 3%

larger than determined with transmission electron microscopy. This indicates that heating by the electron beam is not crucial for shrinking the particles and may indicate that the shrinking already takes place if the nanoparticles are kept at room temperature.

Note that all diameters reported in this work are geometric diameters. When comparing size distributions determined by different sizing techniques, care must be taken to not confuse the geometric diameter with other size measures such as the hydrodynamic diameter obtained from dynamic light scattering [193, 225]. The hydrodynamic diameter contains the particle as well as the solvation shell around the particle, and is therefore expected to be larger than the geometric diameter of the nanoparticles.

In this setup multiple scattering, where X-rays scattered from one nanoparticles continue on to scatter from another one [226] can be neglected due to the low density of nanoparticles in the interaction region. Jones reported that multiple scattering from nanoparticles with a radius of 100 nm has to be considered when the particle density exceeds 10^{19} particles per m^3 [227]. In this experiment, the density is estimated to be well below that limit, i.e. $\approx 10^6\ /cm^3$ or $\approx 10^{15}\ /m^3$.

The size distribution of SiO_2 nanoparticles has now been determined *in situ*, which is of importance if the size distribution in the scattering region differs from the size distribution that can be derived with transmission electron microscopy. Due to shrinking of porous nanoparticles as they are dried in vacuum, the size distribution in the scattering region is not necessarily the same as the one derived by transmission electron microscopy. Since the soft X-ray scattering patterns depend on both the size distribution and the refractive index, it is of importance to have accurate information on the size distribution in the scattering region to be able to accurately determine deviations in the

refractive index near inner shell absorption edges as will be shown in Sections 5.3.1 and 5.3.2.

5.2 Analysis of the Scattering Patterns

Sorensen and Fischbach [228] have proposed to plot angle resolved scattering data from spheres against the product of the radius of the sphere R and the scattering vector $q = 4\pi\ sin(\theta)/\lambda$ where 2θ is the scattering angle and λ is the wavelength of the radiation. When plotted in this way, distinct power laws can be observed that depend on the phase shift parameter $\rho = \frac{4\pi R}{\lambda} \mid n-1 \mid$, where λ is the wavelength, R is the radius of the particle, and n is the refractive index. This parameter is the phase shift of a wave that travels through the center of the particle, as compared to a wave traveling the same distance in vacuum [229]. Fig. 5.9 shows such a plot for d=183 nm $\pm$ 6% SiO_2 nanoparticles recorded at a photon energy of 245 eV on a log-log scale. Shown is also a dashed line with slope (qR^{-4}). The (qR^{-4}) line is in good agreement with the maxima of the experimental curve. This is indicative of scattering from the bulk and is known as Porod's law [230, 231]. In a sense, q is a yardstick of the measurement. This means that the inverse of the scattering vector q^{-1} corresponds to the length scale of the experiment. The scattering is sensitive to structures larger than q^{-1} but it is not sensitive to structures smaller than q^{-1} [230, 232, 233]. In the present case, as Fig. 5.9 shows, the q regime corresponds to probing the global properties of the nanoparticles (size and shape) but applying this method to larger q-values probes local features, such as surface roughness. Indeed, in the study of Bresch et al. in the wide angle scattering region deviations from Mie scattering were observed for q-values above $\approx 0.5\ nm^{-1}$ which were assigned to scattering due to a rough and

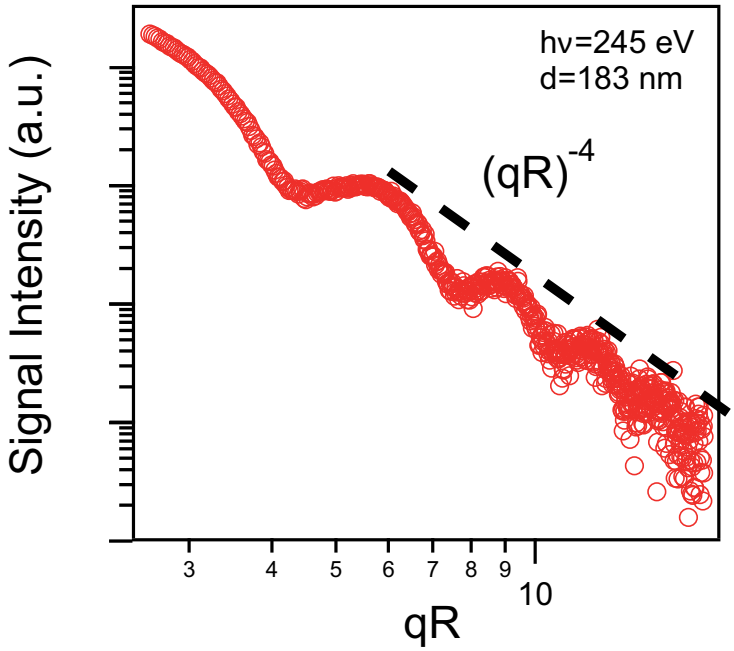

Figure 5.9: Angle resolved soft X-ray scattering from free d=183 nm ± 6% SiO_2 nanoparticles plotted against the dimensionless parameter (qR), where q is the scattering vector and R is the radius of the nanoparticles.

graded surface [28]. The inverse of this value of the scattering vector is 2 nm. Indeed, this is the size order of the surface roughness of SiO_2 nanoparticles. For the d=183 nm ± 6% SiO_2 nanoparticles shown in Fig. 5.9, a q-value of 0.5 nm^{-1} would correspond to (qR)=46 which is not contained in the experimental regime. This shows that for this particle size and photon energy, the soft X-ray scattering patterns in the small angle range correspond to probing the global properties of the particles; size, shape, and refractive index. For larger scattering angles (and thereby larger qR), smaller features can be probed, such as surface roughness.

5.3 Determination of the Refractive Index

There are many gaps in the refractive index of materials around the regions of characteristic absorption edges of inner-shell electrons in the soft X-ray regime [214]. Near the absorption edges the refractive index will be strongly influenced by the local environment of the excited atom and cannot be treated as a weighted average of the atomic scattering factors of the constituent elements of the material under study. For the case of SiO_2 the most comprehensive study of the refractive index in the soft X-ray region was done by Filatova et al. [214]. They applied Kramers-Kronig analysis to reflection spectra of amorphous SiO_2 in the photon energy range 60-3000 eV. Specifically, the Si 2p, O 1s, and Si 1s absorption edges are contained in this region.

Other studies on more limited photon energy ranges include the study of Woronick et al. [234] near the O 1s absorption edge. For the Si 2p absorption edge, the works of Klinkenberg and Illinsky [235], Tripathi et al. [236] and Blau et al. [237] are worth mentioning but they are all limited to a few chosen photon energies and they do not yield comprehensive information on the refractive index changes near inner shell absorption edges. In the following, the angle resolved elastic soft X-ray scattering from the SiO_2 nanoparticles recorded for a large number of photon energies near the absorption edges is used to determined the refractive index at these photon energies at high energy resolution. The Si 2p (IE=108.0 eV) and O 1s (IE=537.1 eV) absorption edges could be reached by the soft X-ray beamline. The Si 1s absorption edge of SiO_2 is found at 1848.6 eV [138] and is outside the range of photon energies that the beamline can deliver (UE52-SGM at BESSY II, see Chapter 3). For the determination of the refractive index, angle resolved scattering curves from d=183 nm $\pm$ 6% SiO_2 are analyzed. The photon energy is varied in the range 106-115 eV in steps of 0.1 eV for the Si 2p near edge regime and 530-550 eV in steps of 0.2

eV for the O 1s near edge regime. For each photon energy a scattering curve is recorded and the modified Bohren-Huffman fit routine is applied to find the real and imaginary parts of the refractive index while keeping the central diameter and polydispersity constant. The size distribution found at 375 eV is used (cf. Fig. 5.8).

5.3.1 Refractive Index Near the Si 2p Absorption Edge

There are two parameters that determine the experimental scattering pattern of soft X-rays scattered from free nanoparticles, namely the complex refractive index and the size distribution of the nanoparticles. At the photon energy that was used to determine the size distribution (375 eV) the position of the minima in the scattering pattern is not significantly influenced by changes in the refractive index (cf. Fig. 5.5). This allows a unambiguous determination of the refractive index without any assumptions about the density of the nanoparticles.

Near the Si 2p absorption edge, this is not the case since the size distribution and the refractive index are both strongly influencing the scattering pattern. Fig. 5.10 (a) shows a comparison of an experimental scattering pattern recorded at 109.3 eV using 183 nm ± 6% SiO_2 nanoparticles compared to fits using different size distributions for the nanoparticles. The simulations correspond to using a size distribution of 178 nm ± 6%, 181 nm ± 6%, 183 nm ± 6%, and 185 nm ± 6%, respectively. The Bohren-Huffman code is then used to determine the refractive index that gives the closest fit to the experimental data. The values for the refractive index obtained in this way when assuming different size distributions are listed in Table 5.3. The numbers in the brackets are standard deviations. The simulated scattering patterns have been multiplied by 1.5, 2.5, 4, and 7, respectively to shift them on the log-scale in order

to make a comparison easier. For the different size distributions, a suitable fit to the experimental data is found in all cases, but the obtained refractive indices are different. This shows that it is not possible to unambiguously determine the refractive index of SiO_2 nanoparticles in this range without prior knowledge of the size distribution.

Fig. 5.10 (b) shows the same experimental scattering pattern as in Fig. 5.10 (a) but includes simulations using the size distribution obtained at 375 eV (183 nm ± 6%) and the refractive index obtained from Fig. 5.10 (a) by assuming 178 nm ± 6% and 185 nm ± 6%, respectively (Table 5.3). This shows that both the size distribution and the refractive index have a significant effect on the scattering patterns at this photon energy, which means that the size distribution and the refractive index cannot be independently determined at 109.3 eV. For the determination of the refractive index in the Si 2p regime, the angle range 3.4-5.1° is used. The reason is that for this experiment, an electron detector is positioned near the scattering center that blocks the scattering pattern at higher and lower angles. This is, however, not a significant disadvantage for the analysis since the first minimum is clearly observed in the angle range 3.4-5.1 °. If no minima are observed, it is neither possible to unambiguously determine the refractive index nor the size distribution. Fig.

Table 5.3: Complex refractive indices found in Fig. 5.10 (a).

Size Distribution	$Re(n)$	$Im(n)$
178 nm ± 6%	0.9786(4)	0.0196(3)
181 nm ± 6%	0.9807(3)	0.0142(3)
183 nm ± 6%	0.9819(3)	0.0111(3)
185 nm ± 6%	0.9831(2)	0.00833(3)

5.11 shows the results of determining the refractive index of SiO_2 nanoparticles in the Si 2p regime. Since the size distribution and refractive index cannot be

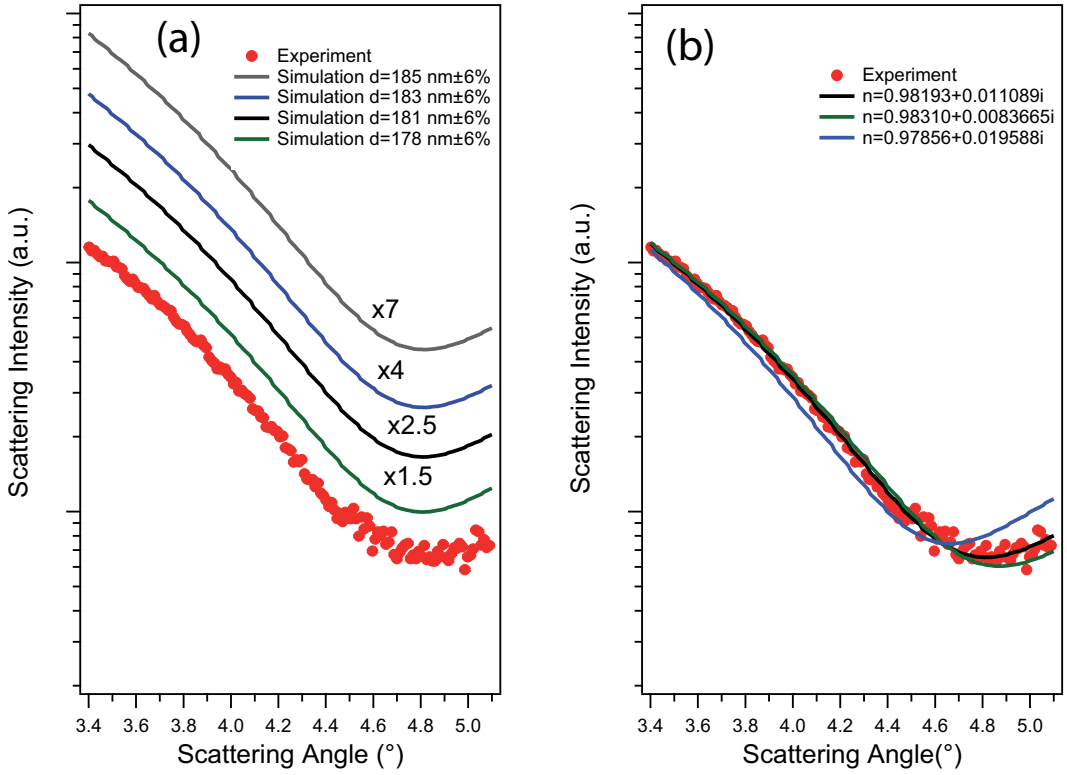

Figure 5.10: (a) Simulated scattering patterns from SiO_2 nanoparticles at a photon energy of 109.3 eV when assuming different size distributions. Scattering curves from SiO_2 nanoparticles can have similar shapes when varying both the size distribution and the refractive index. This exemplifies the need to separately determine the size distribution. The values for the refractive index are liste din Table 5.3 The simulated curves have been multiplied as is shown in the Figure for easier comparison. (b) shows simulations using a size distribution of 183 nm ± 6% and the refractive indices indicated in the figure.

determined independently in this photon energy range, results are shows when using different size distributions. The photon energy is varied in the range 106-115 eV in 0.1 eV steps and for each photon energy an analysis similar to the one in Fig. 5.10 (a) is performed. When using different size distributions, the values obtained from the analysis for the refractive index change. When using 181 nm ± 6%, 183 nm ± 6%, and 185 nm ± 6%, the real part of

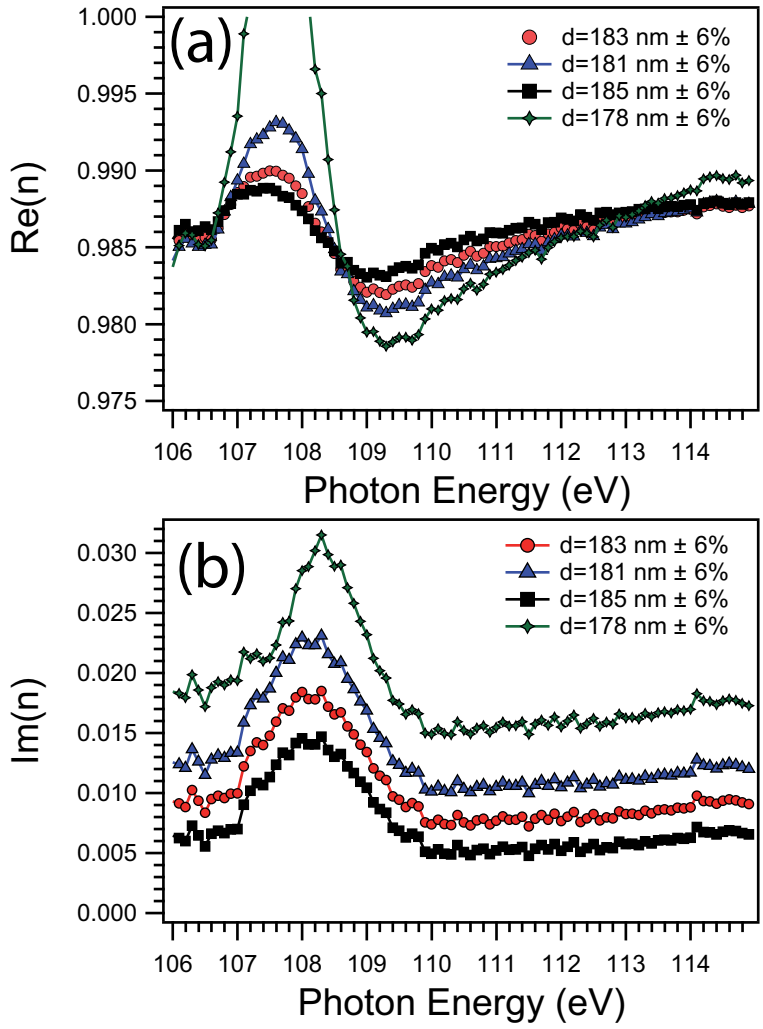

Figure 5.11: Real (a) and imaginary (b) parts of the refractive index in the Si 2p regime obtained from the scattering curves when using different size distributions. The size distributions that are used are the same as in Fig. 5.10.

the refractive index has a maximum in the range 107-108 eV and a minimum around 109 eV. When using 178 nm ± 6%, no realistic value for the real part of the refractive index could be derived in the photon energy range 107-108 eV. This is an indication that this value is too far away from the true size distribution. This is a significant finding, since the central diameter of 178 nm is

the size distribution obtained from transmission electron microscopy whereas the central diameter obtained with elastic soft X-ray scattering at 375 eV is 183 nm. This shows that the size distribution of the nanoparticles needs to be determined *in situ* in order to be able to reliably determine the refractive index in the Si 2p regime. Likewise, the simulations reveal distinct changes of the imaginary part of the refractive index (Fig. 5.11 (b)) when using different size distributions. For the size distributions used, the imaginary part of the refractive index is the highest by assuming 178 nm ± 6% and the lowest by assuming 185 nm ± 6%. However, the general shape of the curve is similar for all size distributions, showing a maximum at 108.3 eV, except when assuming 178 nm ± 6%, in which case this feature is narrower than for the other size distributions.

In Figure 5.12 the results of the determination of the real and imaginary parts of the refractive index of SiO_2 nanoparticles near the Si 2p absorption edge is shown when using d=183 nm ± 6% and is compared to the values reported by Filatova et al. for bulk amorphous SiO_2 [214]. The error bars are the statistical error. The real part of the refractive index is in general somewhat higher than the values published by Filatova et al., which is to be expected for the less dense nanomaterial. For instance, at 112.5 eV, the refractive index reported by Filatova et al. is 0.98452+0.01071i, whereas it is 0.9861(2)+0.0082(3)i in this work. A minimum is observed at 109.2 eV as well as a maximum at 107.7 eV. These features are both similar in the work of Filatova et al., but the amplitude is significantly different. The Si 2p binding energy relative to the vacuum level is 108.0 eV and is indicated by a flag in the Figure 5.12 (b) (Chapter. 4, [22, 23, 151]). The imaginary part of the refractive index shows a maximum at 108.3 eV. The position of the maximum of this feature is similar to that reported by Filatova et al. for bulk amorphous SiO_2. The positions

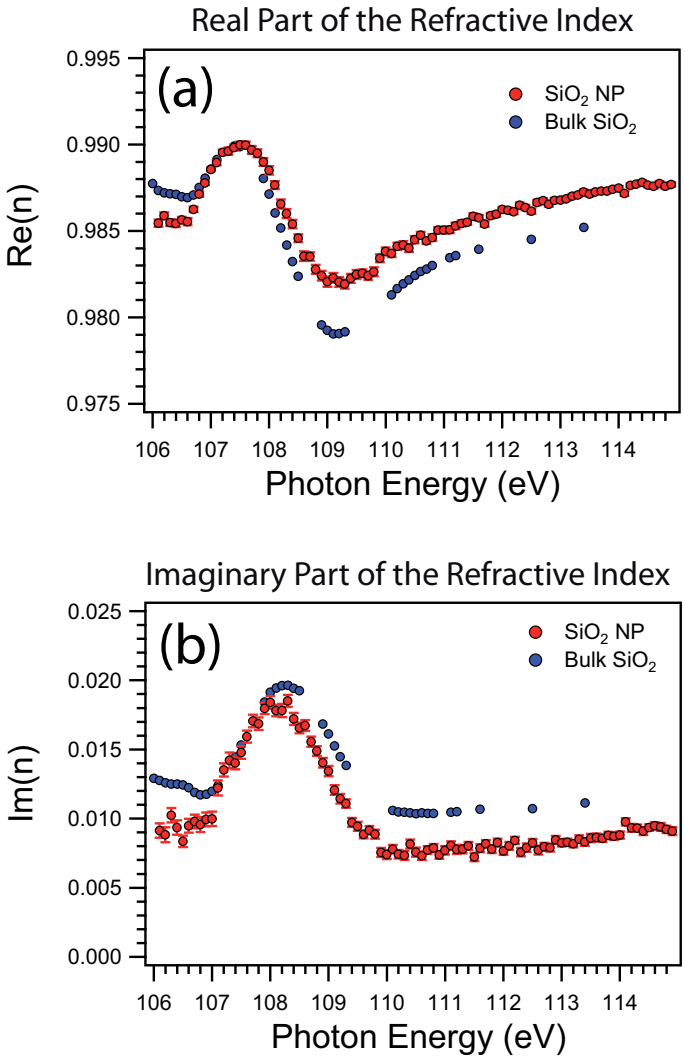

Figure 5.12: Refractive index of d=183 nm ± 6% SiO_2 nanoparticles near the Si 2p absorption edge (IE=108 eV) as determined by applying the Mie formalism to angle resolved X-ray scattering curves: (a) corresponds to the real part of the refractive index and (b) corresponds to the imaginary part. For a comparison, the results derived by Filatova et al. for bulk amorphous SiO_2 are indicated by blue circles [214].

of this maximum corresponds to the maximum seen in the total electron yield spectrum of SiO_2 nanoparticles in Figure 4.1 (a). This is expected, since the absorption is proportional to the imaginary part of the refractive index. The

imaginary part of the refractive index derived in this work is significantly lower than that reported in Ref. [214] in the photon energy range 106.0-107.5 eV. This is likely due to the lower density of the SiO_2 nanoparticles.

5.3.2 Refractive Index Near the O 1s Absorption Edge

The real and imaginary parts of the refractive index of SiO_2 nanoparticles near the O 1s inner shell absorption edge are shown in Figure 5.13. The real part has a maximum at about 536 eV. At the maximum of the real part the determination of the refractive index becomes less reliable due to lower scattering signal than at photon energies below the maximum. The lower signal can be attributed to the higher value of the real part of the refractive index (cf. Fig. 5.5). This is reflected by large error bars. This can be compared to the example in Fig. 5.5 where the intensity of scattering from SiO_2 nanoparticles with a higher real part of the refractive index is lower than for SiO_2 nanoparticles with a lower real part of the refractive index. The imaginary part of the refractive index can again be compared to the total electron yield data (Fig. 4.1 (b)). The imaginary part of the refractive index should show an overall structure similar to the total electron yield measurements. The determination of the imaginary part can only be said to qualitatively reveal an absorption edge. The values of the imaginary part of the refractive index can be seen to scatter around a higher value in the above-threshold regime 540-543 eV than in the regime 530-535 eV which is below the O 1s threshold.

Note the different scales in Figs. 5.12 and 5.13: The change of the refractive index in the Si 2p region is greater in absolute terms than in the O 1s regime. In the Si 2p regime, the real part varies in the range 0.9819(3)-0.9900(4) and the imaginary part in the range 0.0072(3)-0.0185(4). In contrast to this, the real part in the O 1s regime varies between 0.99872(5)-0.9995(1) (when disre-

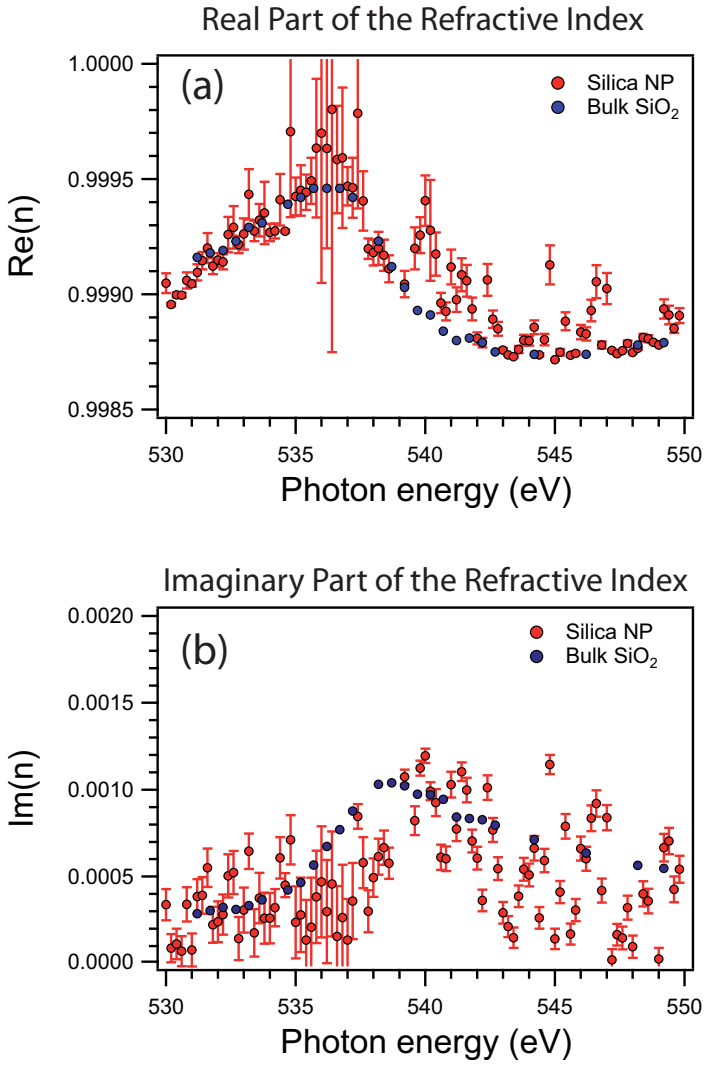

Figure 5.13: Refractive index of SiO_2 nanoparticles near the O 1s absorption edge (IE=537.1 eV), as determined by applying the Mie formalism to angle resolved soft X-ray scattering curves: (a) corresponds to the real part of the refractive index and (b) corresponds to the imaginary part. For a comparison, the results derived by Filatova et al. for bulk amorphous SiO_2 are indicated by blue circles [214].

garding obvious outliers around 537 eV) and the imaginary part in the range 0.0001(1)-0.0011952(5). This is in accordance with the observation in the X-ray regime that the real part of materials approaches unity and the imaginary

part approaches zero with increasing photon energy. These results show that analysis of small angle soft X-ray scattering patterns with the Mie formalism is a sensitive way to probe small changes in the refractive index of free nanoparticles near inner shell absorption edges. The scattering patterns clearly depend on both the size distribution and the refractive index. To determine the refractive index in a spectral region where it changes rapidly as a function of the photon energy, it is necessary to independently determine the size distribution of the nanoparticles. Otherwise, the effects of the size distribution and the refractive index on the scattering patterns cannot be unambiguously disentangled.

5.4 Conclusions and Outlook

Elastic scattering of soft X-rays from free SiO_2 nanoparticles is successfully recorded. The scattering patterns show the expected strong forward component and clear structures of minima and maxima, as is typical for Mie scattering. By analyzing these curves using the Mie formalism, three different sizes of nanoparticles are studied and compared to size distributions derived with transmission electron microscopy. The size distributions determined are in full agreement with size distributions determined with transmission electron microscopy for two out of the three samples. For the largest sample studied, however, the nanoparticles in the nanoparticle beam are 3% larger than determined by electron microscopy. It has been reported that SiO_2 nanoparticles prepared by the Stöber approach tend to shrink when put into high vacuum of an electron microscope due to evaporation of solvent in the pores of the nanoparticles. The present findings indicate that nanoparticles in the nanoparticle beam are already mostly dried when interacting with the soft X-

rays with the exception of the largest particle sample which is evidently not completely dried.

The refractive index of the nanoparticles in the regime of the Si 2p and O 1s absorption edges is determined from the angle resolved scattering patterns. The refractive indices are compared to results derived earlier by reflectometry on bulk amorphous SiO_2 [214]. Clear changes in both parts of the complex refractive index could be observed. The comparison showed that elastic scattering of X-rays is a sensitive tool to probe the optical constants of spherical nanoparticles in the core level regime. This method has the significant advantage over the Kramers-Kronig method that there is no need to scan over a wide photon energy regime to gain information about the complex refractive index of the material under study. With the nanoparticle beam technique, it will be possible to determine size distributions and refractive indices for free nanoparticles of different materials without any interaction with a surrounding medium.

Extending this setup to simultaneously measuring the small angle and wide angle scattering ranges would allow for probing of both global (size, shape, refractive index) properties of free nanoparticles, and local properties of the surface region without any influence from a surrounding medium.

Chapter 6

Excitation of Free SiO_2 Nanoparticles by Few-Cycle Laser Pulses

In this chapter results from experiment will be presented in which the electron emission from free SiO_2 nanoparticles is studied after excitation by ultra-short laser pulses of well defined, but variable waveform. In contrast to the experiments presented in Chapters 4 and 5, the photon energy of the exciting radiation is in the infrared regime, i.e. well below the ionization threshold of the nanoparticles and the interaction is characterized by the strong electric field. By controlled variation of the waveform - more precisely the carrier-envelope phase - the direction of electron emission can be controlled. Moreover, the kinetic energies of the emitted electrons are found to be higher than what is known for rare gas systems and this will be attributed to rescattering of the electrons at the surface of the nanoparticles in an effective electric field which is more intense than the laser field due to contributions from the polarization of the dielectric spherical nanoparticle and to a Coulomb field from free charges

on or near the nanoparticle surface.

Strong laser pulses of well-defined waveform have been used to study and control ionization and dissociation processes for a variety of systems, including atoms [30], molecules [31, 117] and solids [238]. The interaction of strong few-cycle laser pulses with nanostructured materials has also been studied previously for a variety of systems [85,239–244], but in this Chapter the first study using free nanoparticles in a nanoparticle beam will be discussed.

6.1 Electron Emission

Figure 6.1 shows typical momentum maps recorded after exciting (a) xenon atoms and (b) SiO_2 nanoparticles by ultra-short laser pulses at an intensity of $1.9 \cdot 10^{13}\ W/cm^2$. They correspond to a cut through the reconstructed three dimensional distribution in the plane defined by the propagation direction of the laser pulses and the electric field polarization axis [136] (cf. Chapter 3). The polarization axis is shown with a double headed arrow. The momentum scale in Fig. 6.1 is retrieved from velocity map images by determining the location of above-threshold ionization peaks in xenon along the polarization axis of the laser pulse and using the fact that the distance between them is given by the photon energy of 1.72 eV which corresponds to a central wavelength of 720 nm. The electron emission from xenon in Fig. 6.1 (a) shows both direct photoemission and electrons rescattered from the ionic core [245], which is characteristic of short pulse (strong field) ionization of xenon similar to what has been reported before [246]. Electrons emitted directly (without rescattering at the ionic core) have kinetic energies up to 2 U_p where U_P is the ponderomotive potential of an electron in the laser field. The 2 U_P limit is indicated in Fig. 6.1 (a) by a dashed circle.

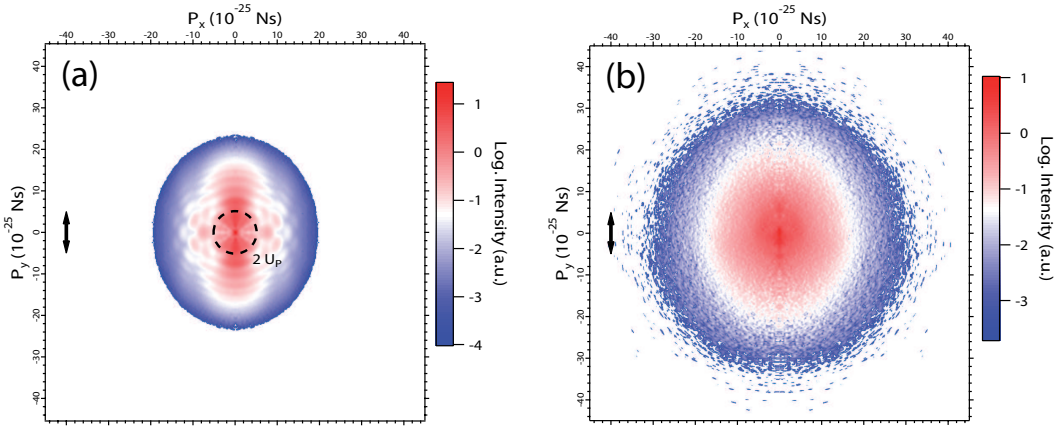

Figure 6.1: Momentum maps of electron emission from (a) xenon and (b) SiO_2 nanoparticles after excitation with $\approx$ 5 fs laser pulses with a peak intensity of 1.9 10^{13} W/cm^2. The emission from the SiO_2 nanoparticles can be seen to have a more continuous angular distribution and to extend to higher momentum. The size distribution of the nanoparticles is 109 nm $\pm$ 6%.

For higher electron kinetic energies, the electrons are mainly emitted along the polarization axis of the laser beam. The fastest electrons are the ones that propagate into the vacuum, are brought to a standstill and turn around towards the ionic core where they are scattered by an angle of 180° back away from the ionic core. This rescattering is the cause for strong-field physics phenomena such as high-harmonic generation [79], nonsequential multiple ionization [80], and above-threshold ionization [247]. These phenomena are dependent on the interaction of the returning electron with the ionic core. Chapter 2 deals with the rescattering process in more detail. For lower kinetic energies, numerous different trajectories contribute to the electron signal [85, 248].

In Fig. 6.1 (b), SiO_2 nanoparticles are excited using the same laser parameters as in Fig. 6.1 (a). A comparison of the electron emission from the nanoparticles and xenon shows a more continuous distribution for the emission from the nanoparticles both with respect to the angle of emission and kinetic ener-

gies. For xenon the emission is stronger along the polarization axis of the laser pulses, whereas it is more isotropic for the SiO_2 nanoparticles. Likewise, the kinetic energy distribution is more continuous and does not show the above-threshold ionization features as from the xenon atoms as is visible in Fig. 6.1 (a). In addition, the electrons emitted from SiO_2 nanoparticles extend up to higher kinetic energies than those from xenon. The nature of these differences is discussed in this chapter [249].

6.2 Carrier-Envelope Phase Dependent Electron Emission

For laser pulses that last only for a few oscillations of the electric field in length, the amplitude of the pulse envelope changes almost as fast as the electric field oscillates. In this experiment, the pulse duration is ≈ 5 fs, which corresponds to ≈ 2 oscillations of the electric field at a wavelength of 720 nm. The relation between the maximum of the pulse envelope and the maximum of the electric field is described by the carrier-envelope phase (or absolute phase) [250]. Fig. 6.2 shows the electric field of a few-cycle pulse, which is given by $E(t) = E_0(t)cos(\omega t + \phi_{CEP})$, where ϕ_{CEP} is the carrier-envelope phase, ω is the carrier angular frequency and E_0 is the peak amplitude. In Fig. 6.2 (a) the maximum of the envelope coincides with the maximum of the electric field corresponding to $\phi_{CEP} = 0$, whereas in Fig. 6.2 (b) the maximum of the envelope is at a zero-crossing of the electric field which corresponds to $\phi_{CEP} = \pi/2$. In Fig. 6.2 (c) the carrier-envelope phase takes a value of π and therefore the field maximum coincides again with the envelope maximum, where the electric field in (c) is pointing into the opposite direction relative to Fig. 6.2 (a). By varying the carrier-envelope phase, the electron emission

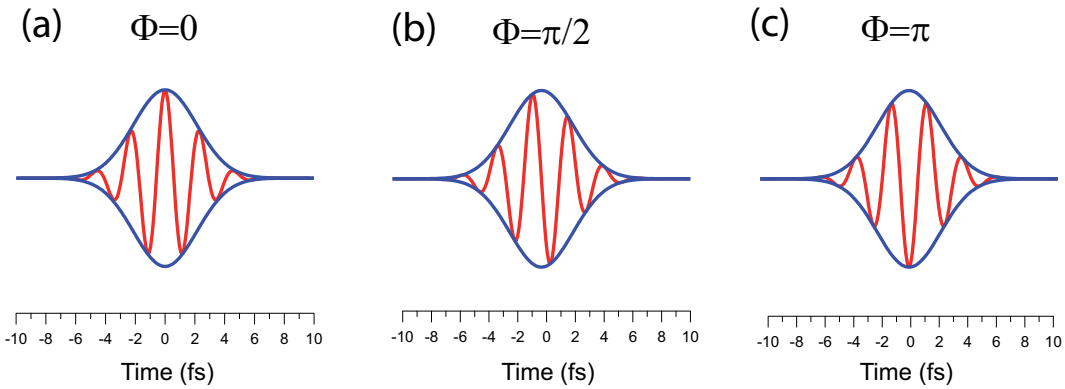

Figure 6.2: Electric field of few-cycle laser pulses with a 5 fs pulse length (FWHM). The phase difference between the maximum of the envelope (blue line) and maximum of the electric field (red line) is called the carrier-envelope phase. A pulse is shown for three different values of the carrier-envelope phase. In both (a) ($\phi_{CEP} = 0$) and (c) ($\phi_{CEP} = \pi$), the maximum of the field oscillations and the envelope coincide, but with the field pointing in opposite directions.

direction can be controlled. To quantify the carrier-envelope phase dependence of the electron emission, an asymmetry parameter $A(W, \phi_{CEP})$ is introduced, where W is the electron kinetic energy and ϕ_{CEP} is the carrier-envelope phase. It describes the ratio, for electrons of a given kinetic energy, between the difference of the integrated emission in a cone in the *up*-direction and *down*-directions on the momentum images divided by the sum of the emission into both directions:

$$A(W, \phi) = \frac{P_{up}(W, \phi_{CEP}) - P_{down}(W, \phi_{CEP})}{P_{up}(W, \phi_{CEP}) + P_{down}(W, \phi_{CEP})} \tag{6.1}$$

Here, P_{up} and P_{down} are cones of 50° opening angle along the polarization axis of the laser pulses [30]:

$$P_{up} = \int_{335°}^{360°} P(W, \phi_{CEP}) d\theta + \int_{0°}^{25°} P(W, \phi_{CEP}) d\theta \tag{6.2}$$

and

$$P_{down} = \int_{155^\circ}^{205^\circ} P(W, \phi_{CEP}) d\theta \tag{6.3}$$

Here 0° is the polarization direction of the laser pulses. In Fig. 6.3 (a) and (b) typical values of the asymmetry parameter of the electron emission from 109 nm ± 6% SiO_2 nanoparticles and xenon, respectively, are shown by a false color map as a function of the carrier-envelope phase and the electron kinetic energy. The laser intensity is $1.9 \cdot 10^{13}\ W/cm^2$ in both cases and is determined by the experimental cutoff energy of the electron emission from xenon with the cutoff energy expected from the rescattering model. The carrier-envelope phase is changed systematically over 3.7 π and for each value of the carrier-envelope phase an image, similar to those shown in Fig. 6.1 is recorded and the asymmetry parameter is determined for different electron kinetic energies. Positive numbers (reddish colors in Fig. 6.3) indicate preferential emission in the *up*-direction and negative numbers (bluish colors) indicate preferential emission in the *down*-direction. Both systems show a clear dependence of the direction of the electron emission on the carrier-envelope phase by oscillations between preferential emission in the *up* and *down*-directions as the carrier-envelope phase is varied. When the carrier-envelope phase is changed from 0 to π, the emission of fast electrons from the SiO_2 nanoparticles goes from being preferentially into the *up*-direction to being preferentially into the *down*-direction after going through a region of non-preferential emission with regard to the *up* and *down*-directions, where the asymmetry parameter is about zero. The absolute value of the carrier envelope phase is determined by the asymmetry of the electron emission in the cutoff region, where the electrons with the highest kinetic energy will be due to 180° backscattering relative to the polarization axis. This implies that they are especially sensitive to the absolute phase [85]. Changing the limits for the definitions of the *up* and *down* emission in eqs.

6.2 and 6.3 changes the absolute value of the asymmetry parameter but does not change the periodic structure of the electron emission when varying the carrier-envelope phase.

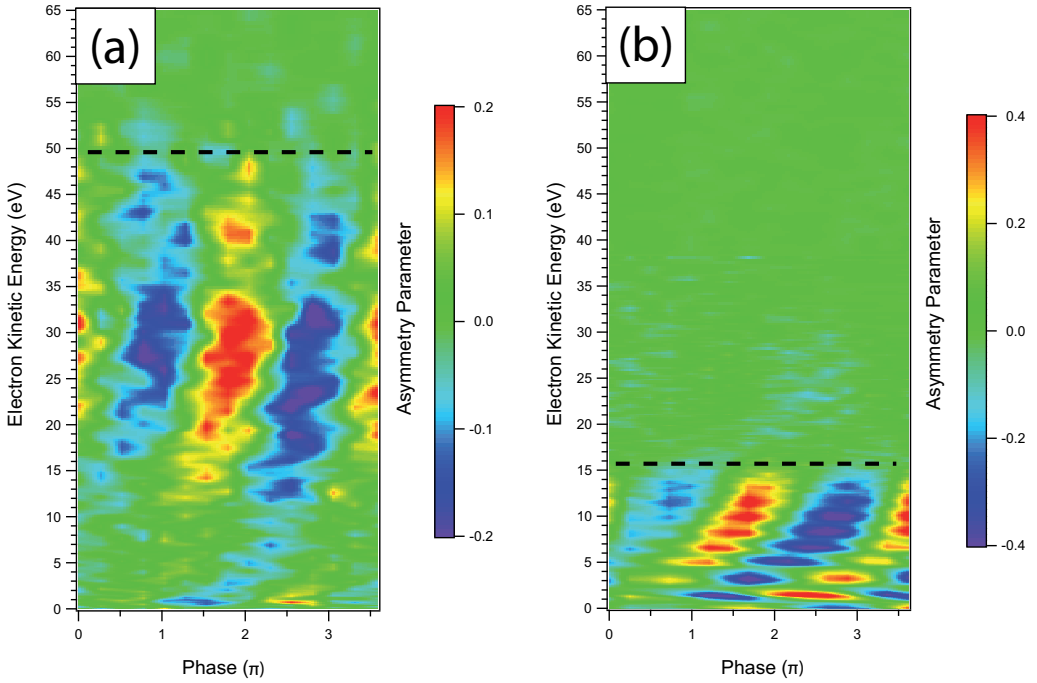

Figure 6.3: Asymmetry of electron emission in the *up* and *down*-direction from (a) free SiO_2 nanoparticles and (b) xenon as the carrier-envelope phase is systematically varied over 3.7 π. The clear carrier-envelope phase dependence can be observed for both systems that oscillates in phase for higher kinetic energies since the electrons with the highest kinetic energies corresponds to backscattered electrons. The diameter of the SiO_2 nanoparticles is 109 nm $\pm$ 6%.

It is noted that by exciting the free nanoparticles by few-cycle laser pulses one can treat the laser induced electron emission and acceleration separately from possible processes that take place on a longer time scale such as resonant heating and subsequent expansion [251, 252].

If the cutoff energy for the two systems is compared, one finds that the cutoff is

15.7±0.5 eV for the xenon atoms and 49.6±3.0 eV for the SiO_2 nanoparticles. The classical cutoff energy for the Xe atoms corresponds to 10 U_p, whereas the cutoff energy for the SiO_2 nanoparticles corresponds to 54.1±4.4 U_p. The cutoff energies are indicated by dashed lines in Fig. 6.3. They are assumed to be at the electron kinetic energy at which the carrier-envelope phase dependence terminates. This experiment is repeated for different sizes of the nanoparticles (central diameters of 52 nm, 82 nm, 105 nm, 109 nm and 147 nm and a polydispersity of ≈ 4-6% as determined by transmission electron microscopy) and using different laser peak intensities (1.0 - 4.5 10^{13} W/cm^2). The resulting cutoff energies as a function of the intensity are presented in Fig. 6.4 for different nanoparticle sizes.

Each experiment on the SiO_2 nanoparticles (corresponding to one point in Fig. 6.4) is repeated with xenon by using the same laser parameters in order to determine the peak intensity using the xenon cutoff. The cutoff for xenon is assumed to be $10.007U_p + 0.583I_p$, where I_P is the ionization energy of xenon, as suggested by Busuladzic et al. [253]. The results from Ref. [253] go beyond the classical picture of rescattering, where a value somewhat higher than the purely classical value of $10.007U_p$ [83] is found. Busuladzic et al.'s higher estimate of the cutoff energy is more in line with what has been observed experimentally [254, 255]. Having found the ponderomotive potential, the intensity of the radiation is calculated using the formula $I[W/cm^2] = \frac{U_p}{9.33^{-14}[eV](\lambda[\mu m])^2}$ where, if U_p is entered in units of eV and λ in units of μm yields peak intensities in units of W/cm^2.

For all nanoparticle sizes the cutoff energy is found to be significantly higher for the SiO_2 nanoparticles than the 10 U_p classical limit, as is known for rare gases, which is indicated by a dashed line in Fig. 6.4. Furthermore, when increasing the laser peak intensity, the cutoff energy of the emitted electrons

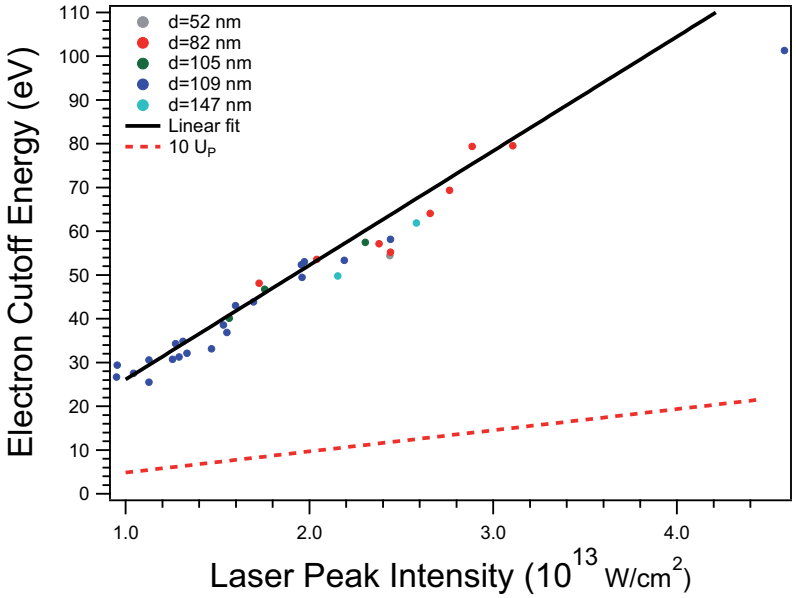

Figure 6.4: The cutoff energies for electron emission from free SiO_2 nanoparticles with different particle sizes in the laser peak intensity range $1.0 - 4.5\ 10^{13}\ W/cm^2$. A linear fit gives $53.0 \pm 0.6\ U_p$.

increase. However, a dependence on the size of the nanoparticles could not be observed. A linear fit through the data points in Fig. 6.4 yields a dependence of the cutoff energy on the laser intensity which in units of the ponderomotive potential is found to be $53.0 \pm 0.6\ U_p$.

6.3 Modeling the Enhanced Electron Acceleration

To understand the higher cutoff energies found in the electron emission from the SiO_2 nanoparticles compared to that from Xe, one has to consider the different environments in which the ionization and subsequent driving of the electrons by the laser field takes place and what influence that environment

has on the backscattering mechanism. The two different cases can be summed up as follows:

- (a) For the rare gas, the electron is set free and will be driven only by the applied laser field and can return to the ionic core that is otherwise surrounded by the vacuum. This corresponds to the case of the classical model.

- (b) For the nanoparticles, electrons is set free from a dielectric of a size which is much larger than the distance traveled by the electrons in the vacuum and will be polarized by the applied field. Due to the high local density of atoms in the nanoparticle as compared to rare gases, the electron will interact with the charged particles from other ionization events elsewhere on or near the nanoparticle surface.

A model is developed by Th. Fennel (University of Rosctock) in which the ionization and propagation of the electrons in an effective electric field is considered [249]. The effective electric field consists of: (i) The enhanced laser field due to the polarization of the nanoparticle and (ii) a Coulomb field due to free charges. This effective field is thus distinctly different from the field an electron set free from an isolated atomic gas will experience. The observation of enhanced cutoff energies in higher harmonics generation using 140 fs, $\lambda = 825$ nm from rare gas clusters has been attributed to higher electron recombination energies due to the locally enhanced field at the cluster surface [256]. In the present study, the interaction with the laser pulses is significantly different since no resonant heating takes place due to the short pulse length.
On the basis of this model, Monte Carlo simulations [257] are conducted. The ionization step is assumed to proceed *via* tunnel ionization at a surface atom. The rate of ionization is assumed to be given by the Ammosov-Delone-Krainov-

rate [258] using the field strength at the surface of the nanoparticle and the ionization potential of elemental silicon (7.16 eV) [259]. The tunnel ionization step is a purely quantum mechanical process, but the subsequent electron propagation is treated classically by the model. Rate equations are used for the propagation and scattering of electrons similar to what is used for charge transport in bulk materials [257]. The propagation of the electrons is given by

$$\ddot{r} = \frac{e}{m}\nabla\Phi^{Eff}(r) \tag{6.4}$$

where e and m are electron charge and mass and $\Phi^{eff}(r)$ is an effective potential, which not only includes the laser field but also contributions from the polarization of the nanoparticle and from free charges. Energy loss of the electrons due to inelastic scattering and collisional ionization is not taken into account.

6.3.1 Polarization of the Nanoparticle

Placing a dielectric sphere into an electric field, such as the SiO_2 nanoparticles in the laser field E_{Laser}, leads to a joint electric field that is given by the following expressions inside and outside the sphere:

$$E_y^{Inside} = E_{Laser}\frac{3}{\epsilon + 2} \tag{6.5}$$

and outside the sphere

$$E_y^{Outside} = E_{Laser}(1 - \frac{\epsilon - 1}{\epsilon + 2}\frac{R^3}{|y|^3}) \tag{6.6}$$

Here ϵ is the dielectric constant of the sphere. In Fig. 6.5 the field enhancement inside and around the sphere is shown in units of the unperturbed laser field.

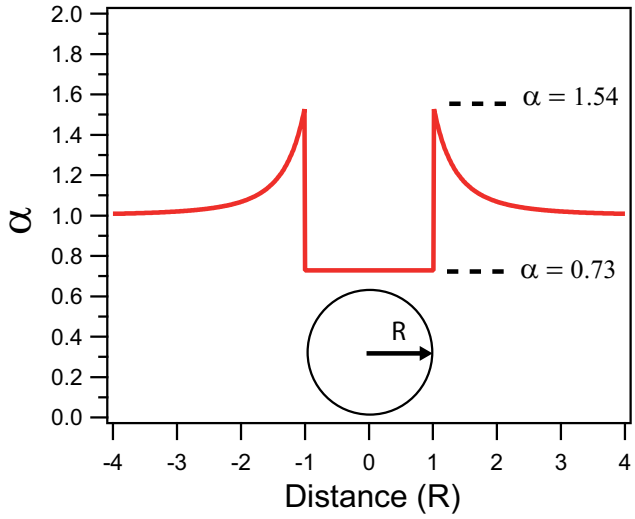

Figure 6.5: Field enhancement inside and outside a dielectric sphere with the radius R that is placed in an electrical field. The enhancement is at maximum at the poles of the sphere.

The center of the sphere is at distance 0. The radius is R, which corresponds to the surface of nanoparticle being located at -R and +R, respectively. The strongest enhancement is at the poles of the sphere (x=R) by a factor of 1.54 relative to the laser field without the presence of the dielectric sphere. Inside the sphere, the field is reduced relative to the unperturbed laser field and takes the value 0.73. For these values, a purely real dielectric constant for SiO_2 is assumed with the value $\epsilon = 2.12$ [260]. If a backscattering mechanism, similar to that considered for the atomic case, is assumed in the enhanced field, the maximum energy of rescattered electrons at the surface of the sphere at $y = |R|$ in the effective field is $10 \cdot \alpha^2 \, U_p = 10 \cdot 1.54^2 \, U_P = 23.72 \, U_p$ which is considerably lower than the experimentally observed cutoff energy of $53.0 \pm 0.6 \, U_P$.

Fig. 6.6 (a) shows a simulation of the kinetic energy distribution of the electron emission with rescattering at the nanoparticle surface in the effective field. The laser peak intensity for the simulation is $2.0 \cdot 10^{14} \; W/cm^2$.

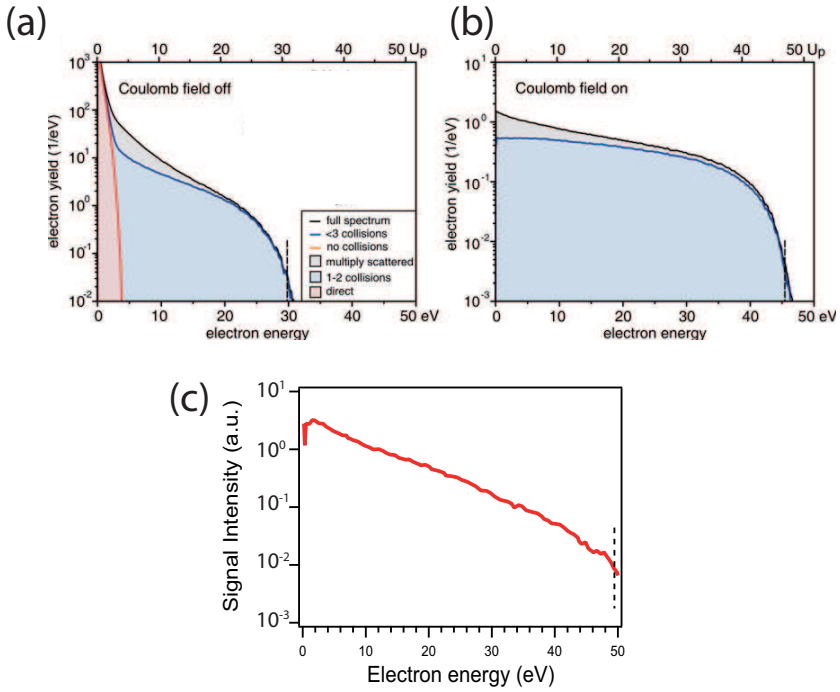

Figure 6.6: Simulations of the kinetic energy distribution of electrons emitted from SiO_2 nanoparticles after excitation by few-cacle lasers pulses at an intensity of $1.9 \cdot 10^{14}\ W/cm^2$. In (a) the field enhancement due to the polarization of the dielectric nanoparticle is considered and in (b) the Coulomb field due to free charges is also included. (c) shows a comparison to the experiment at similar laser parameters. Figure is taken from [249].

This is compared to Fig. 6.6 (c), which shows the experimental kinetic energy distribution at $1.9 \cdot 10^{14}\ W/cm^2$. The cutoff energy in the simulated spectrum is significantly lower than in the experimental spectrum ($\approx$ 30 eV vs. 49.6$\pm$3.0 eV). In addition to the lower cutoff energy in the simulated spectrum compared to the experimental one, the decrease of the signal is steeper in the simulated electron spectrum. In the simulated curve when using the enhanced field due to the nanoparticle polarization, the signal decreases by about four orders of magnitude in the kinetic energy range 0-30 eV. In the experimental curve, on the other hand, the decrease is slower at about two or-

ders of magnitude in the kinetic energy range 0-30 eV. Furthermore, electrons that have undergone different numbers of scattering events have been colored in Fig. 6.6 (a). Direct electron emission, i.e. without rescattering at the nanoparticle surface, is shown in red color and causes electrons of low kinetic energies. The cutoff for the direct emission is $4\ U_P$ which is in accordance with the classical $2U_P$ cutoff in a field enhanced by the nanoparticle polarization ($2\alpha^2\ U_P = 2 \cdot 1.54^2\ U_P = 4.74\ U_P$ at the poles of the nanoparticle). Electrons that undergo 1-2 (shown in blue color) and more than 2 scattering events (shown in gray color) extend to higher kinetic energies. This is similar to the atomic case, where the returning electron can undergo one or more scattering event. As in the atomic case, the electrons at the cutoff limit have undergone one scattering event.

6.3.2 Free Charges

Free charges, i.e. electrons as well as ions, constitute a third part of the effective driving field. In Fig. 6.6 (b) the simulation is repeated using an effective field that also includes free charges at or near the nanoparticle surface. In the simulation, $\approx 10^6$ electrons are let propagate simultaneously so that the effect of free charges can be evaluated.

When including the Coulomb field due to the free charges, the cutoff extends to higher kinetic energies and shows a better agreement with the experimentally observed cutoff. The contribution of direct emission with no rescattering (red color in Fig. 6.6 (a)) vanishes as the direct electrons get trapped at the surface and cannot leave the nanoparticle to be detected. When comparing the simulation done using free charges (Fig. 6.6 (b)) with those done without free charges (Fig. 6.6 (a)) is it seen that the simulation including the Coulomb field from free charges shows a less steep decrease which is more in resem-

blance to the experimental electron spectrum (fig. 6.6 (c)). This is mostly due to trapping of the direct electron emission. The free charges discussed in this Section are all located at other sites of the same nanoparticle. Only a single nanoparticle is probed at any given time due to the low nanoparticle density (i.e. $\approx 10^6/\mathrm{cm}^3$) in the interaction region so that any influence from charges on neighboring nanoparticles can be neglected.
Including the Coulomb field in the simulations has two effects that are considered:

- It loosens the birth time requirements, as defined by the time during the pulse at which the electron is released into the vacuum. With the Coulomb field the time window in which electrons can be emitted and reach the maximum kinetic energy after rescattering is larger.

- Repulsion of fast electrons by slow electrons near the surface. This corresponds to a many-electron effect.

In Fig. 6.7 (a) and (b), the result of simulations of the phase space distribution of the electrons is shown 35 fs after the peak of the laser pulse. This corresponds to the pulse already having left the ionization region. The laser intensity is $2 \cdot 10^{14}\ W/cm^2$ (as in Fig. 6.6) and the carrier-envelope phase is set at $\Phi_{CEP} = 0$, which corresponds to the maximum of the electric field pointing in the *up*-direction (cf. Fig. 6.2 (a)). Shown are the cases when only a field enhancement due to the nanoparticle polarization is included (cf. Fig. 6.7 (a)) and when an additional component from free charges in also included (Fig. 6.7 (b)). In Fig. 6.7 (a), kinetic energies of electrons in *up*-direction extend up to ≈ 30 eV, whereas the kinetic energies of the electrons emitted in *down*-direction extend to ≈ 25 eV. This corresponds to control of the emission direction due to waveform controlled the few-cycle laser pulses. In Fig. 6.7 (b),

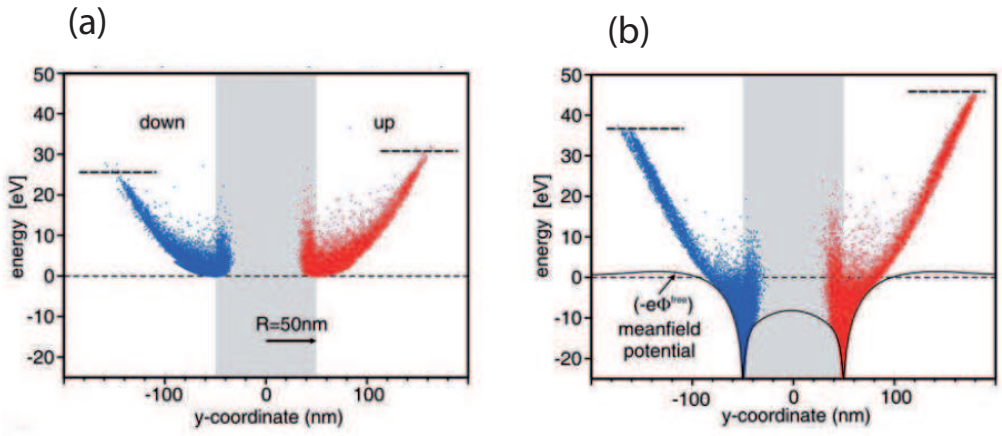

Figure 6.7: Phase space map of simulated electron emission from SiO_2 nanoparticles 35 fs after the peak of the laser pulse. The carrier-envelope phase is 0. In (a) the electron emission in the *up* and *down*-directions is simulated in an enhanced field due to the polarization of the SiO_2 nanoparticles. In (b), a contribution from free charges is included. See text for details. Figure is taken from [249].

a contribution from the Coulomb field due to free charges is included. Here, the kinetic energies of the electrons emitted in the *up* and *down*-directions, respectively, both extend to higher values than in the simulation without the Coulomb field, with the electrons emitted in the *up*-direction extending to the highest kinetic energies. The contribution from the free charges causes slow electrons (mostly directly emitted electrons without rescattering) to be trapped near the nanoparticles.

For further analysis of the contribution from free charges, Fig. 6.8 shows the results of the simulations with respect to the birth time of the electrons. The laser parameters are the same as in Fig. 6.7. In Fig. 6.8 (a) and (b) the kinetic energies of the electrons are shown as a function of their birth time within the laser pulse with and without including the Coulomb field, respectively. The analysis of Fig. 6.8 reveals that the fastest electrons are born shortly after

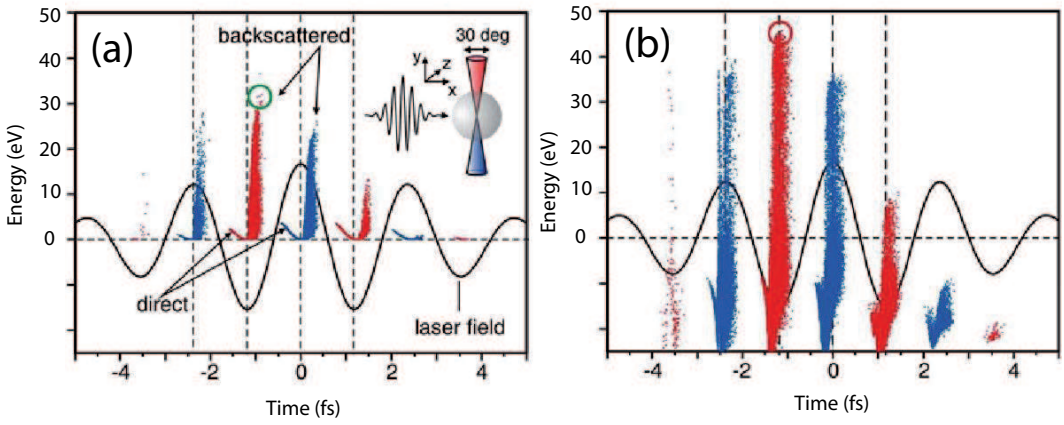

Figure 6.8: Simulation of the kinetic energy of emitted electrons as a function of the birth time during the laser pulse. In (a) an enhanced field due to the nanoparticle polarization is included, and in (b) a contribution from free charges is included as well. The laser parameters are the same as in Figs. 6.6 and 6.7. See text for details. Figure is taken from [249].

the maximum of the field amplitude when the Coulomb field is not included. This is similar to the case for xenon atoms where the highest kinetic energy electrons are set free shortly after the maximum of the fied amplitude [85] (cf. Chapter 2). In contrast to this, electrons that are directly emitted without ever returning to the ionic core have birth times before the maximum. When including a contribution from free charges, however, the electrons that end up with the highest kinetic energies are born at or shortly before the maximum of the laser field amplitude. Thus the free charges cause a loosening of the birth time requirements leading to higher kinetic energies of backscattered electrons. After the fast electrons have left the nanoparticles and the laser pulse has left the interaction region, a smaller additional acceleration (typically 5 eV for 50 eV total energy) is caused by space-charge repulsion between the liberated electrons. The ionization and acceleration mechanism discussed here is different from the one responsible for electron acceleration from clusters

when interacting with ultra-short laser pulses which is attributed to resonant plasmon excitation in the clusters [261, 262].

Fig. 6.9 shows the experimentally observed cutoff energies from SiO_2 nanoparticles as a function of the laser peak intensity for different sizes (similar to Fig. 6.4) and includes the cutoff intensities obtained from simulations similar to those described, but for different laser peak intensities. The green line with triangles shows the cutoff obtained from simulations, which include free charges, as discussed above and the purple line with squares describes the cutoff energies derived when free charges are not included in the simulations. The case that is discussed above at an intensity of $2 \cdot 10^{13}\ W/cm^2$ is thus one of the green triangles and purple squares, respectively, when including or not including the contribution from the free charges. The cutoff intensities obtained from simulations when including a contribution from free charges is higher than when not including them. For the entire laser intensity range that is studied here, the simulations including an effective field composed of an enhanced laser field due to the polarization of the spherical dielectric nanoparticles and contributions from free charges at or near the nanoparticle surface give good agreement with the experimentally observed cutoff energies.

6.3.3 Size dependence

In the experiment, no dependence of the cutoff energy on the size of the nanoparticles is found (cf. Fig. 6.4). The simulations predict a slight size dependence in the studied size range due to larger contributions from the Coulomb field for larger nanoparticles such that the cutoff energies will be somewhat higher for larger nanoparticles. The experimental accuracy is likely not high enough to detect the size dependence in this size range.

Another aspect that can lead to size dependent processes in the interaction of

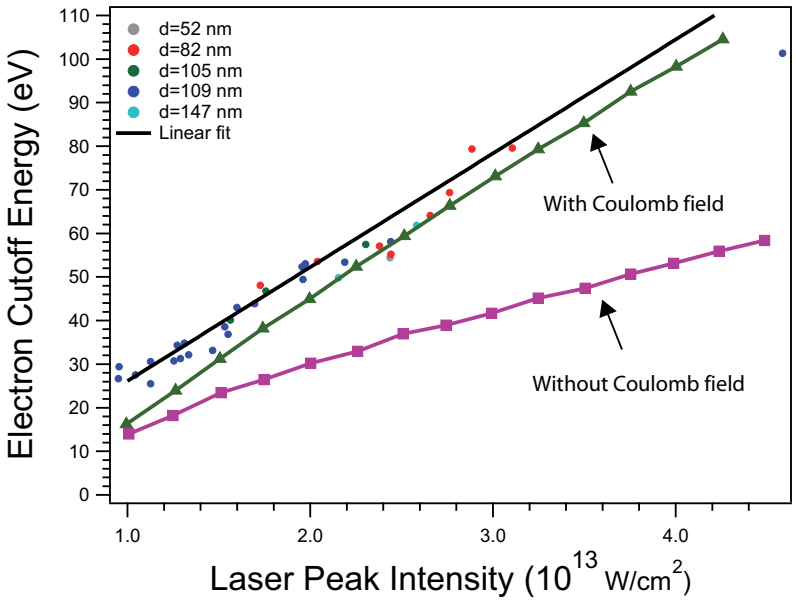

Figure 6.9: The cutoff energies for electrons from the SiO_2 nanoparticles for different particle sizes in the laser peak intensity range $1.0-4.5\ 10^{13}\ W/cm^2$. In addition to the experimental point, cutoff energies obtained with simulations including (i), and not including (ii) a contribution from free charges are shown. See text for details.

dielectric spheres with ultra-short laser pulses is concerned with the propagation of the light within the sphere. The simulations discussed here are done using the dipole approximation (Eqs. 6.5 and 6.6). This is permissible as the wavelength of the radiation is much larger than the size of the nanoparticles. In the experiments reported here, the nanoparticles have a diameter of 52-147, nm whereas the laser central wavelength is 720 nm. If, however, the experiments were to be repeated with either larger nanoparticles or shorter wavelengths one would expect an angular asymmetry in the emission due to propagation of the light within the nanoparticle. This effect should becoma visible by a backward/forward asymmetry of the electron emission. Field distribution effects on the angular distribution of electron emission from nanoparticles has been reported by Wilson et al. [165], where NaCl nanoparticles with diameters

of 50-500 nm were excited with vacuum ultraviolet radiation (hν = 10.9 eV, i.e. λ =113.7 nm). In that study, the attenuation length of the radiation was comparable to the size of the nanoparticles and photoemission was seen to be preferentially from the side facing the incoming radiation. When using laser pulses in the infrared or visible spectral regimes, SiO_2 is essentially transparent, and the asymmetry is expected to be due to nanofocusing at the backside of the nanoparticle [263, 264].

6.4 Conclusions and Outlook

In conclusion free SiO_2 nanoparticles are excited by carrier-envelope phase stabilized few-cycle laser pulses (pulse length $\approx$ 5 fs, central wavelength 720 nm) and the subsequent electron emission is recorded using velocity map imaging. The emission from the nanoparticles is compared to the electron emission from atomic xenon at the same laser peak intensities which are varied in the range 1.0 - 4.5 10^{13} W/cm^2. For both systems, the emission direction could be controlled by varying the carrier-envelope phase. A higher cutoff energy is observed for the electrons emitted from the nanoparticles compared to those from the xenon. In units of the ponderomotive potential, U_p, the cutoff energy for the electrons emitted from the nanoparticles is found to be $53.0 \pm 0.6 U_p$ which is considerably higher than the 10 U_p classical limit known for xenon. These differences are discussed in terms of a novel acceleration mechanism in which the electrons undergo tunnel ionization from surface Si atoms. These are accelerated in the effective electric field and can return to the surface of the nanoparticle where they are backcattered. Simulations of the electron emission and acceleration with an effective electric field assuming contributions from the laser field, polarization of the nanoparticle, and a Coulomb-field due

to free charges near the nanoparticle surface are found to accurately describe the higher cutoff energies from the nanoparticles as well as the kinetic energy distribution of the emitted electrons.

This mechanism is likely neither specific to SiO_2 nor to nanoparticles in general. Is should be present for all dielectric solids since it is a property of the surface rather than a property of the nanoparticles. However, free nanoparticles in a particle beam are ideal systems to study this effect for two reasons: Firstly, nanoparticles have a high surface-to-bulk ratio, which makes free nanoparticles an ideal system to study electron rescattering mechanism since the rescattering happens at or near the surface. Secondly, the nanoparticle beam approach makes sure that damage to the particles due to the strong laser pulses can be neglected, since fresh sample is continuously fed to the interaction region with the laser pulses.

Enhanced electron acceleration at nanoparticle surfaces may find applications where electron recollision is utilized such as in the generation of higher harmonics pulses where it can be expected that higher photon energies are attainable compared to atomic targets because of the higher recollision energy of the electrons.

Chapter 7

Conclusions

In this work, free SO_2 nanoparticles in a continuous particle beam are studied by soft X-rays and short-pulse laser radiation in the visible regime. By preparing the nanoparticles in a beam which propagates in high vacuum, their intrinsic properties can be studied without any interaction with a surrounding medium. Furthermore, radiation damage to the nanoparticles following interactions with the ionizing radiation or intense radiation can be avoided since the nanoparticle beam continuously supplies fresh sample to the interaction area with the soft X-rays or few-cycle laser pulses. The following results are obtained from the experimental studies:

- Emission of one or more electrons from free SiO_2 nanoparticles after excitation by soft X-rays and extreme ultraviolet radiation is recorded using time-of-flight photoelectron spectroscopy. Valence electron and Auger electron emission is observed for the first time from free, size-selected SiO_2 nanoparticles. In addition, emission of inner-shell electrons and secondary electrons is clearly distinguished, where emission of secondary electrons is the dominant photoemission channel.

  Electron-electron coincidence spectroscopy reveals emission of more than

one electron after the absorption of one soft X-ray photon. The emission of two secondary electrons is the dominant two-electron emission channel. Emission of inner-shell electrons in coincidence with Auger electrons, with a secondary electron caused by the Auger electron, and with inelastically scattered Auger electrons are also observed.

- Elastic scattering of soft X-rays from free SiO_2 nanoparticles is recorded in the small angle scattering regime (1.2-9.3°). The angular distribution of the elastically scattered soft X-rays is found to be strongly forward oriented and the shape of the scattering pattern shows distinct minima and maxima. The position of these minima and maxima is influenced by the size distribution of the nanoparticles and their complex refractive index. By using the Mie formalism, the angle resolved scattering patterns are used to determine the average diameter and the polydispersity of the nanoparticles.

  In the range of inner shell absorption edges, the photon energy dependent refractive index is determined. For an unambiguous determination of the refractive index, it is shown that the size distribution needs to be determined first at a photon energy where the density of the material does not significantly influence the positions of the minima and maxima in the scattering patterns. This analysis is performed at a photon energy of 375 eV. The photon energy dependent refractive index near the Si 2p (106-115 eV) and O 1s (530-550 eV) absorption edges is determined. These results are compared with refractive index data obtained by reflectometry on bulk amorphous SiO_2. For the nanoscopic SiO_2, the real part of the refractive index is generally higher and the imaginary part lower than for bulk amorphous SiO_2. This is discussed in the context of the porosity of the SiO_2 nanoparticles.

- Photoemission from free SiO_2 nanoparticles is studies after excitation by phase-stabilized few-cycle laser pulses (pulse length: $\approx$ 5 fs, central wavelength: 720 nm). By varying the carrier-envelope phase of the laser pulses, the electron emission direction is controlled.

  The cut-off energies for electron emission from the nanoparticles is found to be 53.0$\pm$0.6 U_P where U_P is the ponderomotive potential. A comparison with the electron emission from atomic xenon reveals that the cut-off energies for the nanoparticles is significantly higher than the classical 10 U_P limit, which is known for rare gases. This electron acceleration is attributed to the electron rescattering from the surface of the particles in the locally enhanced field. A model is developed by Th. Fennel which considers the rescattering in an effective field that includes contributions from local field enhancement at the poles of the dielectric nanoparticles and contributions from free charges at or near the surface. Monte-Carlo simulations of the electron emission and rescattering yield good agreement with the experimental findings.

These results show the feasibility of studying free nanoparticles in a beam to probe their size, shape, electronic structure, ionization dynamics and nonlinear response to strong electromagnetic fields without the need to deposit them on a substrate. Interesting avenues of further studies would be to use the nanoparticle beam technique to investigate smaller nanoparticles in the sub 10 nm regime, where the size gap to clusters can be fully closed. For instance, quantum size effects can be systematically explored by the use of soft X-rays for studying free quantum dots. Further, chemical reactions taking place on the surface of free nanoparticles, e.g. in catalysis or atmospheric chemistry are also important subjects where a lack of knowledge exists. The application of soft X-ray free electron lasers seems to be another promising way to study free

nanoparticles, since they combine the characteristics of both light sources used in this work, namely yielding intense soft X-rays pulses with pulse lengths in the femtosecond regime.

Bibliography

[1] S. Banerjee, J. Das, R. P. Alvarez, S. Santra, *New J. Chem.* **34** 302 (2010)

[2] D. Napierska, L. C. J. Thomassen, D. Lison, J. A. Martens, P. H. Hoet, *Part. Fibre Toxicol.* **7** 39 (2010)

[3] V. V. Potapov, E. S. Shitikov, N. S. Trutnev, V. A. Gorbach, N. N. Portnyagin, *Glass. Phys. Chem.* **37** 98 (2011)

[4] J. Lademann, H. Richter, A. Teichmann, N. Otberg, U. Blume-Peytavi, J. Luengo, B. Weiß, U. F. Schaefer, C.-M. Lehr, R. Wepf, W. Sterry, *Eur. J. Pharm. Biopharm.* **66** 159 (2007)

[5] B. T. Draine, *Annu. Rev. Astron. Astrophys.* **41** 241 (2003)

[6] B. T. Draine, *Astrophys. J.* **598** 1026 (2003)

[7] H. B. Perets, A. Lederhendler, O. Biham, G. Vidali, L. Li, S. Swords, E. Congiu, J. Roser, G. Manico, J. R. Brucato, V. Pirronello, *Astrophys. J.* **661** L163 (2007)

[8] P. R. Buseck, M. Posfai, *Proc. Natl. Acad. Sci. USA* **96** 3372 (1999)

[9] T. Novakov, J. E. Penner, *Nature* **365** 823 (1993)

[10] V. Ramanathan, P. J. Crutzen, J. T. Kiehl, D. Rosenfeld, *Science* **294** 2119 (2001)

[11] U. Dusek, G. P. Frank, L. Hildebrandt, J. Curtius, J. Schneider, S. Walter, D. Chand, F. Drewnick, S. Hings, D. Jung, S. Borrmann, M. O. Andreae, *Science* **312** 1375 (2006)

[12] T. K. Barik, B. Sahu, V. Swain, *Parasitol. Res.* **103** 253 (2008)

[13] S. T. Stern, S. E. McNeil, *Toxicol. Sci.* **101** 4 (2008)

[14] G. Orr, D. J. Panther, K. J. Cassens, J. L. Phillips, B. J. Tarasevich, J. G. Pounds, *Toxicol. Appl. Pharm.* **236** 210 (2009)

[15] K. M. Waters, L. M. Masiello, R. C. Zangar, B. J. Tarasevich, N. J. Karin, R. D. Quesenberry, S. Bandyopadhyay, J. G. Teeguarden, J. G. Pounds, B. D. Thrall, *Toxicol. Sci.* **107(2)** 553 (2009)

[16] G. Oberdörster, E. Oberdörster, J. Oberdörster, *Environ. Health Persp.* **113** 823 (2005)

[17] K. Yamashita, Y. Yoshioka, K. Higashisaka, K. Mimura, Y. Morishita, M. Nozaki, T. Yoshida, T. Ogura, H. Nabeshi, K. Nagano, Y. Abe, H. Kamada, Y. Monobe, T. Imazawa, H. Aoshima, K. Shishido, Y. Kawai, T. Mayumi, S. Tsunoda, N. Itoh, T. Yoshikawa, I. Yanagihara, S. Saito, Y. Tsutsumi, *Nature Nanotech.* **6** 321 (2011)

[18] D. Drescher, G. Orts-Gil, G. Laube, K. Natte, R. W. Veh, W. Österle, J. Kneipp, *Anal. Bioanal. Chem.* **400** 1367 (2011)

[19] W. Lin, Y.-W. Huang, X.-D. Zhou, Y. Ma, *Toxicol. Appl. Pharm.* **217** 252 (2006)

[20] O. Ponomarenko, A. Y. Nikulin, H. O. Moser, P. Yang, O. Sakata, *J. Synchrotron Rad.* **18** 580 (2011)

[21] H. Döllefeld, C. McGinley, S. Almousalami, T. Möller, H. Weller, A. Eychmüller, *J. Chem. Phys.* **117** 8953 (2002)

[22] E. R. Mysak, D. E. Starr, K. R. Wilson, H. Bluhm, *Rev. Sci. Instrum.* **81** 016106 (2010)

[23] J. Meinen, S. Khasminskaya, M. Eritt, T. Leisner, E. Antonsson, B. Langer, E. Rühl, *Rev. Sci. Instrum.* **81** 085107 (2010)

[24] B. Berge, K. Sudholz, B. Steiner, J. Rohmann, E. Rühl, *Phys. Chem. Chem. Phys.* **1** 5485 (1999)

[25] B. Steiner, B. Berge, R. Gausmann, J. Rohmann, E. Rühl, *Appl. Optics* **38** 1523 (1999)

[26] E. J. Davis, *Aerosol Sci. Tech.* **26** 212 (1997)

[27] D. Duft, T. Leisner, *Int. J. Mass Spectrom.* **233** 61 (2004)

[28] H. Bresch, B. Wassermann, B. Langer, C. Graf, R. Flesch, U. Becker, B. Österreicher, T. Leisner, E. Rühl, *Faraday Discuss.* **137** 389 (2008)

[29] J. Shu, K. R. Wilson, M. Ahmed, S. R. Leone, C. Graf, E. Rühl, *J. Chem. Phys.* **124** 034707 (2006)

[30] M. F. Kling, J. Rauschenberger, A. J. Verhoef, E. Hasovic, T. Uphues, D. B. Milosevic, H. G. Muller, M. J. J. Vrakking, *New J. Phys.* **10** 025024 (2008)

[31] I. Znakovskaya, P. von den Hoff, S. Zherebtsov, A. Wirth, O. Herrwerth, M. J. J. Vrakking, R. de Vivie-Riedle, M. F. Kling, *Phys. Rev. Lett.* **103** 103002 (2009)

[32] W. A. de Heer, *Rev. Mod. Phys.* **65** 611 (1993)

[33] O. Echt, K. Sattler, E. Recknagel, *Phys. Rev. Lett.* **47** 1121 (1981)

[34] O. Echt, K. Sattler, E. Recknagel, *Phys. Lett. A* **90** 185 (1982)

[35] W. D. Knight, K. Clemenger, W. A. de Heer, W. A. Saunders, M. Y. Chou, M. L. Cohen, *Phys. Rev. Lett.* **52** 2141 (1984)

[36] R. Lewinski, C. Graf, B. Langer, R. Flesch, H. Bresch, B. Wassermann, E. Rühl, *Eur. Phys. J.-Spec. Top.* **169** 67 (2009)

[37] F. Baletto, R. Ferrando, *Rev. Mod. Phys.* **77** 312 (2005)

[38] J. P. Wilcoxon, B. L. Abrams, *Chem. Soc. Rev.* **35** 1162 (2006)

[39] P. Buffat, J.-P. Borel, *Phys. Rev. A* **13** 2287 (1976)

[40] A. Schmidt-Ott, P. Schurtenberger, H. C. Siegmann, *Phys. Rev. Lett.* **45** 1284 (1980)

[41] M. Förstel, M. Mucke, T. Arion, T. Lischke, S. Barth, V. Ulrich, G. Öhrwall, O. Björneholm, U. Hergenhahn, A. M. Bradshaw, *Phys. Rev. B* **82** 125450 (2010)

[42] C. Binns, *Surf. Sci. Rep.* **44** 1 (2001)

[43] W. T. Doyle, *Phys. Rev. B.* **39** 9852 (1989)

[44] L. D. Pachon, G. Rothenberg, *Appl. Organometal. Chem.* **22** 288 (2008)

[45] O. Björneholm, G. Öhrwall, M. Tchaplyguine, *Nucl. Instrum. Meth. A* **601** 161 (2009)

[46] W. G. Kreyling, M. Semmler-Behnke, Q. Chaudhry, *Nano Today* **5** 165 (2010)

[47] L. T. Minassian-Saraga, *Pure. Appl. Chem.* **66** 1667 (1994)

[48] E. Chagarov, A. A. Demkov, J. B. Adams, *Phys. Rev. B* **71** 075417 (2005)

[49] G. S. Smith, L. E. Alexander, *Acta Cryst.* **16** 462 (1963)

[50] M. G. Tucker, M. T. Dove, D. A. Keen, *J. Phys.: Condens. Matter* **12** L425 (2000)

[51] D. H. Everett, *Pure Appl. Chem.* **31** 577 (1972)

[52] W. Stöber, A. Fink, E. Bohn, *J. Coll. Int. Sci.* **26** 62 (1968)

[53] K. S. Rao, K. El-Hami, T. Kodaki, K. Matsushige, K. Makino, *J. Colloid Interf. Sci.* **289** 125 (2005)

[54] A. P. Philipse, *Colloid Polym. Sci.* **266** 1174 (1988)

[55] G. H. Bogush, C. F. Zukoski, *J. Colloid Interf. Sci.* **142** 19 (1991)

[56] A. van Blaaderen, J. van Geest, A. Vrij, *J. Colloid Interf. Sci.* **154** 481 (1992)

[57] G. H. Bogush, M. A. Tracy, C. F. Zukoski, *J. Non-Cryst. Solids* **104** 95 (1988)

[58] C. Lourenco, M. Teixeira, S. Simoes, R. Gaspar, *Int. J. Pharm.* **138** 1 (1996)

[59] B. Langer, U. Becker, *Nucl. Instrum. Meth. A* **601** 78 (2009)

[60] N. Nagaya, M. Yao, T. Hayakawa, Y. Ohmasa, Y. Kajihara, M. Ishii, Y. Katayama, *Phys. Rev. Lett.* **89** 243401 (2002)

[61] P. J. Cumpson, *J. Electron Spectrosc.* **73** 25 (1995)

[62] K. Kobayashi, *Nucl. Instrum. Meth. A* **601** 32 (2009)

[63] M. O. Krause, *J. Phys. Chem. Ref. Data* **8** 307 (1979)

[64] C. J. Powell, *J. Electron Spectrosc.* **47** 197 (1988)

[65] B. L. Henke, J. Liesegang, S. D. Smith, *Phys Rev. B* **19** 3004 (1979)

[66] W. S. M. Werner, *Phys. Rev. B* **52** 2964 (1995)

[67] W. S. M. Werner, W. Smekal, H. Störi, H. Winter, G. Stefani, A. Ruocco, F. Offi, R. Gotter, A. Morgante, F. Tommasini, *Phys. Rev. Lett.* **94** 038302 (2005)

[68] H.-J. Fitting, J. Boyde, J. Reinhardt, *Phys. Status Solidi A* **81** 323 (1984)

[69] V. S. Kortov, S. V. Zvonarev, E. Schreiber, H.-J. Fitting, *J. Electron Spectrosc.* **173** 79 (2009)

[70] E. Schreiber, H.-J. Fitting, *J. Electron Spectrsc.* **124** 25 (2002)

[71] T. Fennel, K.-H. Meiwes-Broer, J. Tiggesbäumker, P.-G. Reinhard, P. M. Dinh, E. Suraud, *Rev. Mod. Phys* **82** 1793 (2010)

[72] T. Pfeifer, C. Spielmann, G. Gerber, *Rep. Prog. Phys.* **69** 443 (2006)

[73] T. Brabec, F. Krausz, *Rev. Mod. Phys.* **72** 545 (2000)

[74] J. Mauritsson, *Temporal Aspects of High-Intensity Laser-Matter Interactions*, Ph.D. thesis, Lund Institute of Technology (2003)

[75] M. Protopapas, C. H. Keitel, P. L. Knight, *Rep. Prog. Phys.* **60** 389 (1997)

[76] W. Becker, F. Grasbon, R. Kopold, D. B. Milosevic, G. G. Paulus, H. Walther, *Adv. Atom. Mol. Opt. Phys.* **48** 35 (2002)

[77] Z. Chang, A. Rundquist, H. Wang, M. M. Murnane, H. C. Kapteyn, *Phys. Rev. Lett.* **79** 2967 (1997)

[78] J. L. Krause, K. J. Schafer, K. C. Kulander, *Phys. Rev. Lett.* **68** 3535 (1992)

[79] P. B. Corkum, *Phys. Rev. Lett.* **71** 1994 (1993)

[80] B. Feuerstein, R. Moshammer, J. Ullrich, *J. Phys. B: At. Mol. Opt. Phys.* **33** L823 (2000)

[81] P. Kruit, J. Kimman, H. G. Muller, M. J. van der Wiel, *Phys. Rev. A* **28** 248 (1983)

[82] G. G. Paulus, W. Becker, H. Walther, *Phys. Rev. A* **52** 4043 (1995)

[83] G. G. Paulus, W. Becker, W. Nicklich, H. Walther, *J. Phys. B: At. Mol. Opt. Phys.* **27** L703 (1994)

[84] X. Y. Lai, W. Quan, X. Liu, *Phys. Rev. A* **84** 025401 (2011)

[85] G. G. Paulus, F. Lindner, H. Walther, A. Baltuska, E. Goulielmakis, M. Lezius, F. Krausz, *Phys. Rev. Lett.* **91** 253004 (2003)

[86] O. Glatter, O. Kratky (eds.), *Small Angle X-ray Scattering*, Academic Press, London (1982)

[87] G. Mie, *Ann. Phys.* **330** 377 (1908)

[88] H. Horvath, *J. Quant. Spectrosc. RA* **110** 787 (2009)

[89] C. F. Bohren, D. R. Huffman, *Absorption and Scattering of Light by Small Particles*, Wiley-VCH Verlag GmbH, Weinheim (1983)

[90] W. J. Wiscombe, *Appl. Optics* **19** 1505 (1980)

[91] C. Mätzler, *MATLAB Functions for Mie Scattering and Absorption*, University of Bern, Institut für Angewandte Physik (2002)

[92] H. Ade, C. Wang, A. Garcia, H. Yan, K. E. Sohn, A. Hexemer, G. C. Bazan, T.-Q. Nguyen, E. J. Kramer, *J. Polym. Sci. Pol. Phys.* **47** 1291 (2009)

[93] K. R. May, *J. Aerosol Sci.* **4** 235 (1973)

[94] TSI Incorporated, Shoreview, MN 55126 USA, *Model 3075/3076 Constant Output Atomizer - Instruction Manual*, I edn. (2003)

[95] R. P. Bagwe, L. R. Hilliard, W. Tan, *Langmuir* **22** 4357 (2006)

[96] C.-J. Tsai, J.-S. Lin, C. G. Deshpande, L.-C. Liu, *Part. Part. Syst. Charact.* **22** 293 (2005)

[97] TSI Incorporated, Shoreview, MN 55126 USA, *Model 3062 Diffusion Dryer - Instruction Manual*, I edn. (2003)

[98] P. Liu, P. J. Ziemann, D. B. Kittelson, P. H. McMurry, *Aerosol Sci. Tech.* **22** 314 (1995)

[99] X. Wang, F. E. Kruis, P. H. McMurry, *Aerosol Sci. Tech.* **39** 611 (2005)

[100] X. Wang, A. Gidwani, S. L. Girshick, P. H. McMurry, *Aerosol Sci. Tech.* **39** 624 (2005)

[101] J. Meinen, *TRAPS the key to atmospheric nano-science*, Ph.D. thesis, Ruperto-Carola University of Heidelberg (2010)

[102] X. Zhang, K. A. Smith, D. R. Worsnop, J. Jimenez, J. T. Jayne, C. E. Kolb, *Aerosol Sci. Tech.* **36** 617 (2002)

[103] X. Zhang, K. A. Smith, D. R. Worsnop, J. Jimenez, J. T. Jayne, C. E. Kolb, J. Morris, P. Davidovits, *Aerosol Sci. Tech.* **38** 619 (2004)

[104] H. Bresch, *Photoionisation von freien Aerosolpartikeln mit Synchrotronstrahlung*, Ph.D. thesis, Freie Universität Berlin (2007)

[105] X. Wang, P. H. McMurry, *Aerosol Sci. Tech.* **40** 320 (2006)

[106] X. Wang, P. H. McMurry, *Aerosol Sci. Tech.* **40** 1 (2006)

[107] J. H. Moore, C. C. Davis, M. A. Coplan, *Building Scientific Apparatus*, Perseus Books, Reading, Massachusetts, 2nd edn. (1991)

[108] A. Wiedensohler, H. J. Fissan, *J. Aerosol Sci.* **19** 867 (1988)

[109] A. Wiedensohler, *J. Aerosol Sci.* **19** 387 (1988)

[110] A. Wiedensohler, P. Büscher, H.-C. Hansson, B. G. Martinsson, F. Stratmann, G. Ferron, B. Busch, *J. Aerosol Sci.* **25** 639 (1994)

[111] E. Andersson, *Multi-Electron Coincidence Studies of Atoms and Molecules*, Ph.D. thesis, Uppsala University (2010)

[112] R. Lewinski, *Lokale elektronische und strukturelle Eigenschaften freier Nanopartikeln*, Ph.D. thesis, Freie Universität Berlin (2010)

[113] T. Arion, *Ionization and fragmentation of chalcogene clusters by highly charged ions and synchrotron radiation*, Ph.D. thesis, Freie Universität Berlin (2008)

[114] K. J. S. Sawhney, F. Senf, M. Scheer, F. Schäfers, J. Bahrdt, A. Gaupp, W. Gudat, *Nucl. Instrum. Meth. A* **390** 395 (1997)

[115] K. Godehusen, H.-C. Mertins, T. Richter, P. Zimmermann, M. Martins, *Phys. Rev. A* **68** 012711 (2003)

[116] J. Rauschenberger, *Phase-stabilized Ultrashort Laser Systems for Spectroscopy*, Ph.D. thesis, Ludwig-Maximilians-Universität München (2007)

[117] M. F. Kling, C. Siedschlag, A. J. Verhoef, J. I. Khan, M. Schultze, T. Uphues, Y. Ni, M. Uiberacker, M. Drescher, F. Krausz, M. J. J. Vrakking, *Science* **312** 246 (2006)

[118] I. Znakovskaya, P. von den Hoff, N. Schirmel, G. Urbasch, S. Zherebtsov, B. Bergues, R. de Vivie-Riedle, K.-M. Weitzel, M. F. Kling, *Phys. Chem. Chem. Phys.* **13** 8653 (2011)

[119] M. Nisoli, S. De Silvestri, O. Svelto, *Appl. Phys. Lett.* **68** 2793 (1996)

[120] M. Nisoli, S. De Silvestri, O. Svelto, R. Szipöcs, K. Ferencz, C. Spielmann, S. Sartania, F. Krausz, *Opt. Lett.* **22** 522 (1997)

[121] J. Rauschenberger, T. Fuji, M. Hentschel, A.-J. Verhoef, T. Udem, C. Gohle, T. W. Hänsch, F. Krausz, *Laser Phys. Lett.* **3** 37 (2006)

[122] G. G. Paulus, F. Lindner, D. B. Milosevic, W. Becker, *Phys. Scr.* **T110** 120 (2004)

[123] A. E. Siegman, *Lasers*, University Science Books, Sausalito, CA (1986)

[124] Andor Technology Limited, Belfast, UK, *A users's guide to Andor CCDs*, 2 edn. (2006)

[125] J. Bolze, J. Kim, J.-Y. Huang, S. Rah, H. S. Youn, B. Lee, T. J. Sjin, M. Ree, *Macromol. Res.* **10** 2 (2002)

[126] O. Cheshnovsky, S. H. Yang, C. L. Pettiette, M. J. Craycraft, R. E. Smalley, *Rev. Sci. Instrum.* **58** 2131 (1987)

[127] G. C. King, M. Tronc, F. H. Read, R. C. Bradford, *J. Phys. B: Atom. Molec. Phys.* **10** 2479 (1977)

[128] P. Kruit, F. H. Read, *J. Phys. E: Sci. Instrum.* **16** 313 (1983)

[129] A. C. Thompson, D. T. Attwood, E. M. Gullikson, M. R. Howells, J. B. Kortright, A. L. Robinson, J. H. Underwood, K.-J. Kim, J. Kirz, I. Lindau, P. Pianetta, H. Winick, G. P. Williams, J. H. Scofield, *X-ray Data Booklet*, Lawrence Berkeley National Laboratory, Berkeley (2001)

[130] O. Hemmers, S. B. Whitfield, P. Glans, H. Wang, D. W. Lindle, R. Wehlitz, I. A. Sellin, *Rev. Sci. Instrum.* **69** 3809 (2010)

[131] V. Ulrich, S. Barth, T. Lischke, S. Joshi, T. Arion, M. Mucke, M. Förstel, A. M. Bradshaw, U. Hergenhahn, *J. Electron Spectrosc.* **183** 70 (2011)

[132] O. Graefe, *Femtosecond photoelectron spectroscopy for observation of chemical reactions*, Ph.D. thesis, University of Kassel (2005)

[133] A. T. J. B. Eppink, D. H. Parker, *Rev. Sci. Instrum.* **68** 3477 (1997)

[134] V. Dribinski, A. Ossadtchi, V. A. Mandelshtam, H. Reisler, *Rev. Sci. Instrum.* **73** 2634 (2002)

[135] C. Bordas, F. Paulig, H. Helm, D. L. Huestis, *Rev. Sci. Instrum.* **67** 2257 (1996)

[136] M. J. J. Vrakking, *Rev. Sci. Instrum.* **72** 4084 (2001)

[137] W. Gudat, C. Kunz, *Phys. Rev. Lett.* **29** 169 (1972)

[138] D. L. Griscom, *J. Non-Cryst. Solids* **24** 155 (1977)

[139] A. Bianconi, *Appl. Surf. Sci.* **6** 392 (1980)

[140] D. G. J. Sutherland, M. Kasrai, G. M. Bancroft, Z. F. Liu, K. H. Tan, *Phys. Rev. B* **48** 14989 (1993)

[141] I. Tanaka, J. Kawai, H. Adachi, *Phys. Rev. B* **52** 11733 (1995)

[142] F. J. Himpsel, F. R. McFeely, A. Taleb-Ibrahimi, J. A. Yarmoff, *Phys. Rev. B* **38** 6084 (1988)

[143] Z. H. Lu, M. J. Graham, D. T. Jiang, K. H. Tan, *Appl. Phys. Lett.* **63** 2941 (1993)

[144] Z. H. Lu, J. P. McCaffrey, B. Brar, G. D. Wilk, R. M. Wallace, L. C. Feldman, S. P. Tay, *Appl. Phys. Lett.* **71** 2764 (1997)

[145] C. N. Berglund, W. E. Spicer, *Phys. Rev. A* **136** 1044 (1964)

[146] C. N. Berglund, W. E. Spicer, *Phys. Rev. A* **136** 1030 (1964)

[147] O. A. Baschenko, V. I. Nefedov, *J. Electron Spectrosc.* **17** 405 (1979)

[148] B. L. Henke, E. M. Gullikson, J. C. Davis, *At. Data Nucl. Tables* **54** 181 (1993)

[149] S. Tanuma, C. J. Powell, D. R. Penn, *Surf. Interface Anal.* **17** 927 (1991)

[150] M. Grimm, B. Langer, S. Schlemmer, T. Lischke, U. Becker, W. Widdra, D. Derlich, R. Flesch, E. Rühl, *Phys. Rev. Lett.* **96** 066801 (2006)

[151] A. Bianconi, *Surf. Sci.* **89** 41 (1979)

[152] T. D. Thomas, R. W. Shaw, *J. Electron. Spectrosc.* **5** 1081 (1974)

[153] B. E. Mills, R. L. Martin, D. A. Shirley, *J. Am. Chem. Soc.* **98** 2380 (1976)

[154] R. Sankari, M. Ehara, H. Nakatsuji, Y. Senba, K. Hosokawa, H. Yoshida, A. De Fanis, Y. Tamenori, S. Aksela, K. Ueda, *Chem. Phys. Lett.* **380** 647 (2003)

[155] E. Paparazzo, M. Fanfoni, E. Severini, *Appl. Surf. Sci.* **56-58** 866 (1992)

[156] A. A. Bakke, H.-W. Chen, W. L. Jolly, *J. Electron Spectrosc.* **20** 333 (1980)

[157] M. O. Krause, J. H. Oliver, *J. Phys. Chem. Ref. Data* **8** 329 (1979)

[158] D. E. Ramaker, J. S. Murday, N. H. Turner, G. Moore, M. G. Lagally, J. Houston, *Phys. Rev. B* **19** 5375 (1979)

[159] T. H. DiStefano, D. E. Eastman, *Phys. Rev. Lett.* **27** 1560 (1971)

[160] T. H. DiStefano, D. E. Eastman, *Solid State Commun.* **9** 2259 (1971)

[161] H. Ibach, J. E. Rowe, *Phys. Rev. B* **10** 710 (1974)

[162] A. van Blaaderen, A. P. M. Kentgens, *J. Non-Cryst. Solids* **149** 161 (1992)

[163] E. Bersch, S. Rangan, R. A. Bartynski, E. Garfunkel, E. Vescovo, *Phys. Rev. B* **78** 085114 (2008)

[164] H. K. Kim, T. S. Kim, J. Lee, S. K. Jo, *Phys. Rev. B* **76** 165434 (2007)

[165] K. R. Wilson, S. Zou, J. Shu, E. Rühl, S. R. Leone, G. C. Schatz, M. Ahmed, *Nano Lett.* **7** 2014 (2007)

[166] J. H. D. Eland, O. Vieuxmaire, T. Kinugawa, P. Lablanquie, R. I. Hall, F. Penant, *Phys. Rev. Lett.* **90** 053003 (2003)

[167] P. Lablanquie, L. Andric, J. Palaudoux, U. Becker, M. Braune, J. Viefhaus, F. Eland, J. H. D. Penant, *J. Electron Spectrosc.* **156-158** 51 (2007)

[168] R. D. Molloy, A. Danielsson, L. Karlsson, H. D. Eland, *Chem. Phys.* **335** 49 (2007)

[169] T. Jahnke, A. Czasch, M. S. Schöffler, S. Schössler, A. Knapp, M. Käsz, J. Titze, C. Wimmer, K. Kreidi, R. E. Grisenti, A. Staudte, O. Jagutzki, U. Hergenhahn, H. Schmidt-Böcking, R. Dörner, *Phys. Rev. Lett.* **93** 163401 (2004)

[170] E. Rühl, C. Schmale, H. C. Schmelz, H. Baumgärtel, *Chem. Phys. Lett.* **191** 430 (1992)

[171] M. Mucke, M. Braune, S. Barth, M. Förstel, T. Lischke, V. Ulrich, T. Arion, U. Becker, A. Bradshaw, U. Hergenhahn, *Nature Phys.* **6** 143 (2010)

[172] T. Arion, M. Mucke, M. Förstel, A. M. Bradshaw, U. Hergenhahn, *J. Chem. Phys.* **134** 074306 (2011)

[173] C. Gazier, J. R. Prescott, *Phys. Lett. A* **32** 425 (1970)

[174] H. W. Biester, M. J. Besnard, G. Dujardin, L. Hellner, E. E. Koch, *Phys. Rev. Lett.* **59** 1277 (1987)

[175] R. Herrmann, S. Samarin, H. Schwabe, J. Kirschner, *Phys. Rev. Lett.* **81** 2148 (1998)

[176] G. Stefani, S. Iacobucci, A. Ruocco, R. Gotter, *J. Electron Spectrosc.* **127** 1 (2002)

[177] G. van Riessen, Z. Wei, R. S. Dhaka, C. Winkler, F. O. Schumann, J. Kirschner, *J. Phys.: Condens. Matter* **22** 092201 (2010)

[178] F. O. Schumann, C. Winkler, J. Kirschner, *Phys. Status Solidi B* **246** 1483 (2009)

[179] H. W. Haak, G. A. Sawatzky, T. D. Thomas, *Phys. Rev. Lett.* **41** 1825 (1978)

[180] G. A. van Riessen, S. M. Thurgate, D. E. Ramaker, *J. Electron. Spectrosc.* **161** 150 (2007)

[181] G. Stefani, R. Gotter, A. Ruocco, F. Offi, F. De Pieve, S. Iacobucci, A. Morgante, A. Verdini, A. Liscio, H. Yao, R. A. Bartynski, *J. Electron Spectrosc.* **141** 149 (2004)

[182] S. M. Werner, H. Störi, H. Winter, *Surf. Sci.* **518** L569 (2002)

[183] S. M. Thurgate, *Surf. Interface Anal.* **20** 627 (1993)

[184] S. Ramdas, J. Klinowski, *Nature* **308** 521 (1984)

[185] M. Munoz-Navia, C. Winkler, R. Patel, M. Birke, F. O. Schumann, J. Kirschner, *J. Phys.: Condens. Matter* **21** 355003 (2009)

[186] F. Krausz, M. Ivanov, *Rev. Mod. Phys.* **81** 163 (2009)

[187] A. N. Pfeiffer, C. Cirelli, M. Smolarski, R. Dörner, U. Keller, *Nature Phys.* **7** 428 (2011)

[188] A. L. Cavalieri, N. Müller, T. Uphues, V. S. Yakovlev, A. Baltuska, B. Horvath, B. Schmidt, L. Blümel, R. Holzwarth, S. Hendel, M. Drescher, U. Kleineberg, M. Echenique, R. Kienberger, F. Krausz, *Nature* **449** 1029 (2007)

[189] C. Graf, B. Langer, M. Grimm, R. Lewinski, M. Grom, E. Rühl, *J. Electron Spectrosc.* **166** 74 (2008)

[190] D. Böschel, M. Janich, H. Roggendorf, *J. Coll. Interf. Sci.* **267** 360 (2003)

[191] V. Goertz, N. Dingenouts, H. Nirschl, *Part. Part. Sys. Charact.* **26** 17 (2009)

[192] T. Rieker, A. Hanprasopwattana, A. Datye, P. Hubbard, *Langmuir* **15** 638 (1999)

[193] K. W. Powers, S. C. Brown, V. B. Krishna, S. C. Wasdo, B. M. Moudgil, S. M. Roberts, *Toxicol. Sci.* **90** 296 (2006)

[194] H. Boukari, J. S. Lin, M. T. Harris, *Chem. Mater.* **9** 2376 (1997)

[195] D. L. Green, J. S. Lin, Y.-F. Lam, M. Z.-C. Hu, D. W. Schaefer, M. T. Harris, *J. Colloid Interf. Sci.* **266** 346 (2003)

[196] D. Pontoni, T. Narayanan, A. R. Rennie, *Langmuir* **18** 56 (2002)

[197] P. Riello, M. Mattiazzi, J. S. Pedersen, A. Benedetti, *Langmuir* **24** 5225 (2008)

[198] S. Fouilloux, A. Desert, O. Tache, O. Spalla, J. Daillant, A. Thill, *J. Colloid Interf. Sci.* **346** 79 (2010)

[199] G. Orts-Gil, K. Natte, D. Drescher, H. Bresch, A. Mantion, J. Kneipp, W. Österle, *J. Nanopart. Res.* **13** 1593 (2011)

[200] I. Shyjumon, M. Rappolt, B. Sartori, H. Amenitsch, P. Laggner, *Rev. Sci. Instrum.* **79** 043905 (2008)

[201] J. B. A. Mitchell, J. Courbe, A. I. Florescu-Mitchell, S. di Stasio, T. Weiss, *J. Appl. Phys.* **100** 124918 (2006)

[202] J. B. A. Mitchell, S. di Stasio, J.-L. Le Garrec, A. I. Florescu-Mitchell, T. Narayanan, M. Sztucki, *J. Appl. Phys.* **105** 124904 (2009)

[203] S. di Stasio, J. B. A. Mitchell, J.-L. Le Garrec, B. L., M. Wulff, *Carbon* **44** 1267 (2006)

[204] F. Ossler, J. Larsson, *J. Appl. Phys.* **98** 114317 (2005)

[205] K. Chen, A. Kromin, M. P. Ulmer, B. W. Wessels, V. Backman, *Opt. Commun* **228** 1 (2003)

[206] J. Shu, K. R. Wilson, A. N. Arrowsmith, M. Ahmed, S. R. Leone, *Nano Lett.* **5** 1009 (2005)

[207] J. Shu, K. R. Wilson, M. Ahmed, S. R. Leone, *Rev. Sci. Instrum.* **77** 043106 (2006)

[208] M. J. Bogan, W. H. Benner, S. Boutet, U. Rohner, M. Frank, A. Barty, M. M. Seibert, F. Maia, S. Marchesini, S. Bajt, B. Woods, V. Riot, S. P. Hau-Riege, M. Svenda, E. Marklund, E. Spiller, J. Hajdu, H. N. Chapman, *Nano Lett.* **8** 310 (2008)

[209] M. J. Bogan, S. Boutet, H. N. Chapman, S. Marchesini, A. Barty, W. H. Benner, U. Rohner, M. Frank, S. P. Hau-Riege, S. Bajt, B. Woods, M. M. Seibert, B. Iwan, N. Timneanu, J. Hajdu, J. Schulz, *Aerosol Sci. Tech.* **44** i (2010)

[210] M. J. Bogan, D. Starodub, C. Y. Hampton, R. G. Sierra, *J. Phys. B: At. Mol. Opt. Phys.* **43** 194013 (2010)

[211] S. Swaraj, C. Wang, T. Araki, G. Mitchell, L. Liu, S. Gaynor, B. Deshmukh, H. Yan, C. R. McNeill, H. Ade, *Eur. Phys. J. Special Topics* **167** 121 (2009)

[212] T. Araki, H. Ade, J. M. Stubbs, D. C. Sundberg, G. E. Mitchell, J. B. Kortright, A. L. D. Kilcoyne, *Appl. Phys. Lett.* **89** 124106 (2006)

[213] P. Laven, *Appl. Opt.* **42** 436 (2003)

[214] E. Filatova, V. Lukyanov, R. Barchewitz, J.-M. Andre, M. Idir, P. Stemmler, *J. Phys.: Condens. Matter* **11** 3355 (1999)

[215] A. A. Chabanov, Y. Jun, J. Norris, *Appl. Phys. Lett.* **84** 3573 (2004)

[216] B. J. Maranzano, N. J. Wagner, *J. Chem. Phys.* **114** 10514 (2001)

[217] M. Minor, A. J. van der Linde, H. P. van Leeuwen, J. Lyklema, *Colloids Surfaces A: Physicochem. Eng. Aspects* **142** 165 (1998)

[218] R. D. Badley, W. T. Ford, F. J. McEnroe, R. A. Assink, *Langmuir* **6** 792 (1990)

[219] I. Simon, *J. Am. Ceram. Soc.* **40** 150 (1957)

[220] T. Zhou, K. A. Marx, M. Warren, H. Schulze, S. J. Braunhut, *Biotechnol. Prog.* **16** 268 (2000)

[221] L. B. Kiss, J. Söderlund, G. A. Niklasson, C. G. Granqvist, *Nanotechnology* **10** 25 (1999)

[222] C. G. Granqvist, R. A. Buhrman, *Solid State Commun.* **18** 123 (1976)

[223] C. A. R. Costa, C. A. P. Leite, F. Galembeck, *J. Phys. Chem. B* **107** 4747 (2003)

[224] A. Imhof, M. Megens, J. J. Engelberts, D. T. N. de Lang, R. Sprik, W. L. Vos, *J. Phys. Chem. B* **103** 1408 (1999)

[225] Q. Zhang, A. Dong, Y. Zhai, F. Liu, G. Gao, *J. Phys. Chem. C.* **113** 12033 (2009)

[226] R. Finsy, *Adv. Colloid Interface Sci.* **52** 79 (1994)

[227] A. R. Jones, *Prog. Energy Combust. Sci.* **25** 1 (1999)

[228] C. M. Sorensen, D. J. Fischbach, *Opt. Commun.* **173** 145 (2000)

[229] M. J. Berg, C. M. Sorensen, A. Chakrabarti, *J. Quant. Spectrosc. Ra.* **111** 782 (2010)

[230] K. S. Birdi, *Handbook of Surface and Colloid Chemistry*, CRC Press/Taylor & Francis, Boca Raton, 3^{rd} edn. (2008)

[231] G. Porod, *Koll. Z.* **124** 83 (1951)

[232] A. Y. Huang, J. C. Berg, *J. Colloid. Interf. Sci.* **279** 440 (2004)

[233] C. Scherdel, G. Reichenauer, *Carbon* **47** 1102 (2009)

[234] S. C. Woronick, W. Ng, A. Krol, Y. H. Kao, E. Arnold, *J. Appl. Phys.* **69** 1631 (1991)

[235] E.-D. Klinkenberg, P. Illinsky, *Cryst. Res. Technol.* **23** 1193 (1988)

[236] P. Tripathi, G. S. Lodha, M. H. Modi, A. K. Sinha, K. J. S. Sawhney, R. V. Nandedkar, *Opt. Commun.* **211** 215 (2002)

[237] W. Blau, E. S. Gluskin, A. P. Lyssenko, G. N. Kulipanov, K. Hübner, *Nucl. Instrum. Methods* **208** 605 (1983)

[238] A. Apolonski, P. Dombi, G. G. Paulus, M. Kakehata, R. Holzwarth, T. Udem, C. Lemell, K. Torizuka, J. Burgdörfer, T. W. Hänsch, F. Krausz, *Phys. Rev. Lett.* **92** 073902 (2004)

[239] P. Vasa, C. Ropers, R. Pomraenke, C. Lienau, *Laser & Photon. Rev.* **3** 483 (2009)

[240] C. Lienau, *Phil. Trans. R. Soc. Lond. A* **362** 861 (2004)

[241] M. I. Stockman, M. F. Kling, U. Kleineberg, F. Krausz, *Nat. Photon.* **1** 539 (2007)

[242] M. I. Stockman, *New J. Phys.* **10** 025031 (2008)

[243] M. Durach, A. Rusina, V. I. Klimov, M. I. Stockman, *New J. Phys.* **10** 105011 (2008)

[244] E. Goulielmakis, M. Schultze, M. Hofstetter, V. S. Yakovlev, J. Gagnon, M. Uiberacker, A. L. Aquila, E. M. Gullikson, D. T. Attwood, R. Kienberger, F. Krausz, U. Kleineberg, *Science* **320** 1614 (2008)

[245] D. Ray, Z. Chen, S. De, W. Cao, I. V. Litvinyuk, A. T. Le, C. D. Lin, M. F. Kling, C. L. Cocke, *Phys. Rev. A* **83** 013410 (2011)

[246] S. Chelkowski, D. Bandrauk, *Phys. Rev. A* **71** 053815 (2005)

[247] A. Gazibegovic-Busuladzic, D. B. Milosevic, W. Becker, B. Bergues, H. Hultgren, I. Y. Kiyan, *Phys. Rev. Lett.* **104** 103004 (2010)

[248] F. Lindner, M. G. Schätzel, H. Walther, A. Baltuska, E. Goulielmakis, F. Krausz, D. B. Milosevic, D. Bauer, W. Becker, G. G. Paulus, *Phys. Rev. Lett.* **95** 040401 (2005)

[249] S. Zherebtsov, T. Fennel, J. Plenge, E. Antonsson, I. Znakovskaya, A. Wirth, O. Herrwerth, F. Süßmann, C. Peltz, I. Ahmad, S. Trushin, V. Pervak, S. Karsch, M. J. J. Vrakking, B. Langer, C. Graf, M. I. Stockman, F. Krausz, E. Rühl, M. F. Kling, *Nature Phys.* **7** 656 (2011)

[250] R. Gopal, K. Simeonidis, R. Moshammer, T. Ergler, M. Dürr, M. Kurka, K.-U. Kühnel, S. Tschuch, C.-D. Schröter, D. Bauer, J. Ullrich, A. Rudenko, O. Herrwerth, T. Uphues, M. Schultze, E. Goulielmakis, M. Uiberacker, M. Lezius, M. F. Kling, *Phys. Rev. Lett.* **103** 053001 (2009)

[251] D. Mathur, F. A. Rajgara, *J. Chem. Phys.* **133** 061101 (2010)

[252] D. Mathur, F. A. Rajgara, A. R. Holkundkar, N. K. Gupta, *Phys. Rev. A* **82** 025201 (2010)

[253] M. Busuladzic, A. Gazibegovic-Busuladzic, D. B. Milosevic, *Laser Phys.* **16** 289 (2006)

[254] M. J. Nandor, M. A. Walker, L. D. Van Woerkom, *J. Phys. B: At. Mol. Opt. Phys.* **31** 4617 (1998)

[255] F. Grasbon, G. G. Paulus, H. Walther, P. Villoresi, G. Sansone, S. Stagira, M. Nisoli, S. De Silvestri, *Phys. Rev. Lett.* **91** 173003 (2003)

[256] T. D. Donnelly, T. Ditmire, K. Neuman, M. D. Perry, R. W. Falcone, *Phys. Rev. Lett.* **76** 2472 (1996)

[257] C. Jacoboni, L. Reggiani, *Rev. Mod. Phys.* **55** 645 (1983)

[258] M. V. Ammosov, N. B. Delone, V. P. Krainov, *Sov. Phys. JETP* **64** 1191 (1986)

[259] W. C. Martin, R. Zalubas, *J. Phys. Chem. Ref. Data* **12** 323 (1983)

[260] B. N. Khlebtsov, V. A. Khanadeev, N. G. Khlebtsov, *Langmuir* **24** 8964 (2008)

[261] T. Fennel, T. Döppner, J. Passig, C. Schaal, J. Tiggesbäumker, K.-H. Meiwes-Broer, *Phys. Rev. Lett.* **98** 143401 (2007)

[262] J. Zweiback, T. Ditmire, M. D. Perry, *Phys. Rev. A* **59** R3166 (1999)

[263] M. I. Stockman, *Phys. Rev. Lett.* **93** 137404 (2004)

[264] T. V. Liseykina, S. Pirner, D. Bauer, *Phys. Rev. Lett.* **104** 095002 (2010)

Short Summary

In this work, X-rays and intense few-cycle laser pulses are used to study free nanoparticles prepared in a beam in high vacuum. With this technique, nanoparticles are sprayed from a dispersion and dried, leaving an aerosol of free nanoparticles that are transferred into high vacuum *via* an aerodynamic lens yielding a beam of isolated nanoparticles in vacuum. The nanoparticle beam technique allows studying the intrinsic properties of nanoparticles without interaction with a surrounding medium, as is the case when deposited samples or dispersions are studied. Furthermore, changes to the nanoparticles over time (radiation damage, charging etc.) can be neglected, as fresh sample is continuously fed to the interaction area.

In the first part of this thesis, photoemission from free SiO_2 nanoparticles is studied after excitation by soft X-rays in a site, element, and state selective manner. Electron-electron coincidence spectroscopy allows the identification of numerous two-electron emission channels around the Si 2p inner shell absorption edge.

In the second part, elastic scattering of soft X-rays from free SiO_2 nanoparticles in the small angle scattering range (1.2-9.3°) allows determination of the size and shape of the nanoparticles *in situ* and the determination of their refractive indices near the Si 2p and O 1s inner shell absorption edges.

In the third part, free SiO_2 nanoparticles are excited by few-cycle laser pulses with a well defined and variable waveform (pulse length: $\approx$ 5 fs, λ: 720 nm). By varying the carrier-envelope phase of the laser pulses, the electron emission from SiO_2 nanoparticles can be controlled. The kinetic energies of electrons emitted from SiO_2 nanoparticles extend to significantly higher cut-off energies than in rare gases. This is discussed in the context of electron rescattering in a locally enhanced electric field near the nanoparticle surface.

Kurze Zusammenfassung

In dieser Arbeit werden freie Nanopartikel in einem kontinuierlichen Nanopartikelstrahl im Hochvakuum mit weicher Röntgenstrahlung und intensiver Kurzpuls-Laserstrahlung untersucht. Dispersionen der Nanopartikel werden versprüht, die dadurch erzeugten Tröpfchen getrocknet und die freien Nanopartikel mittels einer aerodynamischen Linse in Hochvakuum überführt. Mit diesem Ansatz können die intrinsischen Eigenschaften der Nanopartikel untersucht werden ohne Einfluss von der Umgebung, wie es für deponierte Partikel und Dispersionen der Fall ist.

Im ersten Teil der Arbeit wird die Photoemission von freien SiO_2 Nanopartikeln nach der orts-, element- und zustandsselektiven Anregung mit weicher Röntgenstrahlung untersucht. Mit Elektron-Elektron-Koinzidenzspektroskopie lassen sich im Bereich der Si 2p Absorptionskante mehrere Zwei-Elektronen Emissionskanäle beobachten.

Im zweiten Teil wird elastische Streuung von weicher Röntgenstrahlung an freien SiO_2 Nanopartikeln im Kleinwinkelbereich (1.2-9.3°) untersucht. Anhand von der Winkelabhängigkeit der Streuung kann die Größe und Form der Nanopartikel *in situ* sowie der energieabhängige komplexe Brechungsindex der Nanopartikel im Bereich der Si 2p und O 1s Absorptionskanten ermittelt werden.

Im dritten Teil werden freie SiO_2 Nanopartikel mit intensiven Laserpulsen mit variabler Pulsform angeregt (Pulsdauer: $\approx$ 5 fs, λ: 720 nm). Durch Variieren der carrier-envelope-phase kann die Winkelverteilung der Elektronenemission gesteuert werden. Die cut-off Energie der Elektronenemission von den Nanopartikeln ist um vielfaches höher als bei Edelgasen. Diese Unterschiede werden durch Elektronen-Rückstreuung an den Nanopartikeln in einem lokal verstärkten Feld an der Oberfläche erklärt.

Parts of the results presented in this thesis have been published in:

S. Zherebtsov, T. Fennel, J. Plenge, E. Antonsson, I. Znakovskaya, A. Wirth, O. Herrwerth, F. Süßmann, C. Peltz, I. Ahmad, S. A. Trushin, V. Pervak, S. Karsch, M. J. J. Vrakking, B. Langer, C. Graf, M. I. Stockman, F. Krausz, E. Rühl, and M. F. Kling

"Controlled near-field enhanced electron acceleration from dielectric nanospheres with intense few-cycle laser fields"

Nature Physics, **7**, 656-662 (2011)

Thanks go to all the good people I had the chance to work with during my doctoral studies.

Firstly, I thank my advisor Prof. Dr. E. Rühl for giving me the opportunity to work in his group, for teaching me so much about how to do science, and for his constant support and interest in the progress of the work.

I thank Prof. Dr. H. Baumgärtel for accepting to be the second reviewer.

I thank Dr. B. Langer for all help on both practical and scientific subjects and for sharing with me his great expertise on X-ray spectroscopy and vacuum technology. And not least for proof-reading this work.

Thanks go to Dr. R. Lewinski for all the good times we shared in the lab and outside of it.

I also thank the people I got the chance to work with on laser projects both in Garching and Berlin: Dr. J. Plenge, Dr. S. Zherebtsov, I. Znakovskaya, Prof. Dr. M. F. Kling, C. Peltz, and Prof. Dr. Th. Fennel.

Thanks go to the people at the Helmholtz Center in Berlin for support during the experiments there.

Without nanoparticle samples, this work would not have been possible. For this, I thank Dr. C. Graf, P. Schmiel, and P. Stumpf.

I also want to thank the people that I had the chance to work with on projects that for one reason or another weren't included in this thesis. For the beam times in France I thank Dr. J. Söderström, Dr. C. Nicolas, Dr. X. Liu , Dr. C. Miron, G. Saidani, Dr. O. Sublemontier, Dr. J.-L. Le Garrec, and Prof. Dr. J. B. Mitchell. I also thank the people from the Karlsruhe group for our beamtimes in Berlin: Dr. J. Meinen, Dr. M. Eritt, S. Khasminskaya.

And last but not least, I thank Fee-Saskia for proof-reading and for being there for me all the time.

The CV is not contained in the online version.

The CV is not contained in the online version.